University of Exeter

College of Engineering, Mathematics and Physical Sciences

Thesis for the Degree of Doctor of Philosophy in Physics

Red Blood Cell Membrane: Organisation, Mechanics and Biochemical Signalling

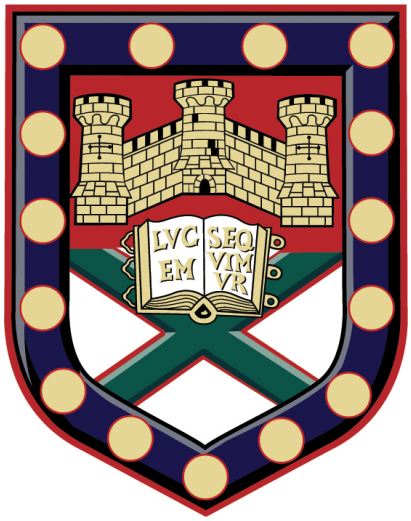

Author:

Beth Mary McGill

Supervisors:

Dr. Peter G Petrov

Prof. C Peter Winlove

I certify that all material in this thesis which is not my own work has been identified and that any material that has previously been submitted and approved for the award of a degree by this or any other University has been acknowledged.

15th August 2021

Beth McGill

Acknowledgements

First and foremost, I would like to thank my supervisors Dr. Peter Petrov and Prof. Peter Winlove for conceptualising this project and giving me the opportunity to bring it to fruition. I have been able to learn so much through your guidance and support, as well as your genuine passion and enthusiasm for research. Peter Winlove, our discussions towards the start of the PhD proved an invaluable foundation. Peter Petrov, thank you for all your feedback that has improved my research ability. Above all else, thank you for your constant reassurance that has kept me going.

To Bob, I fear a single paragraph of thanks will not do justice for all that you have taught me. You took my clueless self and managed to make a competent researcher out of me. Thank you for all your guidance and instruction (especially for the dilution calculations); every lab duet; and pushing me to bring my absolute best self to the table. Above all else, thank you for being my friend.

To my academic sibling Skye, I am so grateful to have had you on this journey with me. Thank you for answering every question, for your guidance in the lab and for all your support during the write-up. Whilst it hasn't been an easy ride, especially with the pandemic, you have handled everything with an awe-inspiring strength and resilience. I am so proud of you and I can't wait to celebrate our success at Graduation. If it takes writing a thesis for us to meet, it will have been worth it.

I'd also like to say thank you to Ellen, for all the help and guidance you provided in the lab, particularly for Chloe's and your help with my ATP experiment. To the wider Biophysics group, particularly: Dave, Anna, Michelle, Michele, Fay, Toby, Michael, Ben, Richard, Jannete, Ryan, Seb and Sarah. You have made this experience a memorable and enjoyable one. Thank you for all the days out; trips to Europe; and for always looking after me after all the wine at Christmas. I hope that we will be able to celebrate over cocktails soon!

Laura, our friendship will always be one of my most treasured memories of this time. Thank you for all the bottles of wine that we have shared and for every time you have listened to me moan and responded with what I've needed to hear. You have

honestly been and continue to be an invaluable part of my life. Thank you also for proof-reading my thesis at such short notice!

I'd like to thank my Brownie team (Rachel, Kat, Ursula, Rachel and Amanda) for being the perfect weekly escape from the academic bubble. Brownies has always been one of my favourite times of the week and you all contributed to making it so. Kat, I will forever be grateful to have you as a friend. You are a constant source of inspiration and proof that mermaids appear during perilous events. Thank you for being there for me when I needed it the most.

Lucy, our weekly run/rant sessions are a huge part of the reason I have made it through these last two years. I can only hope that you have found them as freeing and restorative as I have. To our wider OODS group, thank you for slowing the pace of life right down on our trips to the middle of nowhere. Let it forever be written in a scientific document that you all caused the pandemic by stepping in that stone circle.

To Hannah, you are my favourite sister. Thank you for the constant reminder that it doesn't always have to be about science, and that packing your favourite outfits into a suitcase and moving to the other side the world is probably a better life choice. I am in awe of your confidence, your beauty and the sheer size of your eye-rolls when I start talking about science. Thank you for always having enough sass to cover us both.

Finally, to my Mum and Dad. In a world where girls are rarely encouraged into science, you never let my enthusiasm for the subject fade. Thank you for all the museum visits and for encouraging me to pick the *easy* A-levels that started me on my path into Physics. Thank you for the countless trips up and down the motorway that you have made since and for enduring every teary phone call when I have felt overwhelmed. Thank you especially for supporting me over the last four and half years, in every way I can possibly think of. Thank you from the bottom of my heart.

This thesis is dedicated to my parents,

Jane and Dave McGill.

I love you both so much.

Abstract

This work presents an investigation into the physiological state of the red blood cell (RBC) membrane. Particular focus is given to the properties of the composite membrane and their implication in cellular signalling resulting from increased mechanical deformation.

Intense synchrotron x-ray radiation was used to probe Langmuir monolayers akin to both leaflets of the RBC plasma membrane. Complex phospholipid mixtures were spread at the air-subphase interface of a Langmuir trough, and investigated at a surface pressure of 30 mN/m and temperature of 20°C. Three geometries were used to probe the monolayers: grazing incidence x-ray diffraction (GIXD) measured lateral ordering and crystalline structure within the monolayer, and both grazing incidence x-ray off-specular scattering (GIXOS) and x-ray reflectivity (XRR) measured the monolayer thickness and electron density profiles perpendicular to the air-subphase interface. On the pure water subphase GIXD results demonstrated a hexagonal packing structure for both leaflets, although there were dissimilarities in the parameters of this packing. The inner leaflet (IL) monolayer demonstrated larger domains of crystalline order than the outer leaflet (OL) monolayer, most likely a result of the IL's high phosphatidylethanolamine (PE) content in comparison to the OL's high sphingomyelin (SM) content. The two monolayers were of comparable thickness overall, however, a greater electron density profile was measured for the IL monolayer. This was suggestive of differences in the phospholipid tilt angle, relative to the normal of the air-subphase interface, in the two monolayers.

The effect of oxidative stress on the mechanical properties of the RBC membrane was extensively measured using thermal fluctuation spectroscopy (TFS). The spectra of healthy RBCs were measured before and after treatment with three different oxidising agents, chosen for their known ability to target specific components of the membrane. Changes in each of the elastic moduli of the cell can be attributed to oxidative damage to a particular component of the membrane, since the lipid bilayer dominates the contribution to the cell's bending modulus and the cytoskeleton governs the shear modulus. In good agreement with the literature, the results demonstrated

that hydrogen peroxide (H_2O_2) preferentially targeted the cytoskeleton and cumene hydroperoxide (cumOOH) targeted the lipid bilayer to a greater extent than H_2O_2, whilst diamide was less specific, affecting both the lipid bilayer and cytoskeleton to a varying degree.

In parallel, a novel method for measuring the mechanically stimulated adenosine triphosphate (ATP) release from RBCs was developed. Cells were subjected to an externally applied increased shear rate, using a cannula attached to a syringe pump which drove the flow. This novel approach allowed for acute control of experimental parameters, such as the shear rate. Sample ATP was measured using a standard luciferin based assay, which demonstrated that oxidative modification of the RBC membrane leads to an altered ability to release ATP. Moreover, the change in ability of the RBCs to release ATP upon mechanical stimulation was most likely a result of underlying biological processes associated with the oxidative damage, rather than a change to the cell's mechanical properties.

In all stages of this work the molecular action of dimethyl sulphoxide (DMSO) on the RBC membrane was investigated. This posed an interesting question since DMSO has far reaching applications, but the true effects of the solvent are poorly understood. At 10 vol-%, the x-ray monolayer studies demonstrated a strong reorientating effect of the aqueous-DMSO subphase on both the IL and OL monolayers, with the creation of DMSO rich/lipid poor domains. In the TFS study, DMSO treatment at concentrations of 1, 5 and 10 vol-% were shown to weakly affect the mechanical properties of the cell but importantly, recovery was observed. However, the membrane became significantly permeable to ATP upon DMSO treatment, even without mechanical stimulation. This result offers experimental evidence of the pore forming nature of DMSO, as suggested by molecular dynamics simulations. Together, these results provide clarity over the molecular action of DMSO on the RBC and, through applicability to other cell types, offer justification for the many uses of the solvent.

Publications and Conferences

Publications

Effect of DMSO on the Mechanical and Structural Properties of Model and Biological Membranes.

B. Gironi, Z. Kahveci, *B. McGill*, B.D. Lechner, S. Pagliara, J. Metz, A. Moressi, F. Palombo, P. Sassi, P.G. Petrov

Published in Biophysical Journal on 15th June 2020.

Conferences

Red cell mechanical properties and biochemical signalling

B. McGill, B.D. Lechner, C.P. Winlove, P.G. Petrov

BioMedEng18, Imperial College London, UK

Red cell mechanical properties and biochemical signalling

B. McGill, B.D. Lechner, C.P. Winlove, P.G. Petrov

3rd Workshop on Membrane Biophysics, Confèrences de l'Institut Charles Sadron, France.

Red cell mechanical properties and biochemical signalling

B. McGill, B.D. Lechner, C.P. Winlove, P.G. Petrov

Membranes in Health and Disease, King's College London, UK.

Contents

List of Figures

List of Tables

List of Abbreviations

ATP	Adenosine Triphosphate
BAM	Brewster Angle Microscopy
BSA	Bovine Serum Albumin
CF	Cystic Fibrosis
CFTR	Cystic Fibrosis Transmembrane Conductance Regulator
CHOL	Cholesterol
cumOOH	Cumene Hydroperoxide
DMSO	Dimethyl Sulphoxide
DP	Dipalmitoyl (prefix)
FWHM	Full Width at Half Maximum
GIXD	Grazing Incidence X-Ray Diffraction
GIXOS	Grazing Incidence X-Ray Off-Specular Scattering
GSH	Glutathione
H_2O_2	Hydrogen Peroxide
IL	Inner Leaflet
IPAH	Idiopathic Pulmonary Arterial Hypertension
OL	Outer Leaflet
PBS	Phosphate Buffered Saline
PC	Phosphatidylcholine
PE	Phosphatidylethanolamine
PS	Phosphatidylserine
RBC	Red Blood Cell
RIC	Reflection Interference Contrast
RLU	Relative Luminescence Unit
ROS	Reactive Oxygen Species
SH	Sulfhydryl
SM	Sphingomyelin
TFS	Thermal Fluctuation Spectroscopy
UPW	Ultra Pure Water
XRR	X-Ray Reflectivity

1 Introduction

1.1 Red blood cell membrane structure

The first published description of the red blood cell (RBC) is credited to Antoni van Leeuwenhoek in 1675 [1], almost 350 years ago yet strikingly accurate. Since then the RBC has become one of the most intensively studied cells, a direct consequence of its abundance, ease of obtainment and more simple structure when compared with other cells. In humans, the RBC makes up approximately 40 - 45% of total blood volume [2].

With a diameter of approximately 8 μm, the RBC is highly specialised for its fundamental role of transporting oxygen (O_2) through the circulatory system, where, over a 120 day lifetime a cell will travel approximately 400 km. Lacking a nucleus (anucleate), as well as most other cell organelles, the RBC has increased the internal volume available for the O_2 carrying protein, haemoglobin. The biconcave, discocyte shape increases the surface area to volume ratio for optimal O_2 diffusion, as well as allowing for extreme deformations as the RBC traverses the micro-circulation. At this level of the circulatory system vessel diameter is often smaller than that of the cell. These deformations are fundamental in the proper functioning of the circulation, as they reduce the O_2 diffusion distance between cell and vessel wall and, as described throughout this thesis, can initiate cellular signalling pathways.

The RBC membrane is compound in structure, consisting of a lipid bilayer (plasma membrane) and a mesh network of proteins which laminate the inner leaflet of the bilayer. These components provide a selectively permeable barrier whilst maintaining the overall cell shape and stability. A breakdown of typical membrane mass unsurprisingly reveals that proteins are the largest constituent at ∼52%, with lipids and carbohydrates representing 40% and 8% respectively [3]. A schematic of the membrane structure is provided in Figure 1.1.

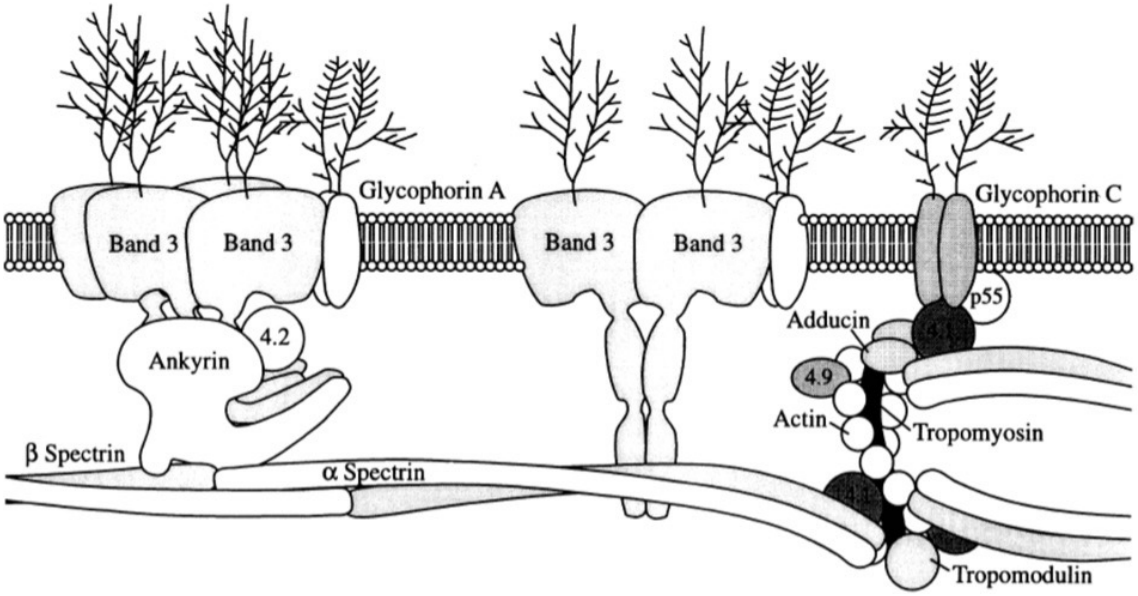

Figure 1.1: ***Schematic of the RBC membrane structure.*** *Composite in nature, the main structural elements of the RBC membrane are the lipid bilayer and spectrin cytoskeleton. The depicted proteins dispersed in the lipid bilayer act to anchor the lipid bilayer to the cytoskeletal network. Adapted from [4].*

1.1.1 Plasma membrane

The plasma membrane is dominated by phospholipid molecules which are interspersed with various proteins. Focusing first on the phospholipids, the typical structure of these molecules is a glycerol backbone attaching one or two fatty acids (acyl chains) to a phosphate group, where the overall molecule is indexed by a defining "head" group attached to the phosphate. Phospholipids are amphiphilic in nature, with the lipid bilayer structure resulting from the entropic arrangement of the hydrophilic polar head groups creating an enclosed region for the hydrophobic acyl chains of the molecule.

The overall shape of the phospholipid molecule results from the size of the head group and the saturation of the acyl chains. Cylindrical phospholipids have a head group in proportion to two saturated chains, whilst conical phospholipids arise either when the head group is out of proportion to the chains, where only one chain is present, or where one or both chains are unsaturated. Unsaturated acyl chains are defined by one or more double bonds in the fatty acid, causing a slight kink in the chain. The saturation of a phospholipid determines the packing density, with unsaturated phospholipids having a lower packing density than saturated phospholipids.

Packing characteristics of phospholipids are often investigated through the use of Langmuir monolayer systems which mimic bulk behaviour. The scattering of intense x-ray radiation from a monolayer surface can be used to obtain molecular level information about either in-plane order or structure perpendicular to the air-subphase interface, depending on the initial x-ray geometry. In-plane measurements detail the crystallographic arrangements of the phospholipid acyl chains, with the ability to measure lattice parameters and crystallographic domain size. Separately, the monolayer electron density, perpendicular to the air-subphase interface, can be obtained through separating the perpendicular structure into slabs of varying thickness. In this method, each slab represents one of the following regions: from the atmosphere, through the phospholipid acyl chains, phospholipid head groups, and finally into the subphase.

Whilst there are several hundred species of lipid that make up the RBC plasma membrane, there are a handful of dominant head groups which give rise to a distinct asymmetry between the leaflets of the lipid bilayer. As demonstrated by Rothman and Lenard [5], phosphatidylethanolamine (PE) and phosphatidylserine (PS) are the main types of lipids found in the inner leaflet, whilst sphingomyelins (SM, the only phospholipid with a sphingosine backbone) and phosphatidylcholines (PC) dominate the outer leaflet.

Other lipids species that can be found in the plasma membrane include glycolipids (the product of a carbohydrate attached to an outer leaflet lipid) and cholesterol. Glycolipids assist in many intercellular activities [6], whilst cholesterol appears to have a more structural role. In recent studies [7], cholesterol has been implicated in the formation of lipid complexes that compartmentalise sections of the membrane due to tight packing with sphingolipids. These more ordered regions are termed rafts and have been associated with protein functionality [8], although limited information is currently disseminated about them.

Embedded proteins

Proteins embedded in the lipid bilayer fall into two subgroups depending on their structural position within the bilayer. Integral proteins, also referred to as transmembrane, span the entire bilayer, connecting the inner leaflet to the outer leaflet. These proteins primarily include ion channels and molecular pumps, but also of note is the Band 3 protein which links the lipid bilayer to the cytoskeleton as demonstrated

in Figure 1.1. Peripheral proteins sit in just one leaflet of the bilayer. Depending on whether they are embedded in the inner or outer leaflet, they can be responsible for anchoring the bilayer to the cytoskeleton, stimulating intra-cellular signalling pathways, or receiving extracellular signals.

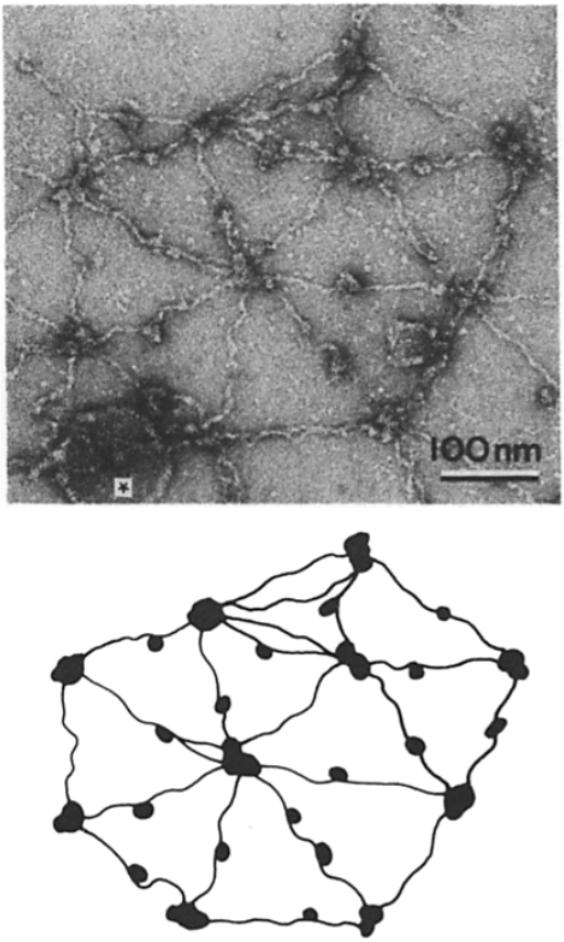

Figure 1.2: ***RBC cytoskeleton.*** *Sub-units of the RBC cytoskeleton observed using electron microscopy (top) and displayed alongside a schematic of the heterodimer-node polygon arrangement (bottom) [9].*

1.1.2 Cytoskeleton

The RBC cytoskeleton is unique in that only the membrane bound element is present, in contrast to nucleated cells which also support a cytoplasmic cytoskeleton. This is a direct consequence of the specialisation of RBCs for the transport of O_2 around the body. As briefly mentioned, the RBC cytoskeleton spans the entire cytoplasmic surface of the lipid bilayer. Coupling of the cytoskeleton to the lipid bilayer occurs via anchor or junction points, as illustrated by the dark nodes in Figure 1.2. These

points involve the aptly named ankyrin protein, which couples the mesh network to Band 3, and protein 4.1 which aids coupling to Glycophorin C.

The cytoskeleton is exclusively composed of proteins, the most abundant of which is spectrin, accounting for 20-25% of the mass of membrane proteins [10]. Spectrin is a large heterodimeric protein built from non-identical α and β sub-units, associated side to side and interacting through hydrophobic bonds and electrostatic attraction [11]. The heterodimers form pentagonal, hexagonal and heptagonal arrangements, creating a *mesh* network with the anchor and junction points as nodes, as shown in Figure 1.2.

1.1.3 Mechanical properties

Of significant importance is the role of the membrane in maintaining the cell shape as the cell negotiates the circulatory system. Each cell will pass through vessels that range in diameter from very large, at a few thousand microns, to very small, where the vessel diameter becomes comparable to, if not smaller than the RBC itself. Not only does this require the cell to significantly deform, but the recovery of the cell to its original shape must occur quickly once the cell is on the venous side of the microcirculation.

The mechanical properties of the RBC are therefore determined by the membrane components described earlier in Section 1.1, and describe the energy-storing resistance to deformation [12]. Whilst the deformation itself is quite complex, it takes just three deformation modes to fully describe the behaviour (Figure 1.3). The deformation modes are the area, bending and shear modes, and each mode is characterised by a specific elastic modulus: K, κ, or μ respectively. Area deformations of the RBC membrane occur on a much higher energy scale (not physiologically relevant) than bending or shear deformations, and as such the area modulus is not as widely investigated as the latter two moduli.

Area deformations

The area modulus, K, reflects the elastic energy storage produced by an isotropic area change of the membrane surface, described as

$$T_{\mathrm{t}} = K\frac{\Delta A}{A_0} \tag{1.1}$$

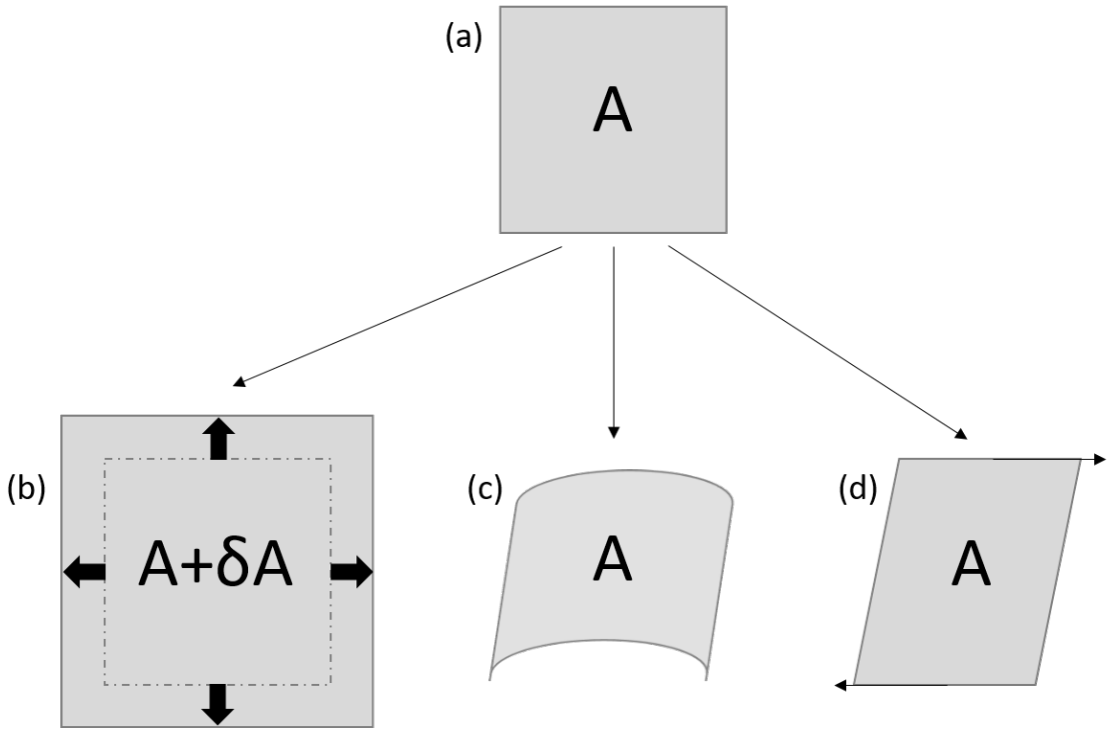

Figure 1.3: ***Mechanical properties of the RBC membrane.*** *The three fundamental deformation modes used to describe the mechanical properties of a soft biomatieral, such as the RBC. The original shape with area A* ***(a)*** *can either undergo area expansion* ***(b)****, bending* ***(c)*** *or shear* ***(d)*** *deformation. Each deformation mode is characterised by a specific elastic moduli.*

where T_t, ΔA and A_0 correspond to the isotropic tension, the change in surface area and the original surface area respectively [13]. In RBCs, the elasticity of the bilayer dominates measured values of K, as the bilayer is both highly inextensible and incompressible.

Bending deformations

The bending of a 2D membrane, such as that of the RBC, involves both a compression and expansion element; the leaflet on the concave side of the bend is compressed, whilst the area on the convex side is increased. The chemical composition of the phospholipids within the lipid bilayer is therefore a major determinant of the bending modulus. This modulus is defined by the energy needed to change the curvature of the membrane, and can be linked to the area modulus with

$$\kappa = \frac{hK}{2} \tag{1.2}$$

where h is the bilayer separation distance [14]. Using a number of different techniques, a broad range of values for κ have been reported. These are discussed in detail in Section 1.2.

Shear deformations

A shear deformation refers to the extension of a membrane surface, whilst the membrane area remains constant. It is the cytoskeleton that endows the otherwise fluid membrane with a shear rigidity, and hence the cytoskeleton dominates any measurement of the shear modulus. The shear modulus is related to the shear tension, T_s, by multiplication with the elongation ratio, $\lambda = (L_0 + \Delta L)/L_0$:

$$T_s = \frac{\mu}{2}(\lambda^2 - \lambda^{-2}) \tag{1.3}$$

where L_0 and ΔL are the original and extension lengths respectively [15].

1.2 Methods of measurement of the RBC membrane mechanics

Various techniques have been developed to probe the elastic moduli of the RBC membrane, although inconsistent values between techniques have been widely reported [16]. This section serves to outline some of these methodologies and the values that have been identified for the various moduli. The method employed within this work, thermal fluctuation spectroscopy (TFS), has been discussed in detail later in Section 4.1.1.

1.2.1 Ektacytometry

As whole blood method ektacytometry measures an average deformability of an ensemble of cells, and is therefore unable to distinguish between the three elastic moduli of the cell. However, it has been included here due to its sensitivity in measuring relative, overall cellular deformability. The system consolidates laser diffractometry with blood viscometry [17], where an incident beam is scattered by a dilute RBC suspension that has been subjected to a shear stress externally applied using the viscometer.

The diffraction pattern obtained is elliptical in shape and corresponds to the average shape of each cell within the sample. It is indexed by an elongation index, EI, a ratio of the long axis, L, to the short axis, W:

$$EI = \frac{L - W}{L + W}. \tag{1.4}$$

Deformability is obtained by measuring the diffraction pattern and hence EI, over a range of applied shear stresses. This method is advantageous due to the convenience and short timescale of the measurement and the small volume of blood required ($\sim$ μL). Measuring the deformability of the RBC population of the sample as a whole makes this a desirable method in the study of RBC physiology.

1.2.2 Filtration and microfluidic devices

Similar to Ektacytometry, both filtration and microfluidic devices are classed as whole blood methods and therefore, are unable to provide detailed evaluation of the RBC's elastic moduli at the fundamental level. The methods are based upon sample flow trough either a pore-like grating or microchannel system.

Filtration

The filtration method probes the ability of a sample of RBCs to pass through a membrane of mircopores. The sample flow is driven either by gravity or a pressure gradient, and deformability is quantified by either the amount of time for a set volume to percolate or the contrary. Although the method is simple and can be carried out in any laboratory, disadvantages include frequent pore occlusion and non-uniform pore diameter, leading to poor reproducibilty in experiments. Further, results are difficult to interpret in terms of the well-defined elastic parameters of the RBC. Nevertheless, the method has been successfully employed in a comparative study of RBCs from diabetic patients and healthy controls [18].

Microfluidic devices

Microfluidic devices offer a solution to some of the limitations experienced using the filtration method. Here, a sample is passed through channels, micrometer in diameter, that mimic the conditions experienced by RBCs in the microcirculation

[13]. By manufacturing the channel system on a chip, deformation of passing RBCs can be directly observed using a microscope. The threshold pressure required to drive the sample flow through the capillary system offers a quantitative measure of RBC deformability [19]. This method has been employed in the assessment of the deformability of both malaria infected RBCs [20] and RBCs from sickle cell patients [21].

1.2.3 Micropipette aspiration

Micropipette aspiration describes the technique of drawing a membrane into a tapered pipette, with diameter on the order of a micron, using a negative pressure to induce the suction and inflict significant deformation on the membrane. This technique was amongst the first used to attain mechanical measurements of cell membranes, attributed to its versatility and ease of interpretation [22]. Not only is this one of the more well established methods, but all three elastic moduli of the RBC can be measured.

The area modulus is measured for osmotically swollen cells [23] using Equation 1.1, where T_t is dependent on the applied pressure, P. For a cell of radius R_c, aspirated into a pipette of radius R_p this tension is defined as

$$T_\mathrm{t} = P\frac{R_\mathrm{p}}{2(1 - R_\mathrm{p}/R_\mathrm{c})}. \tag{1.5}$$

Pressure is applied to aspirate the cell until the external part of the cell is spherical. At such point, any further increase in pressure will cause an increase in the protrusion length of the cell into the pipette and hence, increase the membrane area. Therefore, it follows that $\Delta A/A_0$ is dependent on the change in protrusion length ΔL relative to the original protrusion length L. Accounting for osmotic volume changes the area modulus was determined as $K = 0.45$ Nm^{-1} [24], a relatively large, non-physiological value.

In contrast, both the bending and shear moduli are determined using flaccid membranes. By considering the ratio of the protrusion length, L, to the radius of the pipette, R_p, the behaviour of the aspirated membrane can be divided into three regimes. L/R_p can either be: < 1 as the cell is newly aspirated into the pipette, $= 1$ when a hemispherical cap forms inside the pipette, or > 1 indicating a large protrusion. The behaviour of the membrane is non-specific until the latter regime is reached,

where it is then classified as either solid or liquid drop like. A solid cell will continue to extend into the pipette towards a new equilibrium position as demonstrated by Theret *et al.* [25]. On the contrary, liquid drop behaviour is observed if the membrane flows completely into the pipette, known as *buckling*.

At this point, the pressure difference between the inside and outside of the pipette is related to the shear modulus, μ, through the Law of Laplace

$$P_{\mathrm{o}} - P = \Delta P = \frac{\mu}{R_{\mathrm{p}}}\left(K_1 \frac{L}{R_{\mathrm{p}}} - K_2\right) \tag{1.6}$$

with P_{o} the pressure outside the pipette and $K_1 = 2.45$ and $K_2 = 0.63$ [26]. Since this is a linear approximation for the pressure, Equation 1.6 is only valid for $1 \leq L/R_{\mathrm{p}} \leq 4$. This allows for a direct measurement of the shear modulus, of which Waugh and Evans [27] obtained a value of $\mu = 6.6{\times}10^{-6}$ Nm^{-1}.

The bending modulus is determined by the critical pressure at which bucking occurs and the ratio of the external to internal radii of the pipette [28]. When the external radius is three times larger, bucking occurs at

$$\frac{\kappa}{\Delta P R_{\mathrm{p}}^3} \sim \frac{1}{135}. \tag{1.7}$$

However, when the external radius is six times larger this condition becomes

$$\frac{\kappa}{\Delta P R_{\mathrm{p}}^3} \sim \frac{1}{55}. \tag{1.8}$$

Using this method, the RBC bending modulus was determined at $\kappa = 1.8{\times}10^{-19}$ J [28].

1.2.4 Optical traps

Optical traps employ highly focused lasers to manipulate microscopic objects, where the momentum transfer from the laser to the object results in trapping forces. The laser(s) can interact with the object either directly or indirectly via beads attached to the object. Both these methods are outlined here.

Direct optical trapping

Direct optical trapping is the result of a transfer of momentum from a laser directly to an object, this method can be used to calculate the shear modulus of the RBC. A laser incident on a RBC will transfer a small amount of momentum to the RBC as it meets the boundary of the cell. In a similar manner, another momentum transfer will occur once the laser has passed through the cell and is leaving on the other side. If the refractive index of the RBC is larger than the surrounding medium, this momentum will also be transferred to the RBC resulting in a force on the cell in the direction of the beam. It then follows that two lasers directed at the RBC in opposing directions will elongate the cell along the axis of the beams. The shear modulus was measured at $\mu = (1.3 \pm 0.5) \times 10^{-5}$ Nm^{-1} using this method in the case of an osmotically swollen cell [29].

Indirect optical trapping

Indirect optical trapping requires the binding of silica beads to the RBC, acting as *handles* with which to manipulate the RBC. It is preferable over the previously described method as it minimises damage to the RBC as a result of interaction with the laser. The process of binding the silica beads to the RBC is non-specific, the beads are simply incubated with a RBC suspension after which only RBCs with two silica beads in a diametrical position are measured. The beads are trapped in a similar manner to that described for direct optical trapping, and in increasing the distance between the beads the RBC is stretched. To calculate the shear modulus of the cell, the cell's diameter along the semi-minor axis, D, is measured as a function of the calibrated applied force, F:

$$D(F) = D_0 - \frac{F}{2\pi\mu}, \tag{1.9}$$

where D_0 is the original diameter of the cell. Several values of μ have been obtained for the RBC under varying conditions; such as for a discocyte $\mu = (2.05 \pm 0.3) \times 10^{-6}$ Nm^{-1} or a spherocyte $\mu = (1.9 \pm 0.3) \times 10^{-6}$ Nm^{-1} [30]. Further, the value obtained in measurements of permeabilised spherical ghost cells was two orders of magnitude larger at $\mu = 2 \times 10^{-4}$ Nm^{-1}. The discrepancy is most likely due to assumptions made in the analysis of the discoid and spherical cells [31].

Increasing the number of beads in the trap extends the technique to enable measurement of the area modulus, K. For a free RBC membrane skeleton both μ and K were measured at $(2.4 \pm 0.7) \times 10^{-6}$ Nm^{-1} and $(4.8 \pm 2.7) \times 10^{-6}$ Nm^{-1}, respectively [32].

1.2.5 Reflection interference contrast microscopy

Reflection interference contrast (RIC) microscopy can be used to calculate the RBC's bending modulus through measurements of the RBC's mean square height fluctuations, $\langle |U(q)|^2 \rangle$. For a RBC enclosed in a cover slip/microscope slide chamber, an incident light beam is reflected at both the cover slip boundary and the RBC boundary. The interference of the two reflected beams creates a Newton ring diffraction pattern from which $\langle |U(q)|^2 \rangle$ can be calculated. In the short wavelength approach, $U(q)$ is the Fourier transform of the RIC image which allows for easy obtainment of $\langle |U(q)|^2 \rangle$. The analysis of the long wavelength regime is slightly more complicated, as in this regime a surface profile of the cell can be reconstructed. Here, $\langle |U(q)|^2 \rangle$ is obtained from the difference between two consecutive surface profiles. The bending modulus, κ, is related to $\langle |U(q)|^2 \rangle$ through:

$$\kappa = \frac{k_b T}{S q^4 \langle |U(q)|^2 \rangle} \tag{1.10}$$

where S is the observed surface area and q is the wavevector, and all other variables having their usual meanings [33]. Using RIC, Zilker *et al.* [34] measured a value of $\kappa = (3.4 \pm 0.8) \times 10^{-20}$ J.

1.2.6 Electrodeformation

Electrodeformation takes advantage of the Maxwell-Wagner polarisation effect to inflict a force upon a fixed RBC and hence, measure its shear modulus. In this technique an electric field is applied which fixes the RBC to a wedge-shaped electrode, and deformations are induced by varying the field strength. The Maxwell-Wagner polarisation effect is applicable since there is a difference between the conductivity of the cell's cytoplasm and the surrounding medium; the resulting force is calculated by treating the cell as a conducting body in a dielectric field. The shear modulus is quantified by using fast image processing to measure the elongation of the cell as a

function of the electric (Maxwell) tension. Using this method, a shear modulus of μ = 6.1×10^{-6} Nm^{-1} was obtained for the RBC [35].

1.2.7 Summary

The techniques that have been described in this section and the corresponding reported values of the elastic moduli, are summarised in Table 1.1. Whilst there are a number of techniques available to the individual for probing the RBC's elastic moduli, it becomes clear that reported values can differ between techniques. These inconsistencies often arise as a result of the assumptions made in applying a theoretical approach to the analysis of the practical measurement. This therefore remains an area of intense investigation, both theoretically and experimentally.

Table 1.1: ***Summary of reported RBC elastic moduli.*** *Note that for clarity, error margins are not presented here but can be found within the text.*

Method	**K** $\mathbf{Nm^{-1}}$	κ **J**	μ $\mathbf{Nm^{-1}}$	**Reference**
Micropipette aspiration	0.45	1.8×10^{-19}	6.6×10^{-6}	[24, 27, 28]
Direct optical trapping	-	-	1.3×10^{-5}	[29]
Indirect optical trapping (two beads)	-	-	2.05×10^{-6}	[30]
Indirect optical trapping (three beads)	4.8×10^{-6}	-	2.4×10^{-6}	[32]
RIC microscopy	-	3.4×10^{-20}	-	[34]
Electrodeformation	-	-	6.1×10^{-6}	[35]

1.3 RBC as moderator of vascular tone

Quantifying the mechanical properties of the RBC is an important factor in understanding the physiological behaviour of the cell. It is well recognised that the cell is subjected to extreme deformations as it traverses the circulatory system, and that abnormalities in its elastic behaviour can have significant impacts on O_2 transport. More specifically, abnormalities in cellular mechanics could impact the RBC's ability to dynamically control localised blood flow through altered ability to release the vasodilator adenosine triphosphate (ATP).

Suggesting that the RBC has the ability to dynamically control local blood flow is a major shift from considering the RBC as simply a passive O_2 transporter. However, it is now widely accepted that ATP release from the RBC is stimulated by a number of physiological conditions such as small changes in pH [36], oxygen concentration [37], osmotic pressure [38] and mechanical deformation of the cell [39]. The significance of these findings is apparent through the involvement of ATP in the vasodilation of blood vessels. It is thought that ATP binds with purinergic receptors on the endothelial wall, initiating an endothelial- and smooth muscle cell-dependent vasoactive response that can be conducted upstream [40].

However, the signalling pathway within the RBC that links the physical stimuli to the release of ATP, remains under some debate and often varies between stimuli. Further, in the case of stimulation via mechanical deformation, there is insubstantial evidence over which specific elastic property of the RBC dominates the signalling response. Research to clarify this could help explicate the dominant signalling pathway.

1.4 Clinical relevance

The RBC's ability to both monitor and respond to local O_2 demand raises important questions about the clinical relevance of this mechanism. It would be anticipated that such an intricate mechanism as this could be implicated in a diseased state. Further, it follows that an increasing number of human diseases - such as diabetes mellitus, cystic fibrosis, malaria, sickle cell anaemia and renal failure - are being associated with abnormalities in the RBC [41]. Since the RBC is no longer considered as simply a passive carrier of O_2, its role in regulating the circulatory system could be significantly impacted by these abnormalities. A complete understanding of this control mechanism could lead to new therapeutic approaches in treatment of the following diseases.

1.4.1 Diabetes mellitus

Diabetes mellitus, commonly called diabetes, is a disease in which the body fails to regulate blood sugar levels, either through inability to produce insulin or failure to produce enough/respond to insulin. It is a lifelong condition which if managed poorly, can lead to many secondary complications. Some of these complications are a result of impaired microvasular function as cells become glycated and oxidised.

Previous studies on RBCs from diabetic patients have shown reduced deformability of the cells [42] and in particular, an increased shear modulus [26]. Parallel to this, a 78% decrease in ATP released from RBCs of diabetic patients, as opposed to healthy controls, has been reported [43]. It would appear that no link has yet been established between the reduced deformability and the lack of ATP release in RBCs from diabetic patients.

1.4.2 Cystic fibrosis

Cystic fibrosis (CF) is a hereditary disease caused by a recessive gene mutation which controls the movement of salt and water across the cell membrane. As a result of the mutation, a thick mucus builds up in the lungs of CF patients. Not only does this reduce the lung capacity, the mucus is also largely responsible for secondary complications associated with CF.

The faulty gene is responsible for the cystic fibrosis transmembrane conductance regulator (CFTR) protein, with CF patients lacking this protein. RBCs from CF patients have been shown to release less ATP than control RBCs when subjected to mechanical deformation [44]. However, in contrast to the RBCs of diabetic patients, the deformability of a CF human RBC remained consistent with that for the healthy control. This work implicates the CFTR protein in the signalling pathway, linking stimulation to ATP release.

1.4.3 Idiopathic pulmonary arterial hypertension

Idiopathic pulmonary arterial hypertenstion (IPAH) is an incurable disease in which the vascular system of the lungs is subjected to increased resistance, causing an increase in blood pressure. The reduced blood flow can lead to damage of the right side of the heart, as it works harder to pump blood in the direction of the lungs.

Further hindering blood flow is the reduced ability of RBCs from patients with IPAH to release the vasodilator ATP upon mechanical stimulation [45]. This study also found these RBCs to have a decreased deformability, in comparison to healthy controls.

1.5 Thesis outline

This project serves to elucidate the link between the RBC's mechanical properties and mechanically stimulated ATP release from the cell. The starting focus of the work, through use of model monolayer phospholipid systems and x-ray crystallography, was to investigate the in-plane structure and electron density profile of the RBC plasma membrane. The work then moved to quantifying the response of the RBC membrane elastic moduli upon chemical insult, through thermal fluctuation studies. Chemical treatments were chosen for their demonstrated targeting of specific structural components of the RBC membrane. The design is such that the contribution of each structural component to the cell's overall deformability could be established. The final area of focus for this work was the RBC's ability to release ATP, stimulated by mechanical deformation. Investigated using both pure blood and samples spiked with the same chemicals as for the fluctuation studies, enabled comparison between changes in the mechanical properties of the cell and altered ATP release. In all stages of the project, further inquiry included detailing the effect(s) of dimethyl sulphoxide (DMSO) on the RBC membrane in an attempt to justify and provide basis for the solvent's many uses in the biological and pharmacological fields.

2 Methods

This chapter provides a comprehensive overview of the techniques that were applied in the mesoscale and whole cell study of the human red blood cell (RBC). The theoretical background underpinning each approach is first described, followed by an outline of the protocols for sample preparation and measurement and then finally, details of the analysis. Techniques relating to the mesoscale studies are presented first, followed by the whole cell techniques comprising of thermal fluctuation spectroscopy (TFS) and measurements of mechanically stimulated adenosine triphosphate (ATP) release.

2.1 Mesoscopic techniques

This section details the techniques used to probe the mesoscale properties of the RBC. All techniques described here are performed on phospholipid monolayers composed of various lipid species, chosen specifically to replicate the behaviour of the RBC membrane. Monolayers are one of the most commonly used methods when investigating lipid composition and structural organisation of the membrane.

2.1.1 Langmuir trough

Many characteristics of monolayers can be probed using a Langmuir trough, a high precision instrument that utilises the hydrophobic nature of the phospholipid acyl chains to form a monomolecular lamination of lipids at an air-subphase interface.

The trough is constructed from a shallow bath, movable barriers and a pressure probe, as seen in Figure 2.1. The trough components (bath and barriers) are made using PTFE, due to the fluorocarbon's highly inert and hydrophobic properties [46]. The bath is filled with a fluid subphase until a meniscus is formed, at which point phospholipids in a chloroform solution are spread over the subphase surface. The formation of the subphase meniscus is vital to ensure no lipid leakage from the experimental area, between the barriers.

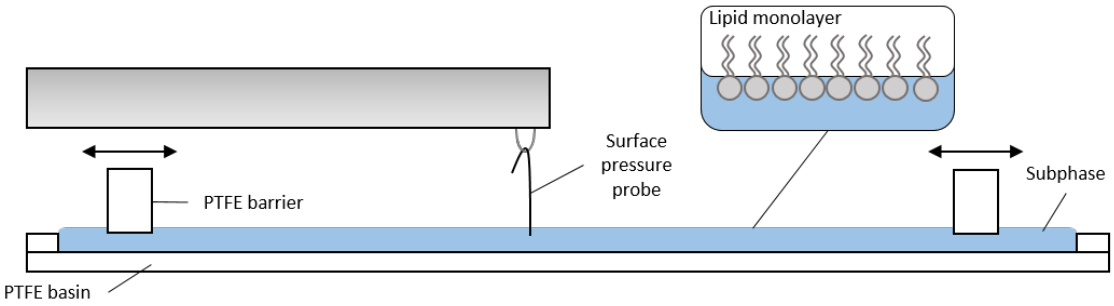

Figure 2.1: ***Langmuir trough schematic.*** *The PTFE barriers move to increase or decrease the surface area available to the lipid molecules. The surface pressure probe relays the 2D surface pressure of the monolayer to a computer, where surface area is also recorded.*

Moving the barriers changes the area available to the phospholipids which in turn, affects the lipid packing, phase state, and surface pressure. Surface pressure, Π, is defined as the difference between the surface tension of the pure water surface, γ_0 (72.8 mN/m at 20°C), and the surface tension of the lipid monolayer, $\gamma(c)$, where c is the surface concentration of the lipid [47]:

$$\Pi = \gamma_0 - \gamma(c). \tag{2.1}$$

Π is recorded via the surface balance probe which must be fully wetted by, but not submerged in the air-subphase interface. Isotherms are the graphical representation of Π, measured as a function of the area per molecule, A. An idealised isotherm is presented in Figure 2.2, detailing the various phases of phospholipid organisation resulting from changing A.

Phospholipids are generally applied to the subphase surface in a chloroform solution using a glass syringe, droplet at a time and with the barriers at maximum spacing, A_{max}. This creates a monolayer under low pressure, with the lipids forming a two dimensional gas structure (inset, Figure 2.2). As the barriers are moved towards each other decreasing A, Π increases and the monolayer condenses through a first-order transition into the liquid expanded phase. A further decrease in A initiates another first-order transition, through a stage of phase coexistence, between the liquid expanded phase and a low ordered condensed phase. Continuing the decrease of A finally initiates a second-order transition, characterised by a sharp increase in Π and eventual monolayer collapse.

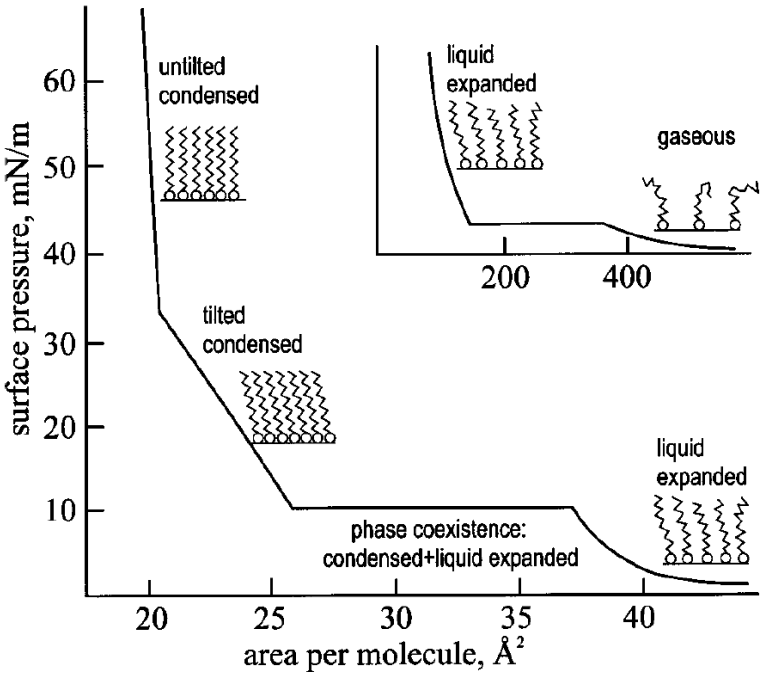

Figure 2.2: ***Idealised Langmuir monolayer isotherm.*** *Phase changes are depicted as gradient kinks, whilst the horizontal section relates to phase coexistence. The monolayer passes from a gaseous configuration at large area per molecule to a condensed phase at small area per molecule, as the the barriers are moved closer together. Modified from* [48].

2.1.2 Synchrotron geometries

Synchrotrons are cyclic particle accelerators that produce intense beams of light as a by-product of deflecting the particle beam around their storage ring. The energy spectrum of this light ranges from infrared to x-rays. As the wavelength of the x-ray is comparable to the molecular dimensions of a monolayer, several techniques used to characterise Langmuir monolayers have exploited this deflection by-product. Below are three examples of these techniques as used in the experiments presented within this thesis. A schematic of each geometry is presented in Figure 2.3.

Grazing incidence x-ray diffraction

Grazing incidence x-ray diffraction (GIXD) probes the lateral ordering in a monolayer. This method provides information on the 2D crystalline structure and phospholipid acyl chain orientation within the sample [49]. As the name suggests, the incident beam is diffracted off the monolayer surface at an angle close to the critical angle for total internal reflection. This geometry reduces the penetration of the beam to an evanescent wave and assists in maximising the signal to noise ratio [50].

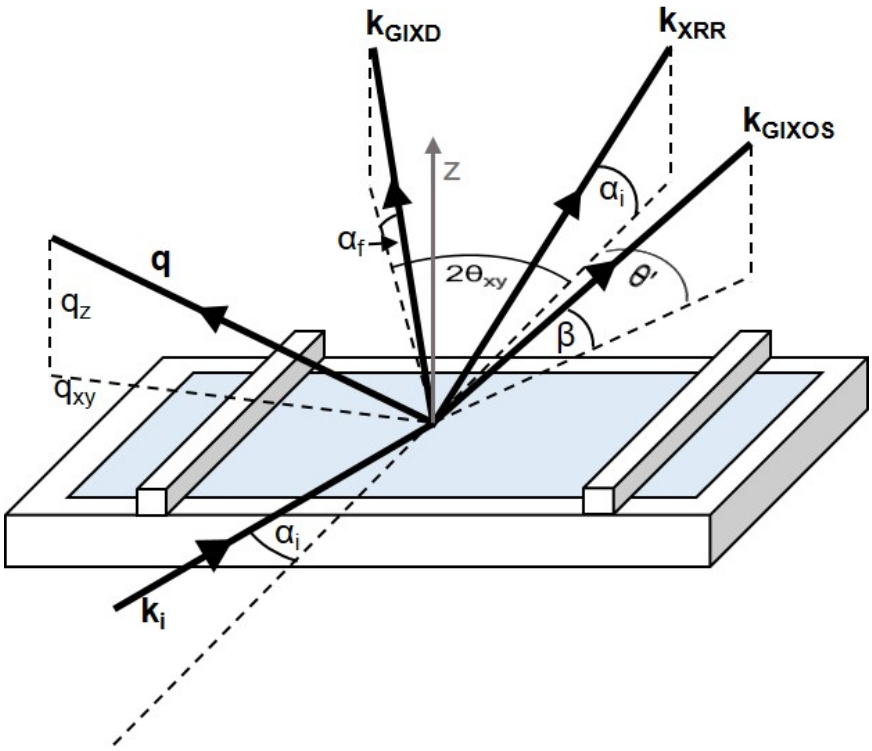

Figure 2.3: ***Synchrotron scattering geometries.*** *In GIXD experiments the incident beam, $\boldsymbol{k}_{\mathrm{i}}$, is diffracted at an in-plane angle of $2\theta_{xy}$ along $\boldsymbol{k}_{\mathrm{GIXD}}$. The measured intensity is a function of the momentum transfer $\boldsymbol{q}$ between the two beams. XRR measurements are made along the same trajectory as the incident beam, as shown by $\boldsymbol{k}_{\mathrm{XRR}}$. In the GIXOS geometry, the scattered beam is measured at an in-plane angle θ', as shown by $\boldsymbol{k}_{\mathrm{GIXOS}}$.*

The arrangement of phospholipids on the subphase surface is considered a mosaic of crystallites, i.e. the crystalline structure domain size is finite. Therefore, the monolayer is described as a 2D powder and the diffraction pattern is averaged over all possible domains (known as powder averaging) [48]. In real space any crystalline structure is fully described by the lattice parameters and basis. The lattice parameters consist of the unit cell primitive lattice vectors, $\mathbf{a}$ and $\mathbf{b}$, and the angle between them, γ, and for this example the basis is assumed to be one lipid molecule per lattice point. Any position within the lattice is given by $\mathbf{r} = u\mathbf{a} + v\mathbf{b}$ (where u, v are arbitrary constants) and the area of the unit cell is defined as $A = ab\sin(\gamma)$.

Lattice structures are also defined in reciprocal space by the reciprocal lattice vector $\mathbf{G}_{h,k} = h\mathbf{a^*} + k\mathbf{b^*}$, where h, k are the Miller indices and $\mathbf{a^*}$, $\mathbf{b^*}$ are the reciprocal primitive lattice vectors. Appreciable diffraction will only occur within the 2D lattice when $\mathbf{G}_{h,k}$ is equal to the scattering vector $\mathbf{q} = \mathbf{k}_{\mathrm{f}} - \mathbf{k}_{\mathrm{i}}$ [51]. Here, $\mathbf{q}$ corresponds to the momentum transfer of the scattered (f) and incident (i) wave vectors, $\mathbf{k}_{\mathrm{i,f}}$. This geometry is defined in Figure 2.3 for $\mathbf{k}_{\mathrm{f}} = \mathbf{k}_{\mathrm{GIXD}}$.

Due to powder averaging the measured diffracted intensity can only be resolved into two out of the three dimensional components. The out-of-plane component, q_z, is characterised by the angle between the scattered beam and subphase surface, α_f, whereas the in-plane component, $q_{xy} = (q_x^2 + q_y^2)^{1/2}$, is characterised by the angle between the incident and scattered beam in the plane of the subphase surface, $2\theta_{xy}$ (see Figure 2.3). That is:

$$q_z = \frac{2\pi}{\lambda} \sin \alpha_\mathrm{f} \qquad \text{and} \qquad q_{xy} = \frac{4\pi}{\lambda} \sin \frac{2\theta_{xy}}{2}. \tag{2.2}$$

Raw GIXD images were first processed to produce 2-D heatmaps of the intensity in the q_z and q_{xy} directions. This intensity was then integrated over, producing either Bragg rods or Bragg peaks. When integrated over q_{xy} with projection onto the q_z axis, the data is presented as a Bragg rod. The inverse, integration over q_z and projection onto the q_{xy} axis, is a Bragg peak [49]. These stages of analysis were performed using custom MATLAB scripts (C. Shen, DESY).

Phospholipid acyl chain orientation is observed from the position and quantity of Bragg rod maxima, but can also be inferred from the 2-D heatmaps. There are 4 possible tilt orientations, each with a unique Bragg rod pattern. A single Bragg rod centred at $q_z = 0$ is indicative of the untilted phase. Here, the peak is inferred as sixfold degenerate due to the lines of symmetry that exist within the crystalline structure. Any deviation from the untilted arrangement leads to the lifting of this degeneracy and therefore, the presence of more Bragg rod maxima at higher q_z (corresponding peaks that would exist at $q_z < 0$ are not observed in measurement), as demonstrated by Ocko *et al.* [52]. A nearest-neighbour tilt is characterised by a rod centred at $q_z = 0$, followed by a degenerate rod at higher q_z. Alternatively, if the first maximum exists at $q_z > 0$ and there exists a second maximum at even greater q_z, the lipid tilt orientation is said to be towards the next-nearest-neighbour. This time the peak at lower q_z is the doubly degenerate peak. In the case of an intermediate tilt the degeneracy is completely broken and three separate Bragg rods will be observed at values of $q_z > 0$. In each case the maxima must satisfy the condition $q_{1z} + q_{2z} = q_{3z}$, where q_{3z} is the largest value of the three.

The Bragg peaks were fitted with a Lorentz profile (B. McGill) to extract their position and full width at half maximum (FWHM). The peak position, q_{xy}, is related to

the lattice d-spacing and $|\,\mathbf{a}\,|, |\,\mathbf{b}\,|, \gamma$, through:

$$d = \frac{2\pi}{q_{xy}} = \left[\frac{h^2}{a^2} + \frac{k^2}{b^2} - 2\left(\frac{hk}{ab}\right)\cos(\gamma)\right]^{-1/2} \sin(\gamma). \tag{2.3}$$

To enable calculation of a and b, each peak must be indexed by a set of Miller indices, $\{h, k\}$. As with Bragg rods, peaks can be degenerate and therefore indexed with multiple $\{h, k\}$. Indexing allows for Equation 2.3 to be solved for a, b and γ simultaneously and in turn, calculation of the area of the unit cell, $A = ab\sin(\gamma)$. The physical significance of A is the area occupied by one acyl chain of a phospholipid molecule, giving the area per molecule as $2A$. The FWHM of the peak determines the length over which the crystalline domain structure is valid (crystallite dimensionality), known as the coherence length:

$$L_c = 0.9\frac{2\pi}{FWHM(q_{xy})}. \tag{2.4}$$

X-ray reflectivity

X-ray reflectivity (XRR) is used to probe the electron density of thin films perpendicular to the air-subphase interface. X-rays are specularly reflected from the sample surface and the intensity of the reflected beam recorded (Figure 2.3, $\mathbf{k}_{\mathrm{XRR}}$). For an abrupt change in refractive index, n, at the interface, a reflection would follow the law of Fresnel reflectivity. With α and α' defined in Figure 2.4, it can be shown that the Fresnel reflectivity coefficient, $\mathcal{R}_F$, is defined as [53]:

$$\mathcal{R}_F = \left|\frac{\alpha - \alpha'}{\alpha + \alpha'}\right|^2 \tag{2.5}$$

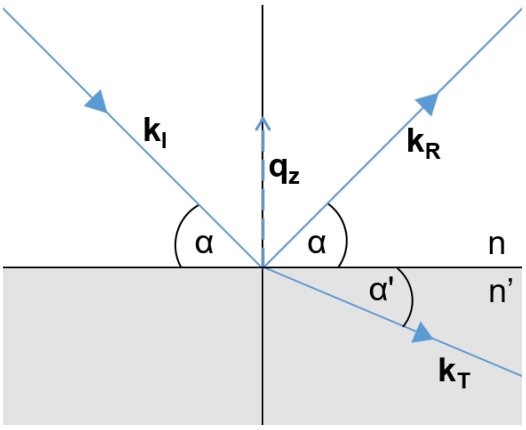

Figure 2.4: ***Specular Reflection.*** *An incident wave, $\boldsymbol{k}_{\mathrm{I}}$, will reflect under Fresnel conditions at an interface with an abrupt change in refractive index, n. Adapted from* [53].

However, the addition of phospholipids to the surface of the subphase smooths the change in refractive index across the interface. This perturbs the experimentally

measured reflectivity from the Fresnel reflectivity as:

$$\mathcal{R}(q) = \mid \phi(q') \mid^2 \mathcal{R}_F(q). \tag{2.6}$$

Where q is the wave vector transfer, q' is that inside the material, and $\phi(q')$ is defined as the Fourier transform of a function of the electron density profile, ρ_e, and its average ρ_{av} [53]:

$$\phi(q') = \mathcal{F}\left(\rho_{av}^{-1}\frac{\partial \rho_e}{\partial z}\right). \tag{2.7}$$

Since $\mathcal{R}_F(q)$ can be calculated for a given interface, an XRR measurement results in the left hand side of Equation 2.6, for which Equation 2.7 can then be used to obtain an electron density profile of the monolayer perpendicular to the interface.

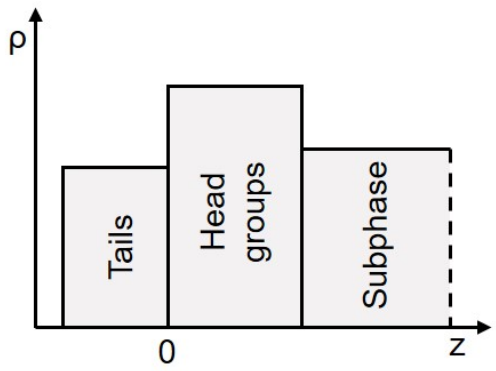

Figure 2.5: ***Slab model representation.*** *Each layer of the interface is represented as a slab with set thickness d, where the subphase is taken to have near infinite thickness. A Gaussian smoothing parameter is used to smooth the resulting ρ_e between the slabs.*

XRR data were analysed using custom built software (O. Konovalov, ESRF). The software inverted the XRR measurements to obtain ρ_e using the slab model regression approach. In this model the interface is split into a number of homogeneous slabs of thickness d, that represent each region of the phospholipid molecule (acyl chain and head group) and the subphase, as shown in Figure 2.5. Each slab has an associated refractive index and Gaussian smoothing parameter, σ. The latter of these is incorporated into the model since a physical interface is less abrupt than the rigid boundaries of each slab block within the model. As slab thickness is an output parameter from the fit, an overall film thickness can be calculated. The fit of the reflectivity curve is then inverted to obtain an electron density profile of the monolayer perpendicular to the interface.

Grazing incidence x-ray off-specular scattering

Similar to XRR, grazing incidence x-ray off-specular scattering (GIXOS) is used to define the electron density profile of a monolayer perpendicular to the air-subphase interface. Due to only needing a single exposure and as such no adjustment of the beam, sample or detector, GIXOS is fast becoming the preferred method of the two. These advantages significantly reduce the measurement time and consequently x-ray induced sample degradation [54].

The experimental set-up is near identical to that of XRR, only for GIXOS the azimuth angle, θ', in Figure 2.3 is now non-zero ($\mathbf{k}_{\mathrm{GIXOS}}$). This off-specular geometry requires guard slits to minimise the level of specular reflection reaching the detector and hence increase the signal ratio of the off-specular scattered beam.

The measured GIXOS intensity is proportional to the ratio of the XRR measured reflectivity and the Fresnel reflectivity, perturbed by a characteristic Vineyard Function for the grazing incidence configuration [55]:

$$I(q_z) \propto |T(k_{out})^2| \frac{\mathcal{R}(q_z)}{\mathcal{R}_F(q_z)}. \tag{2.8}$$

Employing Equation 2.7, the so-called Master Formula of specular reflectivity, the GIXOS measurement can be inverted to obtain the electron density profile, ρ_e.

GIXOS data were analysed in a three step process. The first two stages used custom MATLAB scripts (C. Shen, DESY) to convert the raw measurement to GIXOS data and then into a pseudo-reflectivity curve (by rearrangement of Equation 2.8 for $\mathcal{R}(q_z)$). Once the pseudo-reflectivity had been obtained, the analysis followed the same slab model method as described for the analysis of the XRR data.

2.2 Whole cell methods

The techniques used to study RBCs at whole cell level are outlined here. Both single cell and whole blood methods are described in detail, including theoretical background, data acquisition and processing.

2.2.1 Thermal fluctuation spectroscopy

The RBC membrane is soft, enough so that the thermal energy available at room temperature will cause membrane thermal fluctuations. Optical microscopy techniques can be used to observe the amplitudes of these undulations, which provide information on the elastic parameters of the membrane. Developed in our laboratory, this technique is known as thermal fluctuation spectroscopy (TFS). In the TFS theory the plasma membrane is considered in Monge representation as a 2-D free surface in the x-y plane with height, $h(x, y)$, above the plane, such that a point on the surface would have coordinates $\mathbf{r} = [x, y, h(x, y)]$. The surface has an associated bending modulus, κ, and mean curvature, $H(r)$, defining the bending free energy of such a surface as

$$F_\kappa = \frac{\kappa}{2} \oint dA\big[2H(r)\big]^2. \tag{2.9}$$

The first assumption of this model is that the surface is nearly flat, then $|\nabla h| \ll 1$. Equation 2.9 is then better expressed in terms of the Monge parameters in $\mathbf{r}$, where L is a dimension of the surface:

$$F_\kappa = \frac{\kappa}{2} \int_0^L \int_0^L \big[\nabla^2 h(x, y)\big]^2 dxdy. \tag{2.10}$$

Secondly, the TFS model assumes that the ends of the surface are pinned. This results in a surface tension, σ, that acts to maintain the surface area and introduces a second energy term into the model:

$$F_\sigma = \frac{\sigma}{2} \iint \big[\nabla h(x, y)\big]^2 dxdy. \tag{2.11}$$

The Helfrich free energy, F_H, of a fluid membrane under tension is then the sum of Equations 2.10 and 2.11. Since frequencies are used to describe the physical fluctuations of the membrane, it is advantageous to use the Fourier transform of $h(x, y)$, $h(\mathbf{q})$, in the Helfrich free energy:

$$F_H = F_\kappa + F_\sigma = \frac{1}{2}\frac{A^2}{4\pi^2} \int d\mathbf{q}\big(\sigma q^2 + \kappa q^4\big) h(\mathbf{q}) h^*(\mathbf{q}). \tag{2.12}$$

As each Fourier mode is independent and harmonic in nature, the equipartition theorem can be applied. This assigns an average energy of $k_B T/2$ for each mode and the

mean square amplitude of $h(\mathbf{q})$ can be calculated:

$$\langle |h(\mathbf{q})|^2 \rangle = \frac{k_B T}{\sigma q^2 + \kappa q^4}. \tag{2.13}$$

Thus far, the contribution of the cytoskeleton to the free energy of the cell has been ignored. This vital component of the cellular structure introduces a harmonic confinement potential, γ, resulting from the minimal connections between the cytoskeleton and lipid bilayer [56]. Equation 2.13 is modified to:

$$\langle |h(\mathbf{q})|^2 \rangle = \frac{k_B T}{\sigma q^2 + \kappa q^4 + \gamma}. \tag{2.14}$$

The above equation therefore details the relationship between the mean square amplitudes and elastic moduli of the fluctuating system. Treating the cellular membrane as a composite structure, with a fluid phospholipid bilayer and solid cytoskeleton, Auth *et al.* [57] were able to show that the shear elasticity, μ, of the cytoskeleton is derived from its relationship with the membrane tension:

$$\sigma = \frac{9\mu k_B T}{16\pi\kappa}. \tag{2.15}$$

Experimentally, fluctuations are only measured in the equatorial plane of the cell (Figure 2.7). Therefore, the experimental contour shape can be represented by a Fourier series in polar coordinates (r, θ):

$$r(\theta) = R\Big\{1 + \sum_n \big[a_n \cos(n\theta) + b_n sin(n\theta)\big]\Big\}, \tag{2.16}$$

where R is the cell radius. In this geometry, fluctuations are quantified around the mean shape of the contour by the Fourier amplitudes a_n and b_n, such that $\langle c_n^2 \rangle = \big[\langle a_n^2 \rangle - \langle a_n \rangle^2\big] + \big[\langle b_n^2 \rangle - \langle b_n \rangle^2\big]$.

It remains that Equation 2.14 must then be converted to represent the fluctuation spectrum of an equatorial contour. To do so it is transformed into real space under the assumption that one of the coordinates (y) equals zero, thus defining a fluctuating line. The 2-D equatorial contour fluctuation spectrum accounting for the contour

representation is then [58, 59]:

$$\langle c_n^2 \rangle = \frac{1}{2\pi} \frac{1}{\widetilde{\kappa}\sqrt{\widetilde{\sigma}^2 - \widetilde{\gamma}}} \left[\left(\widetilde{\sigma} + n^2 - \sqrt{\widetilde{\sigma}^2 - \widetilde{\gamma}} \right)^{-1/2} - \left(\widetilde{\sigma} + n^2 + \sqrt{\widetilde{\sigma}^2 - \widetilde{\gamma}} \right)^{-1/2} \right]. \quad (2.17)$$

Here, the tilde mark denotes a dimensionless variable, such that $\widetilde{\kappa} = \kappa / k_B T$, $\widetilde{\sigma} = \sigma \langle R \rangle^2 / 2\kappa$ and $\widetilde{\gamma} = \gamma \langle R \rangle^4 / \kappa$, for simplicity in the above equation. These parameters are obtained through a least squares regression fit of Equation 2.17 to the Fourier amplitudes obtained experimentally through Equation 2.16. Further, the membrane tension, σ, is used to obtain the membrane shear modulus, μ, using Equation 2.15. The analysis of fluctuation spectra is described in more detail later in this section.

TFS also offers a more sensitive measure of overall cell fluctuations in parallel to the mode-decomposed fluctuation analysis described previously. This is achieved through analysis of the cell radius normalised to the average cell radius at a set angle; $r(\theta)/\langle r(\theta) \rangle$. Normalised radii over all angles are combined into a single histogram, with the overall degree of fluctuation given by the standard deviation of the probability density function that describes the resulting normal distribution:

$$p(x) = \frac{1}{\sigma_r \sqrt{2\pi}} \exp\left(-\frac{(r - r_0)^2}{2\sigma_r^2} \right). \quad (2.18)$$

Blood sample preparation

A fresh blood sample was collected immediately before the experiment by use of a pin-prick lancet device (Multiclix, Accu-Chek, UK). Approximately 1.5 µL of blood was suspended in 1 mL of phosphate-buffered saline (PBS; 0.01 M, pH 7.4, Sigma-Alrich, USA) with 1 g/L bovine serum albumin (BSA; VWR Life Science, UK) added. The PBS and BSA (buffer) maintained the cells in their natural discoid shape, counteracting the "glass effect" [60]. The concentration of the blood/buffer solution prevented aggregation of cells allowing for individual cells to be observed under the microscope.

Each blood donation was in accordance with UK ethics regulations (University of Exeter eEthics ID: eEMPS000064). The participant was informed of the basis of the study and provided the researchers with minimal personal information such as gender and year of birth. The female participant had no underlying health conditions.

Slide preparation

Microscope chambers were assembled from a microscope slide and cover slip (both Fisher, UK). The slide and cover slip were rinsed in a chloroform : methanol solution (3:1), air dried, and then assembled using two strips of parafilm (Starlab International GmbH, Germany) to seal the chamber along the two longer edges of the slide (Figure 2.6). This configuration gave a chamber volume of approximately 220 μL and allowed for exchange of the buffer solution during the experiment.

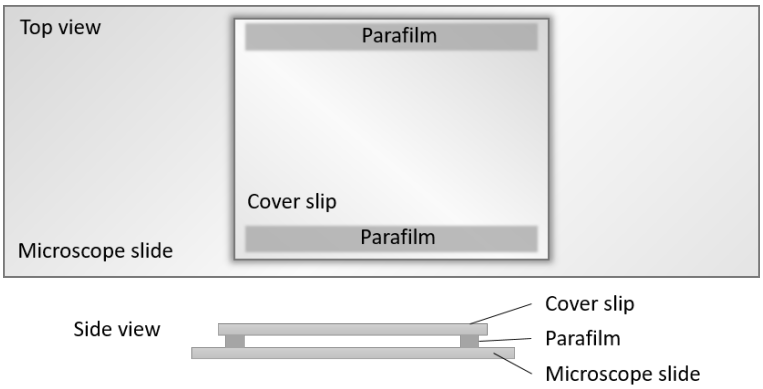

Figure 2.6: ***TFS slide preparation.*** *Schematic detailing the arrangement of the microscope slide and cover slip, creating a partially open chamber for buffer exchange during experiments.*

Measurement Protocol

20 μL of the blood/buffer solution were transferred to the microscope chamber, where capillary forces drew the solution through the chamber. After allowing the cells to settle for 5 - 10 minutes, a further 200 μL of buffer was added to the chamber, counteracting the effects of evaporation for the duration of the experiment.

To observe the cell fluctuations, the microscope chamber was placed on the stage (MS-2000, ASI Imaging, USA) of an upright microscope (DMLFS, Leica) housing a 63x PL Fluotar phase-contrast objective (Leica). Fast-video phase contrast microscopy was used to obtain a 2000 frame video, at 10 ms exposure time, of a single RBC. This was repeated to observe several cells within the same sample.

After the initial video of each cell had been recorded, the buffer was exchanged with that containing a chemical treatment. To ensure complete buffer exchange, 2 mL of the new buffer was flushed through the chamber by addition on one of the open sides of the chamber, then using tissue paper to aid the through-flow on the other side.

Once the buffer was fully exchanged, each cell was further imaged at 10 or 20 minute intervals for up to 90 minutes. This method allowed for single cell analysis, where comparisons could be made for the same cell before and after treatment, negating the time consuming need for a large population of cells to be analysed and avoiding cell to cell variability.

Data analysis

Data analysis of the TFS videos is a multi-stage process that amalgamates the work of several members of this laboratory. In the first stage, the single-frame equatorial contours of a cell are extracted using a custom built ImageJ plugin (J. Hale). The plugin allows for sub-pixel resolution of the contours by fitting an intensity profile of the equator of the cell with a cubic polynomial and taking the minimum of the polynomial as the contour point, demonstrated by Figure 2.7.

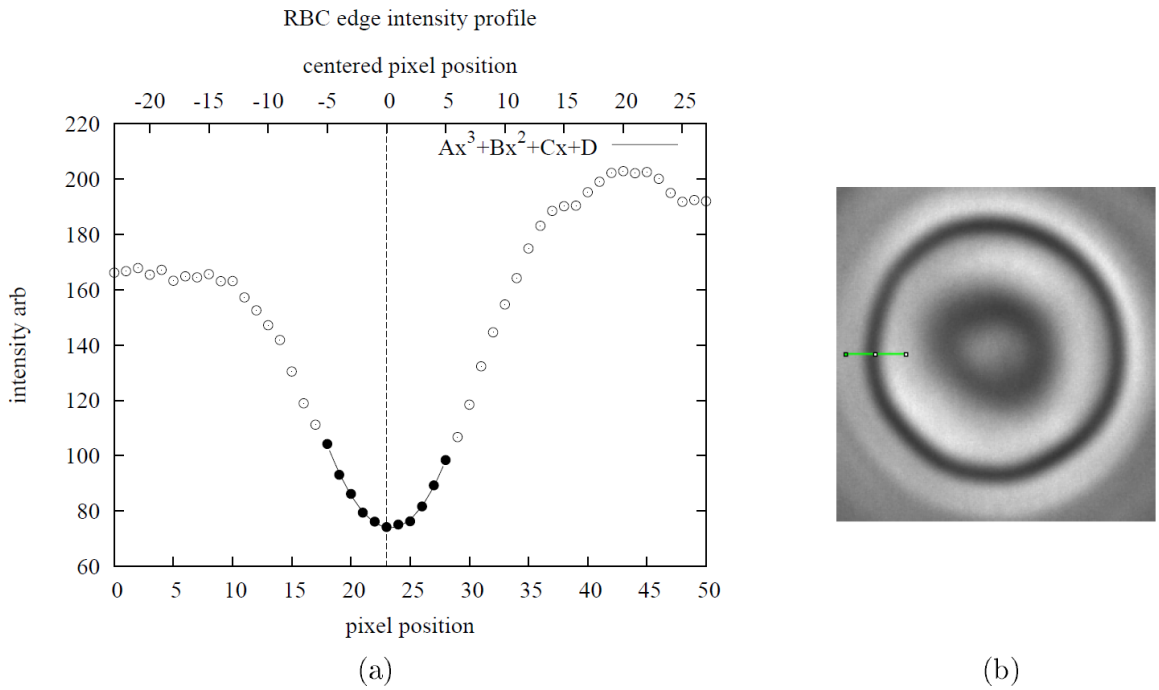

Figure 2.7: ***TFS contour extraction algorithm.*** *(a) The intensity profile fitted with a cubic polynomial. Obtained from an equatorial slice of the membrane as demonstrated in green in the phase contrast image (b)* [3]. *Scale: 30 px = 1 µm.*

The Fourier transform programme of stage 2 (D. Woods) converts the contour file into a Fourier series, as described by Equation 2.16, and then extracts the amplitudes a_n and b_n needed to calculate the fluctuation spectra. Here, the average radius of each cell is also calculated in pixels.

The third and final stage utilises a non-linear regression fitting programme (B. McGill, see Appendix A) written in python to extract numerical values of the moduli. The elastic moduli are obtained from fitting Equation 2.17 to the experimentally obtained fluctuation amplitudes. Here, the input parameters were passed through an iterative modification to minimise the sum of the normalised error squared values (difference between the theoretical and experimental data sets). The bending modulus, κ, and an associated error were obtained directly from the fitting procedure, whilst the shear modulus, μ, was calculated from Equation 2.15 with the error propagated through.

Four chemical treatments were investigated, each at three or five concentrations. Under each condition a minimum of 5 cells where analysed, with the fluctuation spectra and normalised radii histograms presented being representative of the typical observed behaviour. Elastic moduli were obtained for each individual cell and normalised to the untreated state. An average of the normalised elastic moduli under each condition have been presented in Chapter 4, with standard error as the experimental uncertainty. Furthermore, the normalised standard deviations, obtained from the histograms and detailing the kinetics of the cellular response, represent typical behaviour of the sample.

2.2.2 Mechanically stimulated ATP release

A novel shearing device was used to induce mechanically stimulated ATP release from RBCs in the laboratory environment. The physiological conditions were achieved *in vitro* by controlling the shear stress applied to the blood sample through manipulation of several parameters, including sample viscosity, flow rate and cannula length.

Shearing device

The mimicking of blood flow though the circulatory system was achieved by connecting a 3 FG cannula (Portex, Smiths Medical, UK) to a syringe pump (Cole Palmer, USA) that ensured a steady flow through the cannula. A schematic of the device is shown in Figure 2.8.

A system such as this is described by Poiseuille flow, that is the steady, laminar and fully developed flow of a Newtonian liquid along the z-axis of a cylindrical geometry

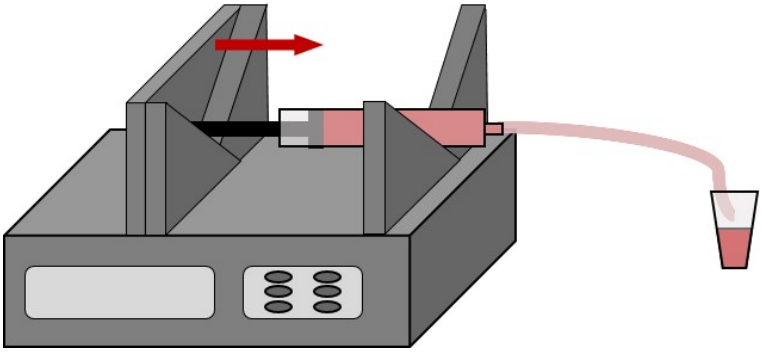

Figure 2.8: ***Schematic of the shearing device.*** *A syringe pump was used to ensure a steady flow of blood through the attached 3 FG cannula. Once the blood had passed though the shearing device it was collected in an Eppendorf tube,ready for immediate measurement.*

of radius R. The velocity profile of the flow is given by the following equation, where Δp is the pressure change and μ the fluid viscosity:

$$v_z(r) = \frac{1}{4\mu}\frac{\Delta p}{L}\left(R^2 - r^2\right), \tag{2.19}$$

The volumetric flow rate for this type of flow can be expressed as:

$$Q = \frac{\pi R^3 |\sigma|}{4\mu}, \tag{2.20}$$

where $|\sigma|$ is the mean shear stress, chosen so that the system was physiologically representative.

Since a syringe pump was used to drive the steady flow, it is more sensible to describe the flow in terms of the speed of the pump, v_p. For a syringe of radius a, Q relates to v_p as:

$$Q = \pi a^2 v_p. \tag{2.21}$$

In a set time frame, t, v_p will correspond to a cross-sectional front of blood flowing a distance, L, through the cannula:

$$L = \frac{v_p a^2 t}{R^2}. \tag{2.22}$$

The experimental variables for the system are then L, t and σ. Once these have been established, v_p can be calculated. The work of Forsyth *et al.* [61] suggested that $\sigma >$

3 Pa (regime III) be sufficient enough to produce an ATP release above a base level. To be sure this system is of physiological relevance and sits well within Forsyth's proposed regime III, the shear stress inflicted upon the flow was set to $\sigma = 5$ Pa. Also in line with Forsyth's system, the shearing time frame was set to $t = 30$ s.

Buffer viscosity

For a simple PBS buffer akin to that used in the TFS experiments, the viscosity would be similar to that of water at $\mu \approx 0.9$ mPa s. As previously mentioned, a 3 FG cannula was used for this system which has an inner radius of $R \approx 0.28$ mm. The established variables allow for a calculation of Equation 2.20 and hence, Equation 2.22. This gives the desired cannula length as $L = 41.7$ m, however, the experimental set-up was limited to $L_{max} = 28$ cm. A decreased cannula length could be obtained by an increase in buffer viscosity. L_{max} gives a minimum required buffer viscosity of $\mu_{\text{min}} = 37.4$ mPa s.

It is known that buffer viscosity can be increased with the addition of dextran (high fraction, Acros Organics, USA). Therefore, to establish the relationship between dextran concentration and buffer viscosity, a simple viscosity experiment was performed. Four different dextran concentrations (40, 75, 150 and 200 g/L) were prepared and measured in comparison to PBS, using a standard viscometer. Four measurements of each concentration were taken, where the average and standard deviation error (extremely small) are shown in Figure 2.9. The data indicated a linear relationship of the form $\log_{10} \mu = 0.0075\ c(\text{dex}) + 0.3059$, thus the concentration of dextran required to achieve $\mu_{min} = 37.4$ mPa s was $c(\text{dex}) = 169.1$ g/L.

Blood sample preparation

A fresh blood sample was collected on the day of the experiment by venepuncture. 250 µL of blood was immediately diluted in 950 ml of buffer to form a 1 %-haematocrit (Htc) solution. The buffer contained 1 g/L BSA and 169.1 g/L dextran. The degree of Htc dilution was established in a preliminary experiment comparing %-Htc that had been used in previous studies [61]. This preliminary experiment demonstrated the desired affect of ATP release from a sheared sample at as low as 1 %-Htc, in agreement with Forsyth *et al.* [61]. It was also observed that, since blood was initially drawn from the donor into a neutral tube not containing an anticoagulant, higher %-Htc concentrations experienced clotting.

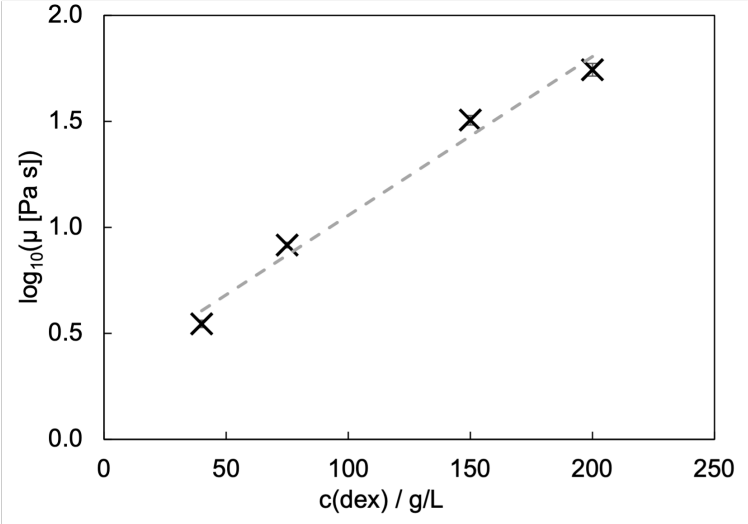

Figure 2.9: ***Buffer viscosity as a function of dextran concentration.*** *The log of the buffer viscosity is increased linearly with increasing dextran concentration. The relationship is described by* $\log_{10}\mu = 0.0075c(dex) + 0.3059$. *Error bars are one standard deviation and lie within point size.*

Blood collection was performed under the same ethics as for the TFS study of Section 2.2.1. Again, minimal personal information about the donor was gathered.

Luminometer assay

Sample ATP was measured using a luminometer (GloMax 20/20, Promega) to collect the luminescent signal produced when luciferin reacts with ATP, as shown by Equation 2.23. Luciferase catalyses the reaction between the ATP and luciferin, producing oxyluciferin in an excited state, adenosine monophosphate (AMP), inorganic pyrophosphate (PP_i) and carbon dioxide (CO_2) [62]. The oxyluciferin subsequently decays to the ground state with the emission of light ($h\nu$):

$$\mathrm{ATP} + \mathrm{D{-}luciferin} + \mathrm{O_2} \xrightarrow[\mathrm{Mg^{2+}}]{\text{luciferase}} \mathrm{Oxyluciferin} + \mathrm{AMP} + \mathrm{PP_i} + \mathrm{CO_2} + h\nu. \tag{2.23}$$

The luminometer follows a 10 measurement, 3s integration time protocol. Per kit instruction and prior to the very first measurement, lyophilised rL/L reagent (Enliten ATP Assay System, Promega) was combined with a reconstruction buffer and allowed to reach room temperature [63]. The rL/L reagent was then divided into several

aliquots to be used throughout the experiment, to prevent bulk deterioration of the reagent.

Measurement protocol

As per the Enliten kit instructions, for a measurement of ATP concentration 100 µL of the rL/L reagent were mixed with an equal amount of sample. Due to the high viscosity of the sample, it was imperative to establish a mixing protocol for when the rL/L reagent was initially added. Three methods of reagent addition were tested; simple addition of the reagent, repeatedly siphoning (using a wide-bore pipette tip) the sample and reagent for 20 seconds after the initial addition and finally, vortexing for 20 seconds after addition. The average of three samples measured using each of the methods is displayed in Figure 2.10, where error bars indicate the standard deviation. Results indicated that vortexing was too vigorous and may have led to the deterioration of the reagent. With no significant difference between the other two methods, simple addition was chosen as the preferred method for its simplicity. This also further prevented excess shearing of the sample as it was siphoned in and out of the pipette tip several times.

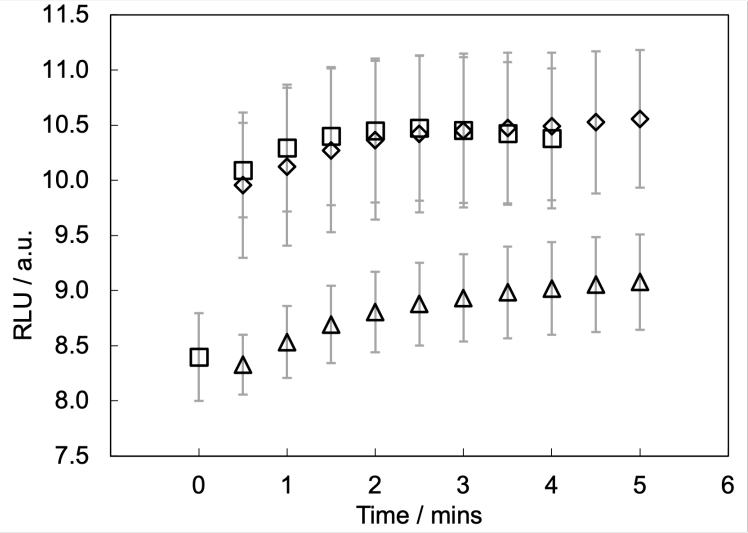

Figure 2.10: ***Methods of addition of the rL/L reagent.*** *Relative luminescent unit (RLU) output measured after adding the rL/L reagent to a sample either by simple addition* (□)*, repeated siphoning* (◊) *or vortexing* (△)*. There was no observed difference between simple addition and repeated siphoning, however vortexing proved too vigorous.*

Relative luminescence unit (RLU) measurements were recorded every 30 seconds from the time of rL/L reagent addition, for up to 4 minutes. This allowed the reagent to

reach saturation with the sample, where it was generally observed that maximum RLU was recorded at $\sim$ 1 minute. Unless otherwise indicated, due to the large variability within the same sample as established in preliminary experiments, five samples were measured under each condition and an average with standard deviation calculated. RLU measurements were made both before and after shearing, with the difference between the two averages indicating the concentration of ATP released during the shearing process. Pure blood samples were measured as a control, allowing for comparison with blood samples that had been incubated with various chemicals for a set amount of time.

Data analysis

An ATP calibration curve was measured each time a new aliquot of rL/L was used, by diluting an ATP standard of $c = 10^{-7}$ M in a dilution series with ATP-free water. This allowed for conversion between RLU from the luminometer and ATP concentration, c(ATP), using Equation 2.24. Here, C_1 and C_2 are constants established from the calibration plot, an example of which is shown in Figure 2.11.

$$log_{10}(\text{RLU}) = C_1 log_{10}\big(c(\text{ATP})\big) - C_2 \tag{2.24}$$

Due to large variability observed within the samples, each set of five condition-specific repeats were further subjected to a Grubbs' test. Extreme outliers are highlighted upon calculation of a repeat-specific Z value, where $\overline{x}$ is the sample mean and σ the standard deviation;

$$Z_i = \frac{|\overline{x} - x_i|}{\sigma} \tag{2.25}$$

A value is considered an outlier if Z_i is greater than a critical value, Z_c. This is determined by the size of the sample, i.e. for $n = 5$, $Z_c = 1.71$ at a significance level of p = 0.05. Outliers were removed from further analysis.

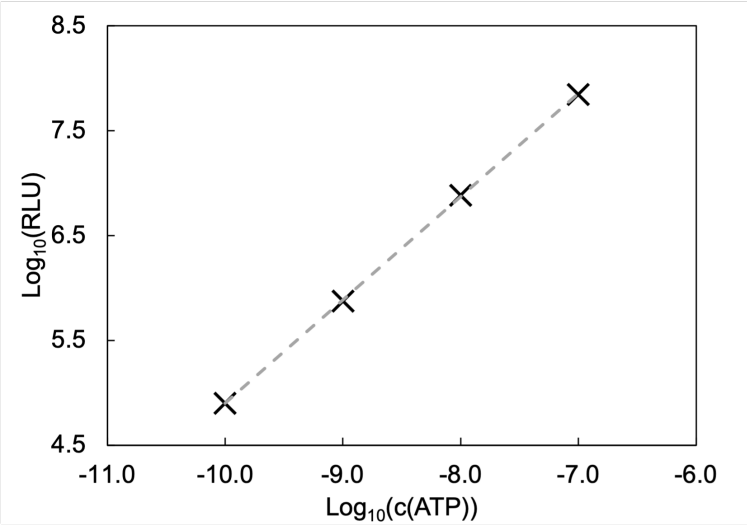

Figure 2.11: ***Calibration of rL/L reagent.*** *The conversion of RLU values into ATP concentration was achieved through calibration of each aliquot of rL/L reagent using four ATP standards of concentration 10^{-7} to 10^{-10} M. The relationship between RLU and c(ATP) was of a linear style on a log - log scale. For the calibration presented here,* $\log_{10}(RLU) = 0.99 \log_{10}(c(ATP)) + 14.75$.

3 Mesoscale structure in monolayers akin to the RBC membrane

3.1 Introduction

The plasma membrane of a cell acts as the main barrier between the intra- and extracellular spaces. Whilst much is know about the individual constituents that make up the plasma membrane including lipid and protein species, little is understood about the considerably complex molecular organisation of such systems [64]. The plasma membrane can be simplified into model lipid bilayers, or further into Langmuir lipid monolayers that are akin to either leaflet of the bilayer. Both are ideal candidates for surface sensitive scattering techniques, such as x-ray crystallography which reveals information about the lateral and transverse molecular organisation of the constituent lipids. In turn, this provides the foundation for gaining a greater understanding of the organisation of lipids within the plasma membrane.

3.1.1 Lipid monolayers akin to the RBC membrane

The cytoplasmic inner leaflet and the exoplasmic outer leaflet of the RBC plasma membrane each provide a unique monolayer on which to examine structural order. This results from the asymmetrical distribution of the four dominant phospholipid species within the RBC plasma membrane, as illustrated in Figure 3.1. The dominant lipid in the inner leaflet is phosphatidylethanolamine (PE), with the remaining three species all present in smaller quantities. On the contrary, the outer leaflet contains much more sphingomyelin (SM) and phosphatidylcholine (PC), whilst notably lacking in phosphatidylserine (PS).

It is thought that this asymmetry may not be due to chance, but instead serves a purpose in the physiological functioning of membrane proteins and other cellular processes hosted in, or mediated by, the plasma membrane. For example, an increase of PS in the outer leaflet of the membrane has been associated with the labelling of

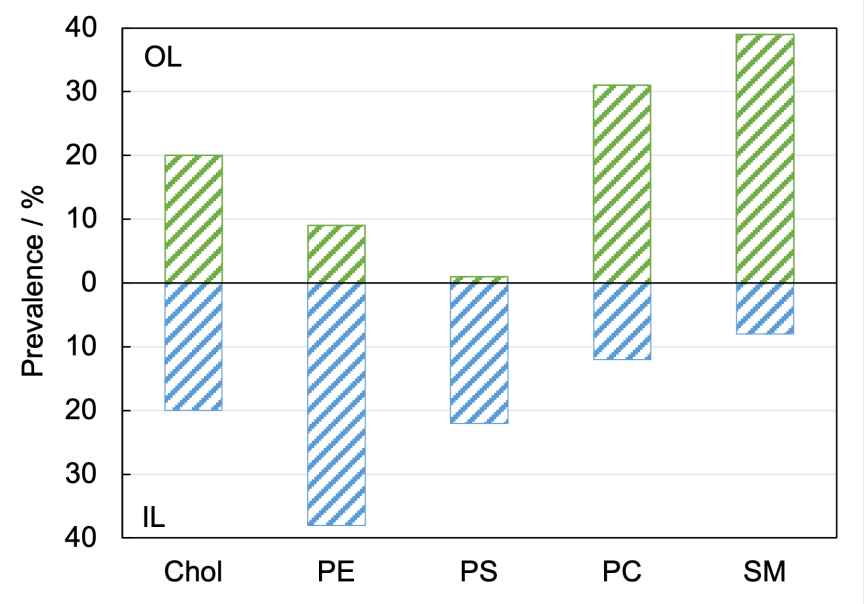

Figure 3.1: ***Asymmetry of lipid species within the plasma membrane.*** *The percentage distribution of lipid species within the inner (IL) and outer (OL) leaflets of the human RBC plasma membrane, adapted from [5].* *Abbreviations: Chol, cholesterol; PE, phosphatidylethanolamine; PS, phosphatidylserine; PC, phosphatidylcholine; SM, sphingomyelin.*

cells to signal removal from the blood circulation [65]. Further, sphingolipids have been implicated in the formation of lipid rafts [7], microdomains of highly ordered and dense lipid packing, due to their high affinity for cholesterol [66]. At first a controversial hypothesis, due to the experimental inability to prove their existence, the importance of lipid rafts is still widely contested. However, it is now thought that rafts provide specialised micro-environments to aid in protein function, as is the case in certain cell signalling pathways [66]. The existence of lipid rafts within a membrane implies the coexistence of domains of differing fluidity and degree of order.

The arrangement of phospholipids within a monolayer will, at the fundamental level, depend on the structure of each individual lipid. As described in detail in Section 1.1.1, lipids can either be cylindrical or conical in shape depending on the relative size of their headgroup to the acyl chain structure or quantity. This ratio is summarised by the critical packing parameter, $cpp = {}^{V}/_{AL}$, where V is the hydrophobic volume, L the acyl chain length and A the area of the hydrophilic region. Figure 3.2 demonstrates the chemical structures for the four main RBC plasma membrane lipids (PE, PC, PS and SM), where dipalmitoyl (DP, C_{16} saturated) lengths are shown as the fatty acid moieties. The headgroup indexing a PE lipid is comparatively smaller suggesting that these lipids have a more conical shape ($cpp \geq 1$ [67]), whereas the other lipid species are more cylindrical ($1/2 < cpp < 1$ [67]) [68] . The bilayer structure within a plasma

membrane is unfavourable for cone shaped lipids. It is therefore unsurprising to see a large fraction of stabilising lipids such as PS, which naturally prefer the bilayer arrangement, alongside the large amount of PE in the inner leaflet (Figure 3.1).

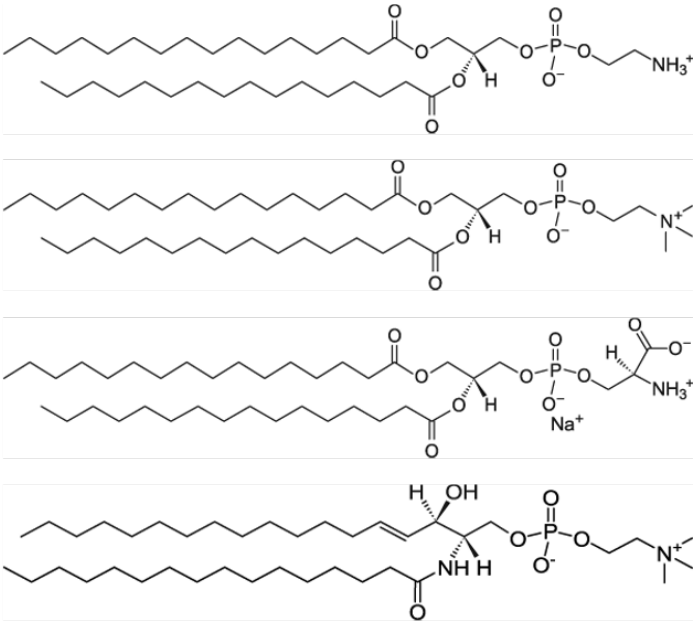

Figure 3.2: ***Chemical structures of phospholipid molecules.*** *From top to bottom: PE, PC, PS, and SM [69] represent lipids typically found in the RBC plasma membrane. All are shown with 16-carbon acyl chains, demonstrating dipalmitoyl (DP) molecules.*

3.1.2 Obtaining structural information from Langmuir monolayers

The molecular arrangement of a monolayer is studied using surface sensitive x-ray techniques, possible as the dimensions within a monolayer are on a similar order of magnitude to the x-ray wavelength (nanometre-scale). Since the successful introduction of the application of x-ray radiation in this manner, many biological and physical systems have been studied at the air-subphase interface, from simple monomolecular systems to more complex systems that focus on processes such as protein adsorption. Importantly, synchrotron sources dedicated to the production of the intense radiation required, have become more widely available for use. Depending on the technique employed x-ray scattering can probe the lateral order of a monolayer or the transverse structure. Together both methods enable a complementary study of monolayers, giving rise to a comprehensive picture of the supramolecular arrangement of the lipids within the monolayer.

Lateral order

Grazing incidence x-ray diffraction (GIXD) is sensitive to monolayer lateral structure. In this technique, x-rays are incident on the sample at a grazing angle that ensures total reflection. Any periodicity in the form of lateral crystalline supramolecular organisation located within the monolayer results in a diffraction peak. This technique has been outlined in detail in Section 2.1.2.

Previous work has suggested that at higher surface pressures (45 mN/m), monolayers of the DPPE phospholipid give rise to a single diffraction peak with a d-spacing of 4.16 ± 0.01 Å [70]. A diffraction pattern such as this is indicative of hexagonal packing symmetry, defined by the unit cell parameters $|\mathbf{a}| = |\mathbf{b}|$ and $\gamma = 120°$. Interestingly, the study of Helm *et al.* [71] measured the GIXD pattern of a DMPE (dimyristoyl, DM, chains are C_{14} in length) monolayer at several intervals of increasing surface pressure. Their results demonstrated that increasing surface pressure results in a GIXD pattern that has a smaller FWHM but greater intensity, suggesting greater lateral ordering of the PE monolayer. Miller *et al.* [72, 73] also detailed the increasing degeneracy of the DPPE diffraction peak with increasing surface pressure. These results demonstrate that an increase in peak FWHM at lower surface pressures could be indicative of a breakdown in the peak degeneracy and therefore, a change in lattice packing. At the lower surface pressure of 20 mN/m where multiple peaks were observed for the DPPE monolayer, d-spacings of 4.394, 4.304 and 4.217 Å have been reported [73].

In contrast to the high lateral ordering of phospholipids with a PE headgroup, PC lipid monolayers give rise to two distinct Bragg peaks indicative of a distorted hexagonal packing arrangement ($|\mathbf{a}| = |\mathbf{b}|$ and $\gamma < 120°$) [73, 74]. In these studies, the peak at smaller q_{xy} was the degenerate {(1,0),(0,1)} peak, whilst the peak at larger q_{xy} was the {1,-1} peak. At the lower pressure of 20 mN/m, the position of these peaks corresponded to d-spacings of ∼4.79 and ∼4.33 Å, respectively [73, 74]. As the lateral pressure applied to the PC system was increased to 30 mN/m, the d-spacings were reduced to 4.606 and 4.291 ± 0.0005 Å, respectively [75]. PC monolayers exhibit a greater area per molecule than PE monolayers [73], as evident from the larger d-spacings and likely a result of the larger size of the PC headgroup.

The lateral packing of the acyl chains in a DPPS monolayer is further distorted from the ideal hexagonal packing of the PE lipid. DPPS diffraction patterns have been characterised as three separate diffraction peaks, indicating an oblique unit

cell ($|\mathbf{a}| \neq |\mathbf{b}|$ and $\gamma < 120°$) [74]. Not only is the degeneracy of the diffraction peaks completely broken, but their positions are also at larger q_{xy} than for DPPC monolayers, corresponding to smaller d-spacings of 4.447, 4.563 and 4.268 $\pm$ 0.001 Å, respectively [74]. Additionally, the area per molecule of a DPPS monolayer falls between that of PE and PC.

The final lipid with a significant contribution to the RBC plasma membrane is SM. GIXD patterns of an SM monolayer differ greatly from the three previously described monolayers. They are characterised by a broad low intensity peak even at higher surface pressures, suggesting an amorphous packing arrangement [76]. Previous results suggest the d-spacing of this peak ranges from 4.260 to 4.298 Å as surface pressure is varied between 18.5 and 35 mN/m [75, 76]. The area per molecule of an SM monolayer is comparative to, if not slightly greater than, that of a DPPC monolayer.

The overwhelming majority of literature focuses on monolayers comprised of each phospholipid species individually rather than a mixture which is more similar to the RBC plasma membrane, with many different lipid headgroups and acyl chain structures. However, in previous work where DPPS was added to a monolayer of DPPC at a ratio of 10:90 mol-%, the results demonstrated that the diffraction pattern of the GIXD measurement took a form similar to that of the dominant lipid species but with overall less intensity [74]. This reduced peak intensity of the measurement suggested that the mixing of various lipids disrupted the lateral order within the monolayer.

Transverse structure

Transverse structure, in the form of electron density and monolayer thickness, is measured using either grazing incidence x-ray off-specular scattering (GIXOS) or x-ray reflectivity (XRR). The differences between these two measurement techniques have been previously discussed in detail in Chapter 2. In summary, the main difference is that XRR is a direct measurement of the monolayer reflectivity, whilst GIXOS results in a pseudo-reflectivity that can be analysed using the exact same protocol as for the reflectivity curves. Since XRR is the older of the two techniques, much of the data available relating to transverse structure has been established using this method. As electron density curves are often hard to compare between systems due to the variety of scales they can be presented on, it is often easier to compare monolayer slab thickness as calculated from fitting the reflectivity curve (see Section 2.1.2).

Helm *et al.* [71] found that the acyl chain region thickness for a DMPE monolayer (PE headgroup with 14-carbon length acyl chains) was in the region of 16.6 Å. Naturally, this suggests the 16-carbon chains of DPPE would lead to a thicker slab. This result is supported by the work of Majewski *et al.* [70]. At a surface pressure of 45 mN/m, they reported slab thicknesses of 8.2 ± 0.2 and 18.8 ± 0.1 Å for the respective headgroup and acyl chain regions of a DPPE monolayer on a water subphase.

The PC phospholipid is known to have a much larger headgroup than PE, so a thicker headgroup region would be expected for a DPPC monolayer. Indeed this value is reported between 8.4 ± 0.3 and 9.08 Å at surface pressures of 35 and 30 mN/m respectively [75, 77], unsurprisingly larger than that reported for the DPPE monolayer. Both of these studies also reported the acyl chain slab thickness to be ∼ 15.5 Å.

In order of increasing headgroup slab thickness, the work of Tae *et al.* [77] indicated a thickness of 11.6 ± 0.3 Å for a DPPS monolayer. In contrast, the thickness for the acyl chain slab reported in their study fell between that of a DPPE and DPPC monolayer at 16.6 ± 0.3 Å. The variation in acyl chain slab thicknesses reported for the various DP phospholipid monolayers could result from variations in chain tilt, as measured from the interface normal. A smaller thickness would indicate a greater degree of tilting.

Reported monolayer thickness values for the SM phospholipid species vary within the literature, however this is most likely a result of each study using a SM lipid that differed in acyl chain length. Reported values of the headgroup slab thickness are in close agreement, at approximately 11 Å [75, 76]. However, discrepancies in the acyl chain region suggest the thickness is between 15 - 19 Å, although this is further dependent upon what pressure the system was investigated at.

It follows from the lateral order investigations that these systems have all been investigated individually. Therefore, major questions remain as to what effect mixing of the various lipid species will have on the electron density and monolayer thickness.

3.1.3 Dimethyl sulphoxide and the RBC

The dimethyl sulphoxide (DMSO) structure is such that two hydrophobic methyl groups are bonded to a central hydrophilic sulphoxide group. This gives rise to an amphiphilic molecule that can interact with the RBC plasma membrane in multiple

ways. It serves to investigate the effect of this molecule on the organisation of Langmuir monolayers, as a means to provide justification for its myriad of uses within the biological and pharmacological fields, described below.

First and foremost, DMSO has been found useful as a solvent [78] and penetration enhancer. In the latter case, DMSO aids the permeation of antiviral agents, antibiotics and steroids through the skin and is generally used in relatively high concentrations (>60%), which can induce negative side effects, such as erythema [79]. The effects of DMSO treatment are also exploited in cellular differentiation, demonstrated to be optimal at DMSO concentrations of 2 vol-% [80], and cell fusion at concentrations ranging from 5 vol-% [81] to around 35% [82]. It is not known whether DMSO is directly involved in these processes, or simply acts in such a way that aids other protagonists. Further, DMSO has demonstrated protective properties. As a radioprotector, Bishayee *et al.* demonstrated that DMSO is most effective at a concentration of 10 vol-% [83]. Of significant importance is the use of DMSO as a cryoprotectant, especially in the case of umbilical cord blood where concentrations of 10 vol-% are cited as the norm [84].

Despite its extensive use, a comprehensive experimental evaluation of the explicit effects of DMSO on the phospholipid membrane remains evasive and left often to molecular dynamics simulations. Performed using single lipid species and cholesterol containing bilayers, the simulations are in agreement that a 3-fold response to increasing DMSO concentration exists [85–88]. In the first regime, low concentrations of DMSO (up to $\sim$ 10 mol-%) induce disordering, loosening, thinning and increased hydrophobic core fluidity of a lipid bilayer. Increasing the concentration of DMSO (often bilayer composition dependent) initiates pore formation, with larger concentrations of DMSO inducing increasingly more stable pores. In the final regime, where DMSO concentration becomes excessive ($\geq$ 40 mol-%), total disintegration of the bilayer is observed. This behaviour indicates that interaction of the RBC membrane with DMSO causes significant modifications to the structure of the membrane, not least the lipid bilayer. As such, structure analysis tools such as GIXD and GIXOS will prove useful in expanding the theoretical knowledge gained from simulations on of the molecular level effects of DMSO on the membrane structure and integrity, experimentally.

3.1.4 Chapter outline

Presented here is an investigation of the mesoscale structure in monolayers that are akin to each leaflet of the lipid bilayer of RBC membranes. The two monolayer systems, inner leaflet and outer leaflet (IL and OL) were spread on a water subphase and investigated using GIXD, GIXOS and XRR. The former technique probes the lateral ordering and crystalline structure of monolayers, whilst the latter two techniques probe the transverse electron density and thickness of the monolayer. Inclusion of both the GIXOS and XRR techniques for the same monolayers allowed for comparison of results and therefore, proof of concept. Together, all three methods provide a coherent picture of the structure of each monolayer system.

As an extension to this work the addition of 10 vol-% DMSO to the subphase was also investigated through GIXD and GIXOS measurements. This concentration replicates that used in the cryopreservation of cord blood and further, the addition of DMSO to the subphase allowed for observation of the structural effects of DMSO on the monolayer. This method was chosen over a pre-incubation of DMSO with the phospholipid solutions, as the latter method would have mainly detailed the effect of DMSO directly on the lipid molecules but not necessarily their arrangement within the monolayer. It is hoped that these results will elucidate the effect of DMSO on the red cell membrane and provide justification for the solvent's many uses in biological and pharmacological fields.

3.2 Experimental methods

The theory, methodology, and data analysis of GIXD, GIXOS, and XRR have been outlined in detail in Section 2.1.2. The section here serves to present specifics regarding the samples investigated and their preparation, along with the beamline specifications.

3.2.1 Sample preparation

For all measurements monolayers were kept at a surface pressure of 30 mN/m, temperature of 293.15 K (bath and thermostat used to temper the subphase), and in a helium rich atmosphere for the duration of the experiment. Furthermore, lateral shifting of the beam spot between measurements was incorporated to aid in minimising

radiation damage to the monolayers. The subphase was kept simple, being either ultra-pure water (UPW) or 10-vol% DMSO (>98%; Sigma-Aldrich, USA) diluted in UPW .

Phospholipid mixtures were chosen to mimic both leaflets of the RBC membrane lipid bilayer, with stock samples of each prepared as a chloroform solution at a total concentration of 1 g/L. The molar composition of the inner leaflet (IL) mixture was as follows: DPPC : DPPE : DPPS : CHOL : SM[1] = 12 : 38 : 22 : 20 : 8 mol-%, where as the outer leaflet (OL) contained: DPPC : DPPE : DPPS : CHOL : SM = 31 : 9 : 1 : 20 : 39 mol-% (Avanti Polar Lipids Inc., USA).

It is of note that these experiments were performed using phospholipids with saturated chains, whilst unsaturated lipid chains are predominant in the native RBC plasma membrane. The double bonds within the chains of unsaturated lipids create 'kinks' which result in an increased area per lipid and reduced packing density. As such, signal attenuation is observed in x-ray studies of unsaturated lipids in comparison to studies of saturated lipids [89]. Since the aim of the study presented here was to observe the distinct packing arrangement of the various lipid species within a monolayer, lipids with saturated chains have been used to obtain a more desirable signal in the x-ray experiments. Further, due to the complexity of the monolayers investigated the saturated acyl chains allowed for better comparison of results to the literature, where saturated acyl chains are frequently used, and hence, more definitive conclusions could be drawn.

3.2.2 Beamline specifications

The GIXD and GIXOS data presented in this thesis were obtained at the PETRA III beamline P08 of the Deutsches Elektronen-Synchrotron (DESY), Hamburg, Germany. The Langmuir trough, with maximum area 182 cm^2, consisted of two movable barriers, a filter paper surface pressure sensor and a glass block positioned in the subphase under the illuminated area (to reduce mechanically excited surface waves [90]). The monolayer was illuminated at an incident angle of 0.07° (85% of the critical angle of water), with monochromated x-ray radiation at 15 keV (λ = 0.827 Å, 100.24 mA) with a high photon flux of 10^{12} photons per second. The area of sample illuminated by the beam was method dependent: for the GIXD geometry the beam illuminated a

[1] DPPC (1,2-dipalmitoyl-sn-3-phosphocholine), DPPE (1,2-dipalmitoyl-sn-glycero-3-phosphoethanolamine), DPPS (1,2-dipalmitoyl-sn-glycero-3-phospho-L-serine, sodium salt), (d18:1/16:0) SM (N-palmitoyl-d-erythro-sphingosylphosphorylcholine), CHOL (cholesterol)

rectangle of 0.07 x 1 (vertical × horizontal) mm, but the GIXOS geometry was a line illumination of 250 μm. A Mythen 1k linear detector recorded the diffracted beam in the GIXD experiments, whilst a Pilatus 100k area detector recorded the GIXOS signal.

XRR measurements were made at the TORIKA II beamline ID10b of the European Synchrotron Radiation Facility (ESRF), Grenoble, France. The Langmuir trough had a maximal area of 711 cm^2, with a single movable barrier and filter paper surface pressure sensor. With a photon flux of 10^{12} photons per second the sample was illuminated with monochromatic x-ray radiation at 8keV (λ = 1.55 Å, 200 mA) over an area of 10 x 300 μm. The specularly reflected beam was detected by a Cyberstar scintillation counter.

3.3 Results

This section presents the results of the structural analyses of Langmuir monolayers akin to both the inner and outer leaflets of the RBC lipid bilayer, on both UPW and aqueous-DMSO subphases. For ease of comparison between monolayer systems, a summary of the quantitative results obtained from the GIXD measurements are presented in Table 3.1. Further, monolayer thicknesses obtained from both GIXOS and XRR measurements are summarised in Table 3.2.

For clarity the IL monolayer is always depicted by blue circles (◯) and the OL monolayer is always depicted by green triangles (△) when presented in graphical format. Further, the results obtained on the UPW subphase are a lighter shade than those obtained on the aqueous-DMSO subphase. Systems are identified as the monolayer followed by the subphase. For example, the inner leaflet on the UPW subphase will subsequently be referred to as IL_water, and be presented as light blue circles within graphs.

3.3.1 Grazing incidence x-ray diffraction

Reciprocal space 2-D heatmaps obtained from GIXD measurements of both the IL_water and OL_water monolayers are presented in Figure 3.3. The corresponding 1-D Bragg peaks are shown in Figure 3.4 (symbols). The experimental data were fit with a superposition (solid line) of two Lorentzian curves (dashed lines). Whilst the

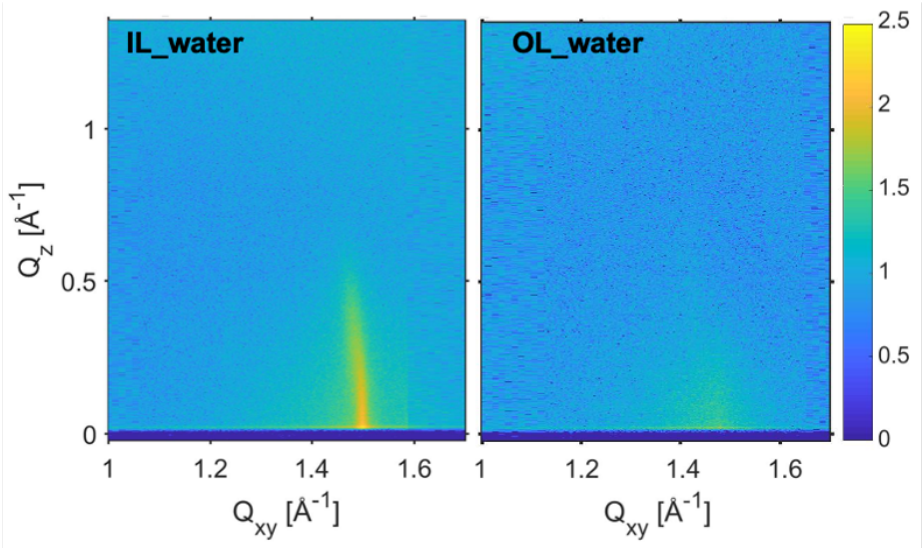

Figure 3.3: ***GIXD 2-D heatmaps.*** *The reciprocal space heatmaps obtained from GIXD measurements of the IL (left) and OL (right) monolayers, each on the UPW subphase.*

Lorentzian is not the ideal peak shape, it is the most frequent practice when fitting Bragg peak data.

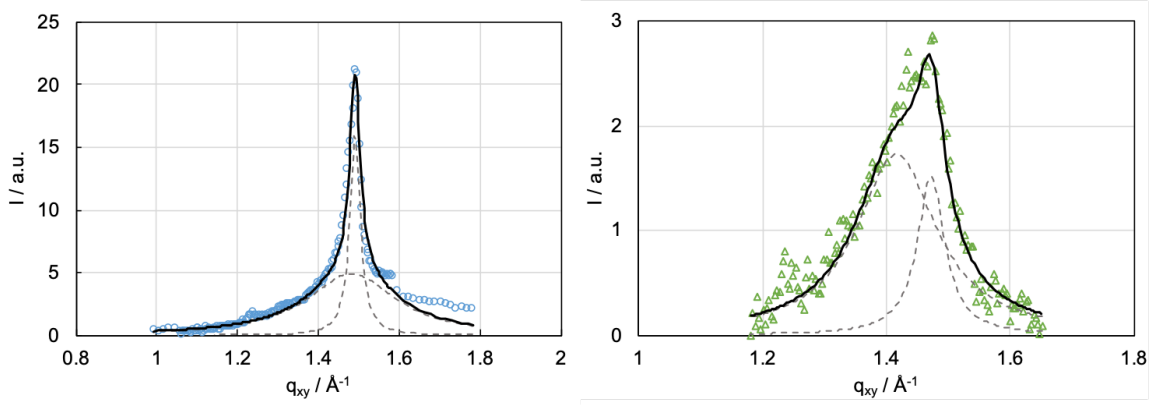

Figure 3.4: ***1-D Bragg peaks measured for the IL_water and OL_water monolayers.*** *The experimental data (IL - ◯ left, OL - △ right) were fitted using the sum (—) of two Lorentzian curves (- - -). Note the order of magnitude difference in y-axis scaling.*

The apparent single peak for the IL_water system appears to be centred at an approximate q_{xy} value of 1.4898 Å^{-1}, although it was observed that more accurate information could be obtained when the data were fit with a superposition of two Lorentz peaks. The enhanced trend of the double Lorentz curve, with respect to the data, suggests that the degeneracy of the single peak reflection may have been somewhat lifted. For further analyses the two peaks were indexed with the corresponding Miller Indices. The lower intensity peak centred at $q_{xy} = 1.483 \pm 0.003$ Å^{-1} and with a FWHM of 0.26 ± 0.01 Å^{-1} corresponded to the degenerate {(0,1), (1,0)}

reflection. These values transposed to $d = 4.237 \pm 0.01$ Å and $L_c = 21 \pm 1$Å in the {(0,1), (1,0)} crystallographic direction. The more intense peak centred at [2]$q_{xy} = 1.491$ Å^{-1} and with a [2]FWHM of 0.03 Å^{-1} corresponded to the {1,-1} reflection. In this crystallographic direction, [2]$d = 4.21$ Å and $L_c = 180 \pm 7$ Å.

The lifting of the degeneracy in the two peak fit suggested a packing arrangement of the phospholipid acyl chains with distorted hexagonal lattice symmetry. A lattice of this geometry is fully described by a unit cell with characteristics $|\mathbf{a}| = |\mathbf{b}|$ and $\gamma < 120°$. Solving Equation 2.3 for each of the indexed peaks suggests $|\mathbf{a}| = |\mathbf{b}| = 4.88 \pm 0.02$ Å, [2]$\gamma = 119.64°$ and the unit cell area, $A = 20.7 \pm 0.2$ Å^2.

Of note for the IL_water data, is the divergence of the fit from the experimental data at $q_{xy} \gtrsim 1.55$ Å. This is most likely an artefact of the experimental design, where a change in q_{xy} step occurred around this value. To prevent the q_{xy} step change impacting any further measurements in such a manner, it was shifted to a higher q_{xy} in measurements of the remaining systems.

Analysis for the OL_water system was much less complicated, as the lifting of the peak degeneracy was much more pronounced. The {(0,1), (1,0)} peak, centred at 1.417 ± 0.005 Å^{-1}, had a FWHM of 0.16 ± 0.01 Å^{-1}. In this crystallographic direction, $d = 4.44 \pm 0.02$ Å and $L_c = 36 \pm 1$ Å. The parameters for the {1,-1} peak were as follows: $q_{xy} = 1.473 \pm 0.002$ Å^{-1}, FWHM $= 0.05 \pm 0.01$ Å^{-1}, [2]$d = 4.27$ Å, and $L_c = 105 \pm 15$ Å. In turn, the distorted hexagonal packing arrangement was fully described by a unit cell with the parameters $|\mathbf{a}| = |\mathbf{b}| = 4.99 \pm 0.01$ Å and $\gamma = 117.37 \pm 0.01°$, where $A = 22.2 \pm 0.1$ Å^2.

3.3.2 Grazing incidence x-ray off-specular scattering

The GIXOS measurements and the corresponding pseudo-reflectivity curves for all systems are presented in Figure 3.5. Using the slab model to fit the pseudo-reflectivity curves, slab thicknesses for each of the headgroup and acyl chain regions were obtained and are presented in Figure 3.6. Whilst the overall shape of the GIXOS and pseudo-reflectivity curves appear similar for the two monolayers on the UPW subphase (aqueous-DMSO subphase discussed later, in Section 3.3.4), there are subtle differences in the q_z values of the inflexion points alluding to dissimilar monolayer slab thicknesses.

[2]Negligible experimental uncertainty.

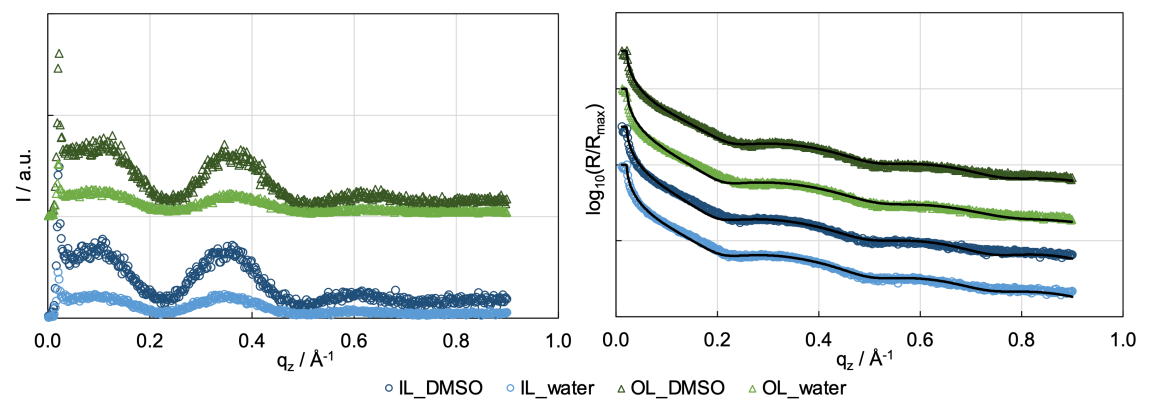

Figure 3.5: ***GIXOS and pseudo-reflectivity curves for all systems.*** *For clarity, the GIXOS data (left) for the OL systems (△) are presented offset from the IL systems (◯). The corresponding pseudo-reflectivity curves (right, symbols) are also presented in a stacked approach. Here, the solid line represents the parameterised fit using the slab model.*

Figure 3.6 revealed the headgroup region for the OL_water system as significantly smaller than that for the IL_water system, at 7.5 ± 0.7 and 8.5 ± 0.2 Å, respectively. The experimental uncertainty in the measured values of the slabs representing the acyl chain region of each monolayer suggested no significant difference in thickness. These thicknesses were 16.7 ± 0.5 and 17.1 ± 0.2 Å for the OL and IL systems respectively.

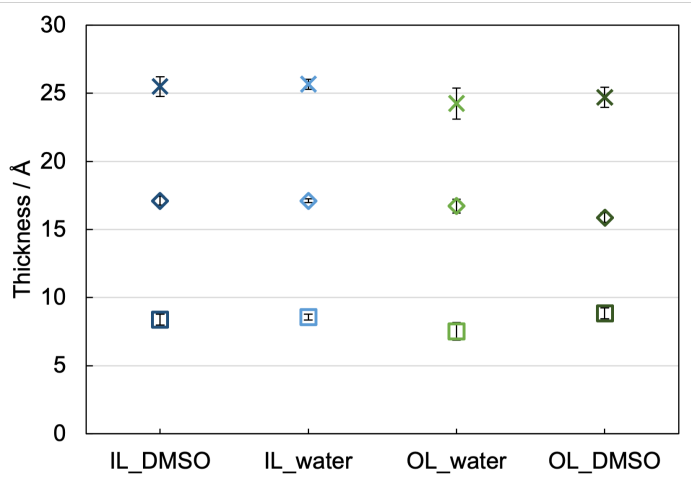

Figure 3.6: ***GIXOS slab thickness.*** *The overall monolayer thickness (×) is presented alongside the size of the acyl chain (◊) and headgroup (□) slabs. Measured perpendicular to the water surface for the two monolayers (IL and OL) on both subphases (UPW and 10 vol-% aqueous-DMSO).*

Electron density, ρ_e, profiles were calculated from the fit of the pseudo-reflectivity curves. Again focusing first on the systems with the UPW subphase, the electron

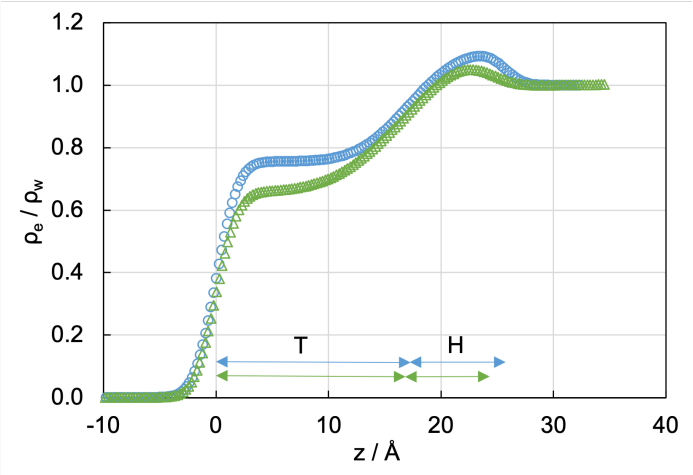

Figure 3.7: ***Electron density profiles of the IL_water and OL_water monolayers.*** *The electron density profiles obtained from GIXOS measurements of the IL (◯) and OL (△) monolayers on a UPW subphase. ρ_w represents the electron density of the subphase and arrows demonstrate the approximate overall slab thickness, with the acyl chain slab* (T) *from $z = 0$ Å, followed by the headgroup slab* (H).

density profiles for IL_water and OL_water are presented in Figure 3.7. A smaller overall ρ_e was measured for the OL_water system across all slabs, with the difference being noticeably more pronounced in a comparison of the acyl chain region.

3.3.3 X-ray reflectivity

The transverse structure of the IL_water and OL_water systems were also investigated using the classical XRR technique. The inclusion of these results served to act as a proof of concept comparison for both the standard XRR and advanced GIXOS techniques. Since the same UPW subphase was used for both methods, for this section the systems are referred to as the monolayer type followed by the experimental method (i.e. IL_XRR). Reflectivity curves (symbols), the parameterised fit (solid lines) and resulting ρ_e profiles from the XRR measurements are given in Figure 3.8. The slab thicknesses output from the reflectivity fit are further presented in Figure 3.9, alongside the corresponding values from the GIXOS measurements (as already shown in Figure 3.6).

There are noticeable differences between the reflectivity curves of the IL_XRR and OL_XRR systems. The local minima of the IL_XRR curve are much more pronounced and appear at lower q_z, implying differences in monolayer thickness which was exemplified in the ρ_e profiles. Here, the acyl chain region of the IL_XRR system

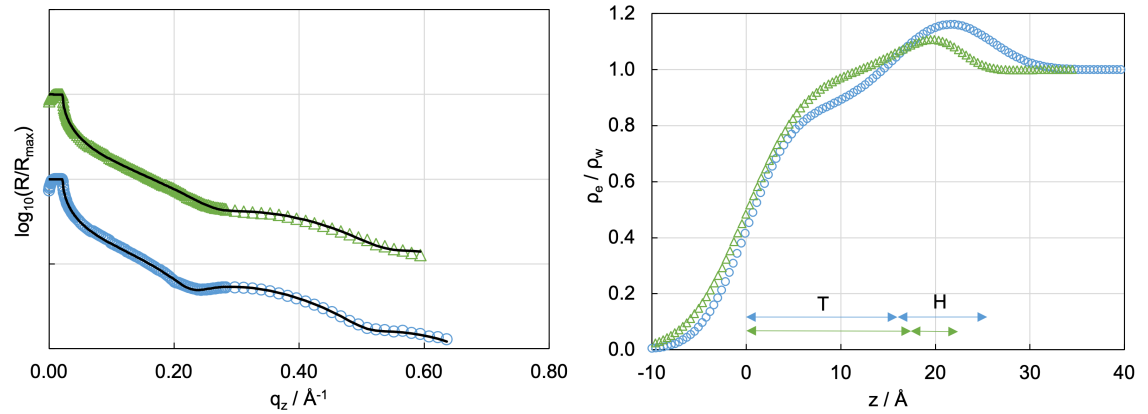

Figure 3.8: ***XRR reflectivity curves and electron density profiles.*** *The XRR reflectivity curves (left) for the IL_XRR (◯) and OL_XRR systems (△). The curves were then converted into electron density profiles and normalised to the electron density of the subphase, ρ_w (right). Arrows demonstrate the approximate overall slab thickness, with the acyl chain slab (T) from $z = 0$ Å, followed by the headgroup slab (H).*

had a lower electron density than the acyl chain region of the OL_XRR system, but this dissimilarity is reversed for the ρ_e of the headgroup regions. Of particular note the ρ_e profiles presented in Figure 3.8 (right) differ from those obtained using the GIXOS technique (Figure 3.7), particularly in the acyl chain region.

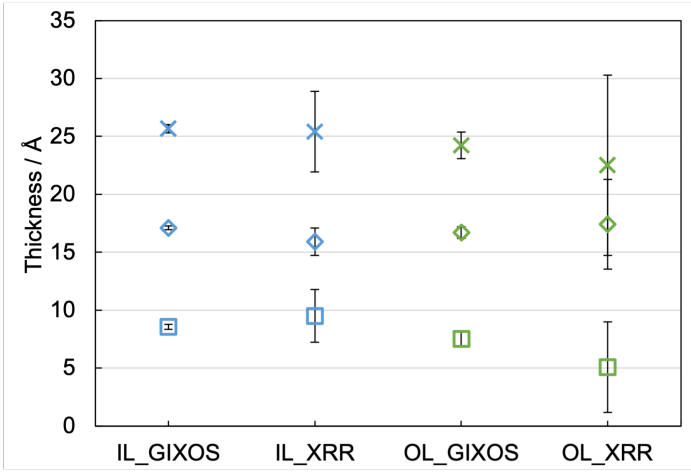

Figure 3.9: ***Comparison of slab thickness between GIXOS and XRR.*** *The overall monolayer thickness (×) is presented alongside the size of the acyl chain (◊) and headgroup (□) slabs. Measured using both GIXOS and XRR for the two monolayers (IL and OL) on a UPW subphase.*

A comparison of slab thickness between the XRR systems reveals that whilst there are differences in the measured values, large experimental uncertainties suggest these are not significant. The overall thickness of the IL monolayer was 25 ± 3 Å, whereas the OL monolayer measured 23 ± 8 Å. Individual slab thicknesses for the IL monolayer

were found to be 16 ± 1 Å for the acyl chain region and 10 ± 2 Å for the headgroup region. Again, no significant differences were found between these data and the thickness of the corresponding slabs of the OL monolayer. For the OL monolayer, the acyl chain region was measured at 17 ± 4 Å and the headgroup region at 5 ± 4 Å. Further, Figure 3.9 demonstrates that these results are similar to that obtained using the GIXOS technique when the experimental uncertainties are accounted for.

3.3.4 Aqueous-DMSO subphase

As an additional set of experiments, the UPW subphase was exchanged with an aqueous-DMSO subphase at a concentration of 10 vol-%. GIXD and GIXOS measurements were performed on both the IL and OL monolayers on this subphase.

Grazing incidence x-ray diffraction

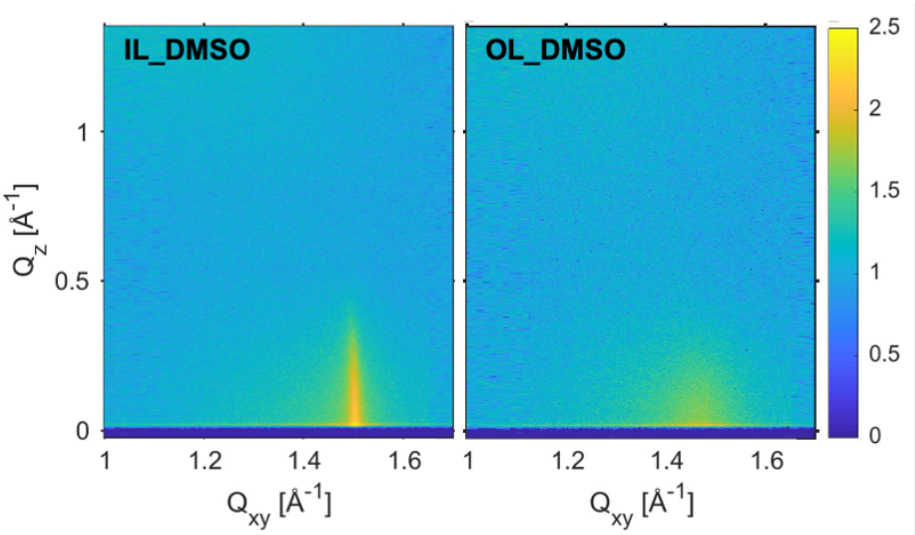

Figure 3.10: ***2-D GIXD heatmaps, aqueous-DMSO subphase.*** *The reciprocal space heatmaps obtained from GIXD measurements of the IL_DMSO (left) and OL_DMSO (right) monolayers.*

GIXD measurements of the IL and OL monolayers on an aqueous-DMSO subphase are presented in heatmap format (Figure 3.10), with the corresponding 1-D Bragg peaks presented in Figure 3.11. As with the monolayers on the UPW subphase, these peaks were fit with a superposition of two Lorentz curves.

The aqueous-DMSO subphase appeared to definitively lift the peak degeneracy for the IL monolayer, with GIXD data showing two Bragg peaks. The centre of the less

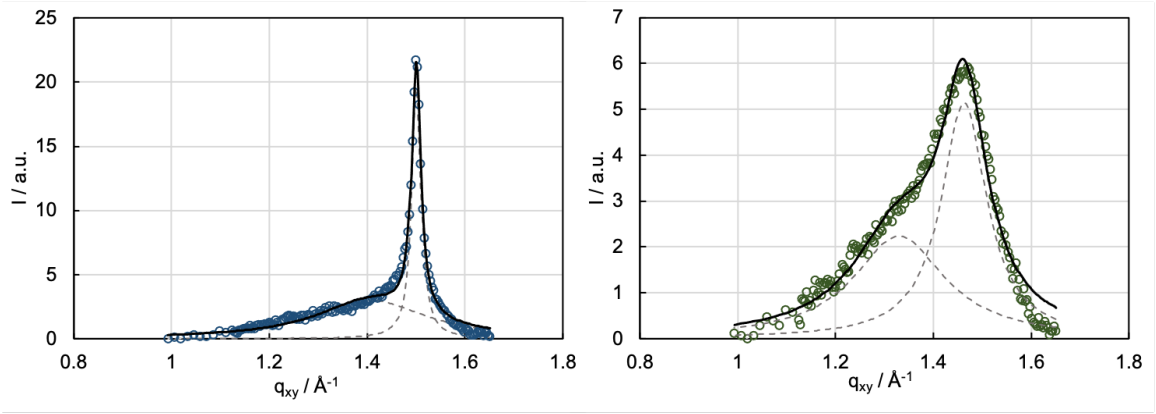

Figure 3.11: ***1-D Bragg peaks measured on the IL_DMSO and OL_DMSO monolayers.*** *The experimental data (IL - ◯ left, OL - △ right) were fitted using the sum (—) of two Lorentzian curves (- - -). Note the different y-axis scaling between the two monolayers.*

intense peak shifted to $q_{xy} = 1.408 \pm 0.004$ Å^{-1} and the FWHM of this peak was 0.27 $\pm$ 0.01 Å^{-1}, giving a d-spacing of 4.46 $\pm$ 0.01 Å and coherence length $L_c = 20.7 \pm$ 0.8Å in the {(0,1), (1,0)} crystallographic direction. The second peak was centred at [3]$q_{xy} = 1.500$ Å^{-1} with a [3]FWHM of 0.02 Å^{-1}. These values correspond to [3]$d = 4.19$ Å and $L_c = 250 \pm 5$ Å in the {1,-1} crystallographic direction. As with the UPW subphase, the multiple Bragg peaks suggest that the acyl chains of the phospholipid molecules were arranged with distorted hexagonal symmetry. It followed that the lattice parameters were $|\,\mathbf{a}\,| = |\,\mathbf{b}\,| = 4.95 \pm 0.02$ Å with [3]$\gamma = 115.59°$, and the unit cell area, $A = 22.1 \pm 0.2$ Å^2.

The aqueous-DMSO subphase increased the overall intensity of the Bragg peak obtained from the OL monolayer when compared to that from the OL_water system. For the OL_DMSO system, the first peak was centred at $q_{xy} = 1.330 \pm 0.008$ Å^{-1} with a FWHM of 0.23 $\pm$ 0.02 Å^{-1}. From these values the d-spacing and coherence lengths were calculated as $d = 4.73 \pm 0.03$ Å and $L_c = 25 \pm 2$ Å in the {(0,1), (1,0)} crystallographic direction. The second peak was centred at $q_{xy} = 1.463 \pm 0.001$ Å^{-1} with a FWHM of 0.11 $\pm$ 0.01 Å^{-1}. The higher q_{xy} decreased the d-spacing, whilst the smaller FWHM increased the coherence length in the {1,-1} crystallographic direction. These values were [3]$d = 4.30$ Å and $L_c = 50 \pm 2$ Å. Again, this behaviour is typical of a distorted hexagonal packing arrangement and led to the following lattice parameters: $|\,\mathbf{a}\,| = |\,\mathbf{b}\,| = 5.14 \pm 0.04$ Å, $\gamma = 113.25 \pm 0.01°$ and $A = 24.3 \pm 0.4$ Å^2.

[3]Negligible experimental uncertainty.

Grazing incidence x-ray off-specular scattering

The GIXOS and pseudo-reflectivity curves for the IL_DMSO and OL_DMSO monolayers are presented alongside the UPW subphase results in Figure 3.5. For ease of comparison, slab thicknesses for these systems are also presented in Figure 3.6. In the case of both monolayers the aqueous-DMSO subphase increased the intensity of the GIXOS measurement, although the resulting pseudo-reflectivity curves appeared not to significantly change from that of the same monolayer on the UPW subphase. In the case of each monolayer on the aqueous-DMSO subphase, the q_z values of the gradient changes in both the GIXOS and pseudo-reflectivity curves followed that on the UPW subphase.

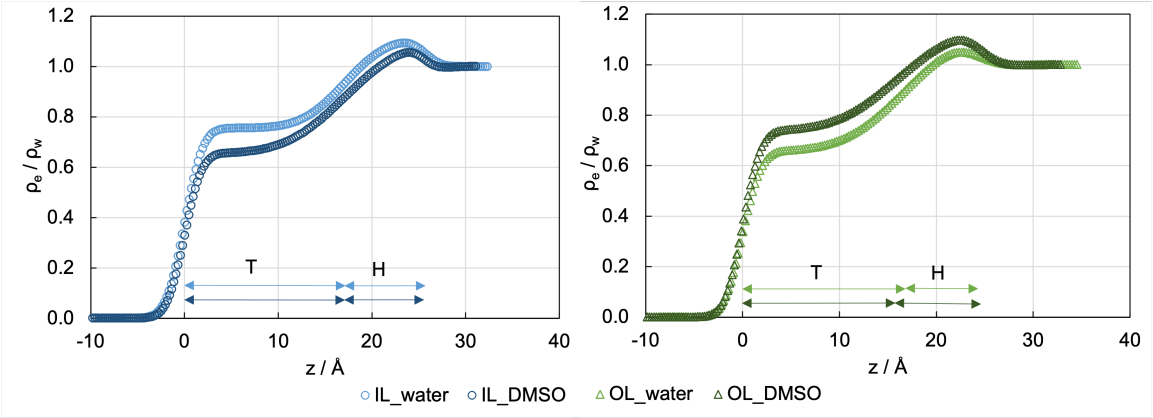

Figure 3.12: ***Comparison of electron density profiles for the IL and OL monolayers on both the UPW and aqueous-DMSO subphases.*** *The aqueous-DMSO subphase reduced ρ_e for the IL monolayer (left), but had the opposite effect on the OL monolayer (right). ρ_w represents the electron density of the subphase and arrows demonstrate the approximate overall slab thickness, with the acyl chain slab (T) from z = 0 Å, followed by the headgroup slab (H).*

As mentioned previously, the subtle differences in the pseudo-reflectivity curves translate into varying thicknesses of the slab regions. When compared to that on the UPW subphase, the aqueous-DMSO subphase had little effect on the individual slab and overall thicknesses of the IL monolayer. For IL_DMSO the thickness values were 8.4 ± 0.4 Å for the headgroup and 17.1 ± 0.3 Å for the acyl chain regions. In contrast, the aqueous-DMSO subphase significantly increased the thickness of the OL monolayer's headgroup region to 8.8 ± 0.4 Å. However, within experimental uncertainty the thickness of the acyl chain region remained unchanged and in turn, the overall thickness of the OL_DMSO monolayer was comparable to that of the OL_water monolayer.

Comparisons of the electron density profiles of the IL_DMSO and OL_DMSO systems to the same monolayer on the UPW subphase are presented in Figure 3.12. Spreading the IL monolayer on the aqueous-DMSO subphase reduced the overall electron density of the monolayer, particularly in the acyl chain region. Interestingly, the aqueous-DMSO subphase had the opposite effect on the OL monolayer, with the largest change again seen in the acyl chain region.

3.3.5 Summary tables

For clarity, GIXD measurements and uncertainties for each of the four systems investigated are presented in Table 3.1. This is followed by a summary of the monolayer thicknesses and uncertainties, obtained from the GIXOS and XRR measurements, in Table 3.2.

Table 3.1: ***GIXD parameters*** *and experimental uncertainties for the four systems investigated at π = 30 mN/m and T = 293.15 K. Each monolayer presented with distorted hexagonal packing symmetry although primitive unit cell parameters varied as outlined below.*
† denotes negligible experimental uncertainty.

	Index	**IL_DMSO**	**IL_water**	**OL_water**	**OL_DMSO**
$\boldsymbol{q_{xy}}$ **(Å^{-1})**	{(1,0),(0,1)}	1.408 ± 0.004	1.483 ± 0.003	1.417 ± 0.005	1.330 ± 0.008
	{1,-1}	1.500 †	1.491 †	1.473 ± 0.002	1.463 ± 0.001
FWHM (Å^{-1})	{(1,0),(0,1)}	0.27 ± 0.01	0.26 ± 0.01	0.16 ± 0.01	0.23 ± 0.02
	{1,-1}	0.02 †	0.03 †	0.05 ± 0.01	0.11 ± 0.01
$\boldsymbol{d}$ **(Å)**	{(1,0),(0,1)}	4.46 ± 0.01	4.237 ± 0.01	4.44 ± 0.02	4.73 ± 0.03
	{1,-1}	4.19 †	4.21 †	4.27 †	4.30 †
$\boldsymbol{L_c}$ **(Å)**	{(1,0),(0,1)}	20.7 ± 0.8	21 ± 1	36 ± 1	25 ± 2
	{1,-1}	250 ± 5	180 ± 7	105 ± 15	50 ± 2
Primitive Unit Cell	$\boldsymbol{a = b}$ **(Å)**	4.95 ± 0.02	4.88 ± 0.02	4.99 ± 0.01	5.14 ± 0.04
	$\boldsymbol{\gamma}$ **(°)**	115.59 †	119.64 †	117.37 ± 0.01	113.25 ± 0.01
	$\boldsymbol{A}$ **(Å^2)**	22.1 ± 0.2	20.7 ± 0.2	22.2 ± 0.1	24.3 ± 0.4

Table 3.2: ***Monolayer thickness*** *and experimental uncertainties obtained from both GIXOS and XRR measurements, for the four systems investigated at π = 30 mN/m and T = 293.15 K. The data presented here are analogous of Figures 3.6 and 3.9.*

Thickness (Å)	**GIXOS**				**XRR**	
	IL_DMSO	**IL_water**	**OL_water**	**OL_DMSO**	**IL_water**	**OL_water**
Total	25.5 ± 0.7	25.7 ± 0.4	24 ± 1	24.7 ± 0.8	25 ± 3	23 ± 8
Chains	17.1 ± 0.3	17.1 ± 0.2	16.7 ± 0.5	15.9 ± 0.3	16 ± 1	17 ± 4
Heads	8.4 ± 0.4	8.5 ± 0.2	7.5 ± 0.7	8.8 ± 0.4	10 ± 2	5 ± 4

3.4 Discussion

Both the GIXD and GIXOS techniques allow for the structural study of phospholipid monolayers at the air-subphase interface in fine detail. The two methods are complementary in nature with GIXD probing lateral order and crystalline organisation, whilst GIXOS provides information about the transverse structure and electron density. The investigation of complex monolayers containing several lipid species, akin to the composition of the leaflets of RBC membrane bilayers, served to further the current knowledge base in this field where only single or dual lipid monolayers had thus far been investigated. Direct comparison of the results obtained from IL and OL monolayers served to elucidate the role of the RBC membrane in physiological cell functioning. Furthermore, the inclusion of studies of these monolayers on an aqueous-DMSO subphase at a physiological concentration of 10 vol-% could aid in justification of the solvent's use as a cryoprotectant in the storage of cord blood.

3.4.1 Grazing incidence x-ray diffraction

Comparison of inner and outer leaflet monolayers on the UPW subphase

Contrary to first appearance of a single peak, the dual fitting of the Bragg peaks measured for the IL_water system suggests a distorted hexagonal packing arrangement ($|\ \mathbf{a}\ | = |\ \mathbf{b}\ |$, $\gamma < 120\ ^\circ$). A similar result was obtained by our laboratory at Diamond Light Source, UK (unpublished). A result such as this, demonstrating high lateral order for the IL_water monolayer, was to be somewhat expected. The IL is rich in the PE phospholipid which has been shown to produce a sharp {1,-1} peak with a broad {(0,1),(1,0)} shoulder at $\pi = 20$ mN/m [73], a lower surface pressure than used in the experiments here. It follows that a higher π might induce a more ordered state and thus, a less distinguishable shoulder for the {(0,1),(1,0)} reflection. In support of this, Helm *et al.* [71] demonstrated that as surface pressure increases the Bragg peak pattern for a DPPE monolayer reduces to one sharp peak. The result presented here suggests that inclusion of other lipid species in the IL_water monolayer leads to a slight distortion of the packing from perfect hexagonal symmetry. Majewski and Stec [74] demonstrated that the mixing of DPPC and DPPS reduced the order of the lipids within the monolayer. Further, at 4.237 and 4.2145 Å, the measured d-spacings of the IL_water monolayer are much smaller than that reported for monolayers of the individual lipid species. However, it remains unclear if this is a

direct result of mixing the lipid species or the greater pressure at which these results were obtained, with both potentially being contributing factors.

In support of the ordering of the IL_water monolayer being dominated by the PE moiety, are the values that describe the primitive unit cell. Here, at 119.64°, γ deviates only slightly from 120° which describes an arrangement with perfect hexagonal symmetry. Further, the value obtained for the unit cell area, $A = 20.7$ Å^2, is only slightly greater than that reported previously for the DPPE lipid at 19.9 ± 0.2 Å^2 (independent of monolayer pressure) [48]. This is most likely a result of accommodating the larger headgroups of the other lipid species like PC and PS.

The broad diffraction pattern obtained for the OL_water monolayer suggests much less in-plane order than for the IL_water monolayer. Again, a similar result has previously been obtained by our laboratory (unpublished). Less order within the OL of the RBC lipid bilayer is not surprising due to the high concentration of the SM phospholipid species. This lipid does not appear to develop long-range crystalline order, even at higher surface pressures where other lipid species would show long-range order in the monolayer [76]. In further support that the OL monolayer structure is dominated by the SM lipid, the measured *d*-spacing of the {1,-1} peak, 4.27 Å, is in good agreement with that previously reported for monolayers of SM [75, 76]. Interestingly, the {(1,0),(0,1)} peak's *d*-spacing of 4.44 Å was the largest measured in either of the two monolayers on the UPW subphase. This could be a result of the high content of PC, for which previous literature has reported similarly large *d*-spacings [73–75]. Since PC is a dominant species within the OL, its contribution to the structural organisation of this monolayer must also be considered. Both SM and PC have previously shown unit cell areas larger than that of PE [48, 74, 76], not surprising due to the smaller size of the PE headgroup. This suggests the unit cell area of the OL monolayer would be larger than that of the IL monolayer, as established through these experiments (Table 3.1). Further, the value of $A = 22.2$ Å^2 obtained for the OL monolayer is in rough agreement with the unit cell size for the minimum molecular area required by the PC headgroup, at ∼22.5 Å^2 [91].

Effect of DMSO on the inner leaflet monolayer

Whilst the Bragg peak patterns for both the IL_water and IL_DMSO systems suggest distorted hexagonal arrangements, differences are apparent in the derived lattice parameters. The aqueous DMSO subphase causes a significant shift in the position

of the {(1,0),(0,1)} peak from q_{xy} = 1.483 to 1.408 Å^{-1}, although the FWHM remains comparable (see Table 3.1). This propagates to an increased d-spacing but comparable coherence length in the {(1,0),(0,1)} crystallographic direction of the two systems. In contrast, the q_{xy} position of the {1,-1} peak remained comparable however, the aqueous-DMSO subphase reduced this peak's FWHM from 0.03 to 0.02 Å^{-1}, in turn causing a sizeable increase in the {1,-1} coherence length of 69.89 Å. Further, the parameters describing the primitive unit cell of the IL_DMSO system were significantly different to those obtained for the IL_water system. The length of the unit cell vector increased from 4.88 to 4.95 Å and the the unit cell angle decreased by 4.05°. Overall, this gave rise to a significantly larger unit cell on the aqueous-DMSO subphase of 22.1 Å, compared to 20.7 Å on the UPW subphase.

The marked increase in the {1,-1} coherence length suggests DMSO is capable of increasing order within a monolayer akin to the IL of a RBC membrane. In support of this, Chen *et al.* [92] demonstrated that increasing DMSO concentration reduced the phase transition point between the gel and crystalline phases for DPPE, of which the IL monolayer is rich in. In addition, Brewster Angle Microscopy (BAM) has demonstrated that DMSO exhibits a condensing and caging effect on phospholipids within a monolayer, irrespective of the lipid headgroup structure [93]. In this effect the competitive hydrogen bonding between water, lipid headgroups and DMSO causes the condensation of the monolayer into lipid rich/DMSO poor and DMSO rich/lipid poor domains. Not only does the existence of these domains offer an explanation for the observed increase in coherence length, they also suggest a mechanism by which DMSO can enhance penetration of various solutes across a membrane, through the DMSO rich/lipid poor domains.

Effect of DMSO on the outer leaflet monolayer

The results presented for the OL_water and OL_DMSO systems suggest that the aqueous-DMSO subphase also had a marked effect on the OL monolayer. Whilst the OL_DMSO system was still fully described by a distorted hexagonal packing arrangement, there was much variation in the parameters between the two systems, as outlined in Table 3.1. Most notably the peak of maximum intensity switched from the {(1,0),(0,1)} peak to the {1,-1} peak, with both peaks shifting towards smaller q_{xy}, from 1.417 and 1.473 Å^{-1} to 1.330 and 1.463 Å^{-1} respectively. The FWHM of each peak significantly increased on the aqueous-DMSO subphase, by 0.0719 Å^{-1} for the {(1,0),(0,1)} peak and 0.0591 Å^{-1} for the {1,-1} peak. These changes lead to

significantly increased d-spacings and markedly reduced coherence lengths (see Table 3.1 for overview). Moreover, the parameters describing the primitive unit cell of the OL_DMSO system were significantly different to those obtained for the OL_water system. The unit cell vectors were increased from 4.99 to 5.14 Å and the angle between them decreased by 4.12°, both leading to an overall increase in the unit cell area of 2.14 Å^2. Interestingly, this was a greater difference than seen for the IL monolayer.

The interchanging of peak intensities suggests that DMSO caused a change in tilt orientation of the OL phospholipid acyl chains, with respect to the interface normal. A greater tilt angle is supported by the observed increase in unit cell area, the physical significance of which is the area occupied by a single acyl chain of a phospholipid molecule (hence, area per molecule is $2A$). The reorientation of the lipid molecules as a result of interaction with the aqueous-DMSO subphase, is likely to have occurred due to the aforementioned competitive binding between phospholipid headgroups, water and DMSO. It has been shown that water has an affinity for binding with DMSO molecules over the headgroups of the lipids. This results in an apparent dehydration of the monolayer region [94] and consequential reorientation of the headgroups [95] and thus, acyl chain tilt angle will also be affected.

Also of interest are the markedly reduced coherence lengths in both crystallographic directions, which suggests the presence of many domains of different acyl chain orientation within the OL_DMSO monolayer. However, this observation is in stark contrast to the increase in L_c observed for the IL_DMSO monolayer, suggesting that the caging effect of DMSO is not the sole cause of these smaller domains. As an alternative explanation DMSO has been implicated in the reduced packing of SM bilayers [96] which, in concurrence with the reorientating effect described above, suggests that the acyl chains of neighbouring lipids have reduced affinity for tilting in the same direction. This effect would lead to many domains of differing chain tilt direction, in turn reducing the measured coherence length. This analysis offers an explanation for the observed disordering effect of low concentrations of DMSO seen in molecular dynamics simulations [86].

3.4.2 Grazing incidence x-ray off-specular scattering

Comparison of inner to outer leaflet monolayers

For both the IL_water and OL_water monolayers the thicknesses of the acyl chain slabs fell within the limits of that suggested by the single-species monolayers [70, 75–

77]. Whilst there was a small difference (0.4 Å) in thicknesses of this region between the two monolayers it was not significant (see Table 3.2). Since phospholipids with C_{16} chains were investigated in both monolayers this is not a surprising result. The nominal difference measured could indicate that the degree of tilt, as measured from the normal to the subphase surface, varies between the monolayers.

The difference in thickness between the headgroup regions is more surprising. Even though the IL monolayer was dominated by PE (the smallest headgroup), this slab was significantly thicker than for the OL_water monolayer by 1.02 Å. However, previous literature suggests that DPPS gives rise to the largest headgroup slab [77] and for the monolayers investigated here, DPPS is included in a rather small concentration in the OL monolayer, but a much larger concentration in the IL monolayer. Therefore, this difference in PS concentration could contribute to the larger slab thickness of the IL_water monolayer headgroup region.

The electron density profiles for both the IL_water and OL_water monolayers show that the headgroup region has a greater electron density than the tail region. This is to be expected considering the chemical structures of the phospholipids, as given in Figure 3.2. The largest difference in electron density between the two monolayers occurs in the tail region, with the IL acyl chain region having the larger electron density. This difference could relate to the lipid packing as discussed in Section 3.4.1. Due to the relative lipid headgroup sizes, with the dominant IL lipid PE being comparatively smaller, it is not a surprise that the difference in electron density between the monolayers lessens as z approaches the headgroup region.

Effect of DMSO on the inner leaflet monolayer

The interaction of DMSO lowered the electron density across all regions of the IL_DMSO monolayer, in comparison to that of the IL_water monolayer. This result is of particular interest considering there is nominal change in the overall thickness of the monolayer, and individual slab regions, between the two systems. The GIXOS technique results in transverse structure of the a monolayer, measured in the footprint of the beam and then averaged across the whole monolayer. It follows that if the measurement was obtained near a DMSO rich/lipid poor domain - where the average electron density would be reduced due to the sparsity of phospholipids resulting from the caging effect of DMSO (described in Section 3.4.1) - then averaging this over the whole monolayer could give a distorted representation of the true electron density.

Effect of DMSO on the outer leaflet monolayer

In contrast to the IL monolayer, the electron density profile for the OL monolayer increased when measured on the aqueous-DMSO subphase. This change was paralleled by a significant increase in thickness of the headgroup slab (1.3 Å) and a notable decrease in the acyl chain slab thickness (0.83 Å), see Table 3.2.

The observed increase in thickness of the slab representing the headgroup could be a result of the dehydration and thus, greater exposure of the lipid headgroups on the aqueous-DMSO subphase [94]. The latter measurement could be explained as a result of the tilting of the phospholipid acyl chains, induced by DMSO interacting with and modifying the orientation of the headgroups. Increasing the tilt of the phospholipid acyl chains, with respect to the interface normal, would shorten the vertical distance from the subphase surface to the end of the lipid molecule. This would in turn confine more electrons to a smaller slab region and thus increase the electron density.

3.4.3 Comparison of GIXOS and XRR techniques

Of first note is the difference in q_z step for the GIXOS and XRR measurements, which was much larger in the XRR technique resulting in a reduced data set. Although the XRR reflectivity curves (Figure 3.8) appear a similar shape to the pseudo-reflectivity curves obtained from the GIXOS data (Figure 3.5), the XRR reflectivity curves exhibit an overall steeper gradient. This difference was propagated through into the electron density profiles, where greater density profiles were measured using the XRR technique for both monolayers. Whilst the two methods are in agreement that the IL headgroup region has a greater electron density than the OL headgroup region, the same cannot be said for the acyl chain region. Interestingly, the XRR results suggest that the OL monolayer has the greater electron density in the tail region, whilst the GIXOS results suggest the opposite. Further, in the analysis of slab thickness it is apparent that each monolayer was measured as having a greater thickness using the GIXOS technique. The difference in overall thickness between the methods were 0.23 Å for the IL monolayer and 1.74 Å for the OL monolayer, although in neither case were these significant.

Unfortunately, the large experimental uncertainties associated with the XRR results (see Table 3.2) compound any meaningful comparison, particularly with respect to the OL monolayer. These results suggest that in the context presented here, GIXOS was

the more reliable method of measurement, further adding to this method's advantages over the classical XRR technique and making it convincingly the more desirable technique of the two.

3.5 Conclusions

Synchrotron x-ray radiation has proved a useful tool in the structural analysis of monolayers akin to the composition of the leaflets of the RBC lipid bilayer. In using both GIXD and GIXOS, we have succeeded in elucidating the lateral and transverse organisation of complex mixtures of phospholipids at the air-water interface. It was this complexity of the monolayers that greatly increased the difficulty of giving physical meaning to the quantitative results, especially in considering the individual contribution of each lipid species.

GIXD results demonstrated that whilst both monolayers arranged with a distorted hexagonal symmetry, the lattice parameters were considerably different. For the OL monolayer the distance over which crystalline order was present was reduced, most probably due to the greater concentration of the SM phospholipid which has previously demonstrated to not develop long-range order.

The perpendicular slab structure of both monolayers agreed well with the range of results obtained from single lipid monolayer studies. Through the GIXOS technique it was also demonstrated that the IL monolayer had a greater overall electron density than the OL monolayer, potentially due to the packing arrangement of the different lipid species or the different headgroup structures of the dominant lipid species. Unfortunately, the comparison between the GIXOS and XRR techniques was impaired by large experimental uncertainty in the XRR study. This comparison does suggest that, for this particular experiment, parameters evaluated from the GIXOS technique are more reliable.

Finally, both monolayers were investigated on an aqueous-DMSO subphase which was at a concentration of 10 vol-%. This simulated the presence of DMSO at the membrane, at the concentration used during the cryopreservation of cord blood. The acyl chains within each monolayer retained the distorted hexagonal packing arrangement, however the area per molecule ($2A$) was increased upon DMSO interaction. Particularly for the IL monolayer GIXD measurements indicated the formation of DMSO poor/lipid rich and DMSO rich/lipid poor domains, suggesting a mechanism

for the molecular action of DMSO that supports its use as a solvent and penetration enhancer in the biological and pharmacological fields. Additionally, both GIXD and GIXOS measurements of the OL monolayer on the aqueous-DMSO subphase indicated that DMSO could have a reorientating or tilting effect on the phospholipid acyl chains. This in turn, effected the thickness of the monolayer headgroup and acyl chain regions. Curiously, the GIXD results showed that both monolayers were affected in a similar manner, but in the GIXOS measurements there was a much greater effect on the OL monolayer. This discrepancy results from the difference in fundamental measurement of each method - where GIXD measures only ordered regions but GIXOS measures both ordered and unordered regions - and suggests that the action of DMSO may be more targeted towards the regions of less order of the acyl chains within the monolayer.

4 Chemical alteration of RBC mechanical properties

4.1 Introduction

This chapter serves to present and discuss the findings of thermal fluctuation spectroscopy (TFS) studies into the chemical modification of red blood cell (RBC) membrane structural components and the effect(s) this had on the cell's mechanical properties. Four chemical treatments were used: hydrogen peroxide (H_2O_2), cumene hydroperoxide (cumOOH), diamide and dimethyl sulphoxide (DMSO), each proposed to alter the cell in a different manner. The primary target for H_2O_2 treatment is thought to be oxidisation of haemoglobin [97], initiating a cascade of interactions that affect the membrane skeleton [98]. CumOOH is also an oxidative agent, thought to primarily target the phospholipid acyl chains of the lipid bilayer [99], whilst diamide oxidatively targets the cytoskeletal proteins [100]. Finally, not generally considered oxidative DMSO is thought to alter the lipid arrangement within the bilayer [86].

4.1.1 Mechanical properties of the RBC

TFS is a static deformation technique used to examine the bending and shear moduli of the RBC membrane, utilising the natural thermal undulations of the membrane. The area modulus cannot be measured using this technique, as the energy scale is not sufficiently large enough to produce a substantial area change.

The ability of the RBC to deform is imperative for its role in the circulation. Abnormalities in deformability lead to increased flow resistance and blood viscosity [19] and results in quicker removal of cells from the circulation. Many pathophysiological conditions result in such abnormalities, but improper function can also result from osmotic concentration changes, membrane alterations, cell age or elevated levels of oxidative stress.

Previous TFS experiments have measured the bending modulus of healthy, untreated cells to be on the order of 10^{-19}J. Using the TFS method, Hale *et al.* [59] measured a value of $(5.6 \pm 0.7) \times 10^{-19}$J which was in agreement with values from their coarse-grained particle dynamics situations at 7.5×10^{-19}J [101]. As summarised in Boal [102], other measurement techniques have returned similar values for the bending modulus, but discrepancies arise when moving between deformation length scales and strain magnitudes in the measurement. Micropipette aspiration measures at a comparable wavelength to TFS, returning a bending modulus of $\sim 1.8 \times 10^{-19}$J [28], whereas the techniques of Brochard *et al.* [33] and Zilker *et al.* [103] are at smaller wavelengths, obtaining smaller values of 5×10^{-20}J and 2×10^{-20}J respectively. This discrepancy can, in part, be credited to the theoretical approximations used to interpret fluctuation results which for longer wavelengths are impacted by the cell geometry [101].

Values of the shear modulus obtained from TFS are, on average, three orders of magnitude larger than when measured using other static deformation methods. Hale *et al.* [59] presented a value of $(1.0 \pm 0.2) \times 10^{-3}$ Nm^{-1}, in stark contrast to those obtained through, for example, micropipette aspiration at (6 - 10) $\times 10^{-6}$ Nm^{-1} [13] (see Table 1.1). Since the coarse-grained particle dynamics simulations of Hale *et al.* are also in near-agreement with the static deformation experiments, this large discrepancy must arise from the application of Equation 2.17 to the long wavelength modes, at which the shear modulus is measured. This equation was derived for a flat membrane geometry which a physical cell does not have and therefore, as the wavelength of the fluctuation increases, the physical response of the cell deviates from that theoretically described [58, 101].

This is not to say that the TFS method should be discarded. The comparatively simple methodology allows for direct comparison between untreated and treated states of individual single cells, thus findings can be presented as changes in the elastic moduli *relative* to the untreated state. This negates the effects of any systematic discrepancies arising from method limitations, whilst still allowing for a comprehensive analysis and comparison.

4.1.2 Oxidative stress and antioxidant systems

Oxidative stress is a form of cellular damage resulting from an imbalance in the concentration of reactive oxygen species (ROS) within the cell. Being in an oxygen

rich environment and having an abundance of unsaturated phospholipid acyl chains in the plasma membrane, the RBC is highly susceptible to oxidative damage. Therefore, within the RBC there is a plethora of enzymatic and non-enzymatic defence systems that counteract beneficial concentrations of ROS. Age (both cellular and patient) and pathophysiological conditions have both been linked to dysregulation of ROS within the blood [104–106]. Oxidation can be artificially induced by treatment with oxidising chemicals such as H_2O_2, cumOOH or diamide.

ROS occur as either radicals or non-radicals. The former includes superoxide ($O_2^{\bullet -}$), hydroxyl ($^{\bullet}OH$) and hydroperoxyl ($HOO^{\bullet}$), whilst non-radicals include H_2O_2 and singlet oxygen ($^1O_2$) [105]. Superoxide is generated through several different enzymatic reactions and in subsequent reactions will produce H_2O_2 and $^{\bullet}OH$ [106]. The hydroxyl radical is by far the most potent and can be formed through either the Fenton reaction:

$$Fe_2^{+} + H_2O_2 \longrightarrow Fe_3^{+} + OH^{-} + {}^{\bullet}OH \tag{4.1}$$

or Harber-Weiss reaction [107]:

$$O_2^{\bullet -} + H_2O_2 \longrightarrow OH^{-} + {}^{\bullet}OH + O_2 \tag{4.2}$$

ROS can cause extensive damage to the structural components of the cell membrane through cross-linking of proteins, both in the cytoskeleton and plasma membrane, and cleaving double bonds in polyunsaturated phospholipid chains. This in turn can severely alter the mechanical properties of the cell.

Since ROS are required in many biological processes and can act as signalling molecules, in small concentrations they are highly beneficial. Therefore, to maintain proper physiological concentrations of ROS within the cell there are both enzymatic and non-enzymatic antioxidant systems present. The family of antioxidant enzymes includes superoxide dismutase (SOD), catalase (Cat), glutathione peroxidases (GSHPx) and peroxiredoxin-2 (Prx2) [104]. As suggested by its name, SOD catalyses the dismutation of $O_2^{\bullet -}$ into H_2O_2 and O_2, then in turn, Cat and GSHPx degrade H_2O_2 into oxygen and water [108]. Prx2 is most associated with the bilayer, protecting against lipid peroxidation [109].

Non-enzymatic antioxidants include glutathione (GSH) and Vitamins C and E. At concentrations of 2 - 10 mM within the RBC, GSH works both independently and collaboratively with GSHPx to remove H_2O_2 and lipid peroxides [110]. Both vitamins

C and E are essential in preventing lipid peroxidation within the plasma membrane [108, 111] where, although Vitamin C is hydrophilic and vitamin E is lipophylic, they work in partnership.

4.1.3 Dimethyl sulphoxide and RBC mechanical properties

DMSO is a versatile solvent with a myriad of uses in the biological and pharmacological fields, as outlined in Section 3.1.3. Although not an oxidant, each application of DMSO alludes to changes in the cellular membrane, with the severity dependent upon DMSO concentration. However, the specific method of action of DMSO remains poorly understood with little experimental backing, this therefore resides as an interesting area of investigation.

As an experimental method, TFS is used to determine changes in the individual elastic moduli of a cell membrane. As such changes in each moduli can be explained by alterations of the various membrane components, this places TFS as an important tool in investigating the specific effect(s) of DMSO on the red cell membrane components.

The effect of DMSO on the bending modulus of a membrane is well documented. Previous work using molecular dynamics simulations has demonstrated a 5 - fold decrease in the bending modulus of DPPC bilayers in the presence of 12 mol-% DMSO [86]. Further, this work is supported by that of Koch *et al.* [112] reporting a reduced bending modulus after treatment of RBCs with both 5 and 15% DMSO. Notably, the reduction was only statistically significant at 15%. A decreased bending modulus demonstrates that the resistance of the lipid bilayer to a bending deformation has decreased; expressly, the flexibility of the lipid bilayer has increased. Due to the solvents amphiphilic property, it comes as no surprise that notable effects on the lipid bilayer have been documented. What remains to be elucidated is the effect of DMSO on the shear modulus of the cell and hence, what effect the solvent has on the RBC cytoskeleton.

4.1.4 Chapter outline

The structural components of the RBC membrane are selectively altered by one of the three oxidising agents: H_2O_2, cumOOH or diamide. From these experiments, the elastic parameters of the altered membranes are measured and compared to results

from healthy, untreated membranes. Both spectral and edge displacement analyses are provided and then discussed, to elucidate how the physical changes of the membrane as a result of oxidisation contribute to changes in the elastic parameters. These results serve as the foundation for establishing if altered elastic parameters of the membrane contribute to reduced ATP release from RBCs, as discussed in the next chapter.

Further, the inclusion of DMSO as one of the four chemical treatments aims to increase clarity surrounding its molecular action on the cell membrane and hence, justify the significant usage of DMSO throughout the scientific field.

4.2 Experimental methods

The TFS experimental procedure and analysis is presented in Chapter 2. Here, this section serves to outline more specific details of the preparation of the chemical treatments.

4.2.1 Preparation of oxidants

Each chemical treatment was investigated at 5 different concentrations. Either a stock solution was directly diluted to give the desired concentration or a dilution series was employed. For H_2O_2 (Fisher Bioreagents, Belgium), a stock solution with concentration $c_s = 9.78$ M was diluted in a PBS buffer, with 1 g/L BSA added, to give final concentrations of 100, 200, 300, 400 and 500 μM. Due to the unstable nature of the oxidant each dilution was prepared on the same day as the experiment.

For experiments involving cumOOH (Sigma-Aldrich, USA), a 100 μM dilution was prepared from a stock solution (concentration $c_s = 5.42$ M) and a PBS buffer with 1 g/L BSA added. From this, a dilution series was used to obtain further concentrations of 10, 30, 50 and 70 μM. Due to the immiscible nature of cumOOH, solutions were sonicated for 1 minute using a finger probe sonicator (UP100H, Hielscher, Germany) before addition to the blood sample.

Diamide (Sigma-Aldrich, USA) concentrations were also diluted in series from a base solution of 10 mM, to 1, 3, 5 and 7 mM. The base solution was mixed from powdered diamide, PBS buffer and BSA (1 g/L final concentration of BSA) using $c = \frac{m}{VM}$.

Here, c is the desired concentration, m the mass of diamide required for a desired volume, V, of PBS, and $M = 172.19$ g mol^{-1} is the molar mass of diamide.

4.2.2 Preparation of dimethyl sulphoxide

Stock DMSO (>98%; Sigma-Aldrich, USA) was diluted in a PBS buffer containing 1 g/L BSA. For the purpose of the TFS study, concentrations of 1, 5 and 10 vol-% were prepared on the day of the experiment. Heavy emphasis was placed on the use of glass apparatus in handling DMSO, due to the solvent's high reactivity with plastic.

4.3 Results

This section presents the results of each of the four chemical treatments used to modify the RBC membrane structural components and the effect(s) this had on the mechanical properties of the cells.

Where fluctuation spectra are presented it should be noted that low mode number fluctuations are dominated by the shear modulus, this is the cytoskeleton's contribution to overall cell deformability. High mode number fluctuations are dominated by the bending modulus, accounting for the lipid bilayer's contribution.

4.3.1 Oxidative modification using hydrogen peroxide

Figure 4.1 (left) details the typical effect of H_2O_2 on the fluctuation spectra of RBCs at each of the five concentrations used to modify the RBC membrane. In the case of each concentration it is apparent that the cell was affected in a time-dependent manner. The mean-square fluctuations are steadily dampened over the course of the experiment, with the severity of the dampening increased with increasing H_2O_2 concentration. Smaller concentrations appeared to affect the lower modes the most, with higher modes appearing relatively unaffected until the concentration of the treatment became more extreme (at 400 μM).

The membrane elastic parameters can be obtained from fitting the experimental data with Equation 2.17. Since TFS allows for single cell observations, this made for easy comparison of the elastic moduli between pre- and post-treatment for each individual cell. Therefore, post-treatment changes of the elastic moduli were normalised to the

value obtained from the cell in its untreated state. The average sample change in both the bending and shear moduli are presented in Figure 4.2, where the error bars represent the standard error in the mean of 8 (100 μM), 12 (200 μM), 7 (300 μM), 7 (400 μM) and 5 (500 μuM) cells respectively. It is worth noting that the spectra of most cells in both the 400 and 500 μM samples indicated that the cells were too stiff for further valid analysis beyond 50 minutes.

H_2O_2 treatment does not appear to largely affect the bending modulus at lower concentrations of 100 - 300 μM. However, at 400 and 500 μM the bending modulus increased up to a value some 3-fold greater than pre-treatment. On the contrary, after 90 minutes there was already a 50% increase in the shear modulus for the lowest concentration of H_2O_2 at 100 μM. The shear modulus then increased in a concentration-dependent manner through the 90 minutes of the experiment. For both the bending modulus and shear modulus, a large difference in the severity of the effect of H_2O_2 treatment was present between concentrations less than or equal to, and greater than 300 μM.

As an alternative to the mode-decomposed fluctuation analysis presented above, the radial fluctuation histograms provide sensitive detail as to changes in the overall fluctuations of the cell. Figure 4.1 (right) demonstrates the marked changes in the normal distribution of the radii, for each of the spectra presented. Over the course of each experiment, changes in the histogram profiles became more prominent, with this trend also reflected when comparing increasing concentrations of H_2O_2. The normalised standard deviation, Δ/Δ_0, further demonstrated that for each concentration of H_2O_2, the overall fluctuations of the cell were diminished over the course of the experiment (Figure 4.3). Further, the rate of change can be inferred from the gradient in this trend. This indicated that by increasing the concentration of H_2O_2, fluctuations were dampened at a quicker rate. That is, the cell became increasingly more stiff with increasing H_2O_2 concentration.

4.3.2 Oxidative modification using cumene hydroperoxide

The effect of cumOOH on the fluctuation spectra of RBCs is represented in Figure 4.4 (left). There appeared a concentration-dependent dampening of fluctuation amplitudes across the whole spectra, although it remained difficult to determine if both the lower and higher modes were affected in a similar manner.

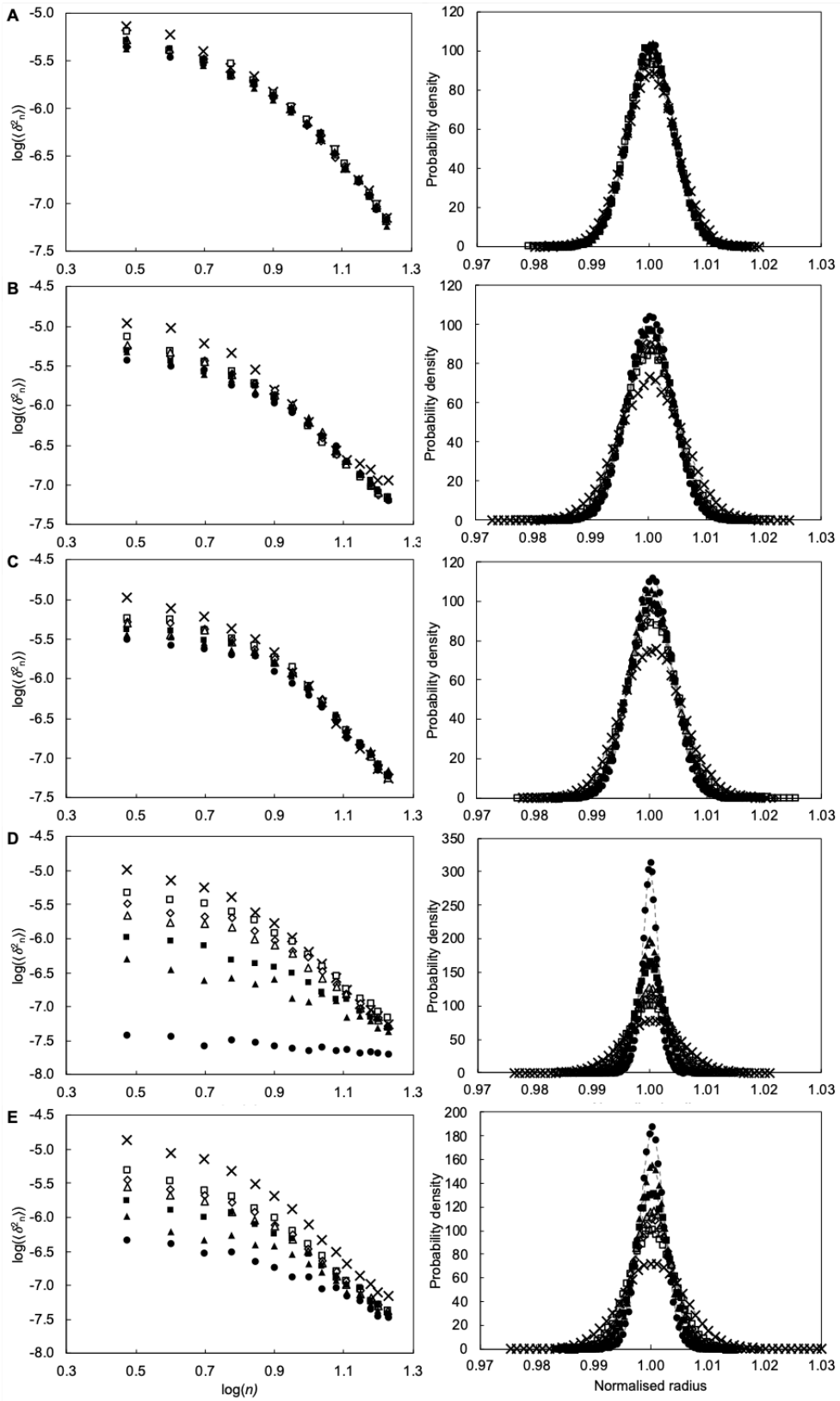

Figure 4.1: ***Fluctuation spectra and radial displacement histograms for RBCs treated with H_2O_2.*** *Spectra (left) and radial displacement histograms (right) are presented for cells treated with 100, 200, 300, 400, and 500 μM H_2O_2 (***A** *to* **E***). Measurements were made pre-treatment (×) and at the following minutes post-treatment: 10 (□), 20 (◊), 30 (△), 50 (■), 70 (▲) and 90 (●).*

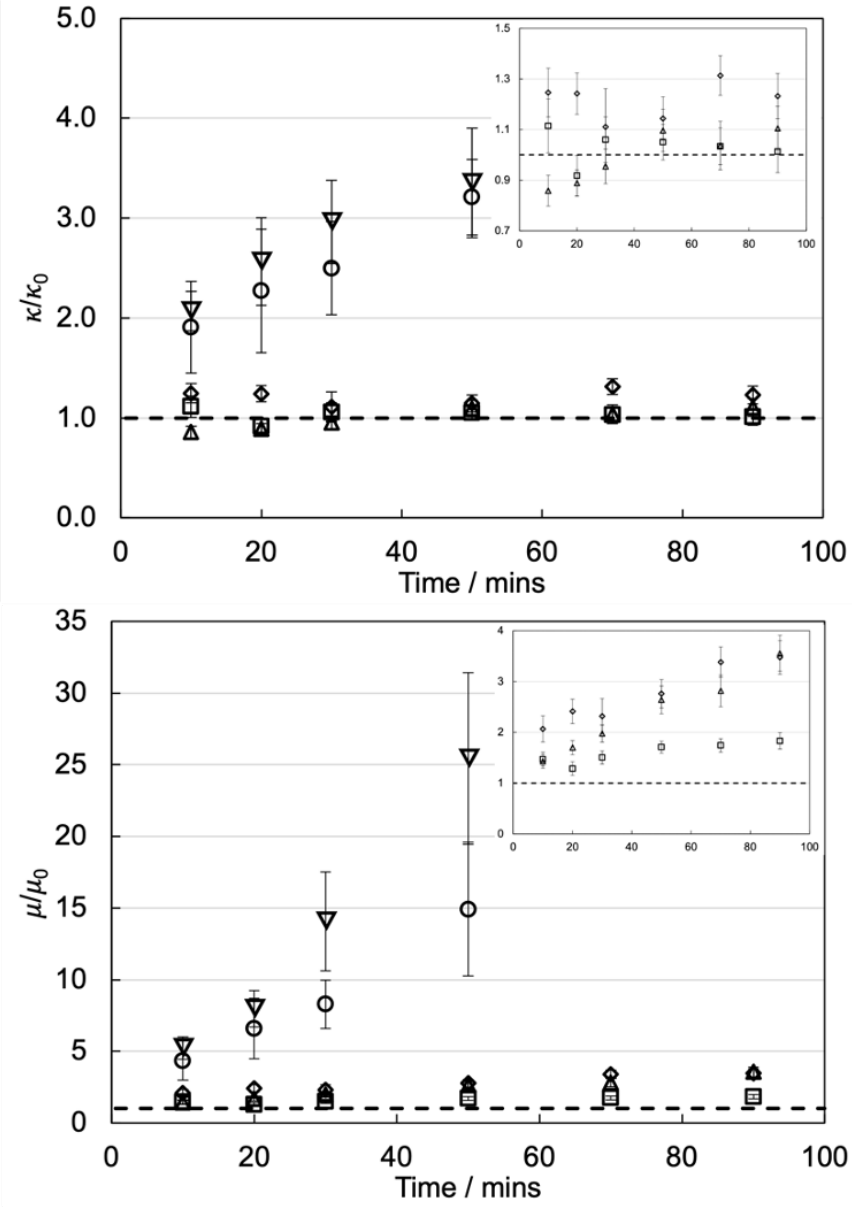

Figure 4.2: ***Effect of H_2O_2 on the elastic moduli of the RBC.*** *Change in bending (top) and shear (bottom) moduli of the RBC, relative to the untreated cell, for cells treated with 100 μM (□), 200 μM (◊), 300 μM (△), 400 μM (◯), and 500 μM (▽) H_2O_2. The dashed line is at a value of 1, indicating no change in parameter from the cell's untreated state. Standard error is given as the experimental uncertainty. Insets detail the small effects of the lower concentrations (100 - 300 μM) of H_2O_2.*

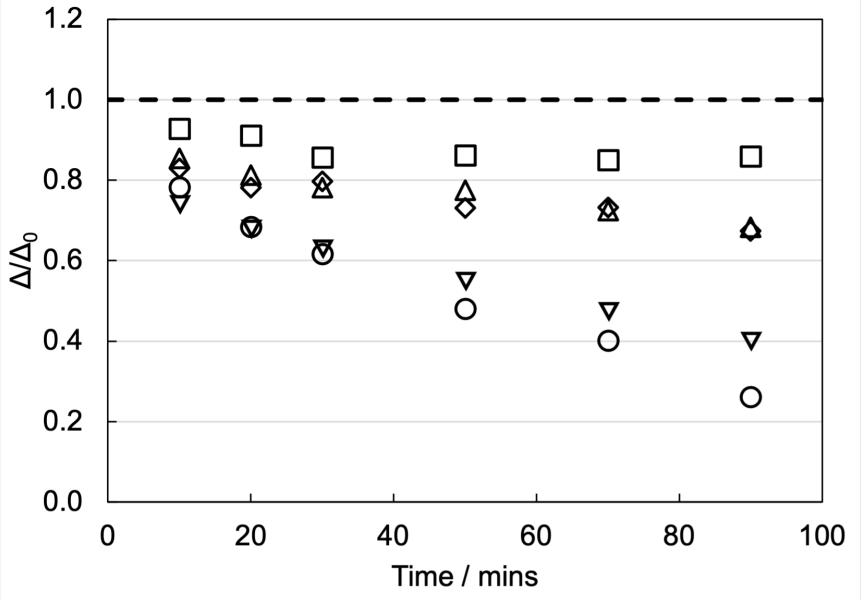

Figure 4.3: ***Kinetics of the cell response to H_2O_2 treatment.*** *Normalised cell radial displacement standard deviation as a function of time, for cells treated with 100 μM (□), 200 μM (◊), 300 μM (△), 400 μM (◯), and 500 μM (▽) H_2O_2. The dashed line represents $\Delta/\Delta_0 = 1$, indicating no change in parameter from the cell's untreated state. Experimental uncertainty lies within the point size.*

The spectra appeared to display kinks in the gradient at higher mode numbers, a possible artefact of the experimental design. The cumOOH treatment appeared to affect the slight adhesion of the cells to the microscope slide, resulting in many cells being flushed from the field of view during the exchange of the buffer with that containing the cumOOH treatment (this effect was also reported by Sinha *et al.* [113]). Analysis could only be performed on the cells that had a stronger adhesion to the microscope slide and therefore remained at the end of the buffer exchange. This could be the reason for the observed irregularities in the highest modes which are dominated by the lipid bilayer and therefore, more likely to be affected by greater adhesion to the microscope slide.

The values of the elastic parameters were extracted from the experimental data and are presented in Figure 4.5. In a similar manner to how results were presented for H_2O_2 treatment, the normalised sample average is presented and the error bars denote the standard error in the mean of 10 (10 μM), 6 (30 μM), 8 (50 μM), 5 (70 μM) and 6 (100 μM) cells respectively.

The maximum incubation period for cumOOH treatment was largely truncated especially for the higher concentrations (70 and 100 μM), where it became impossible

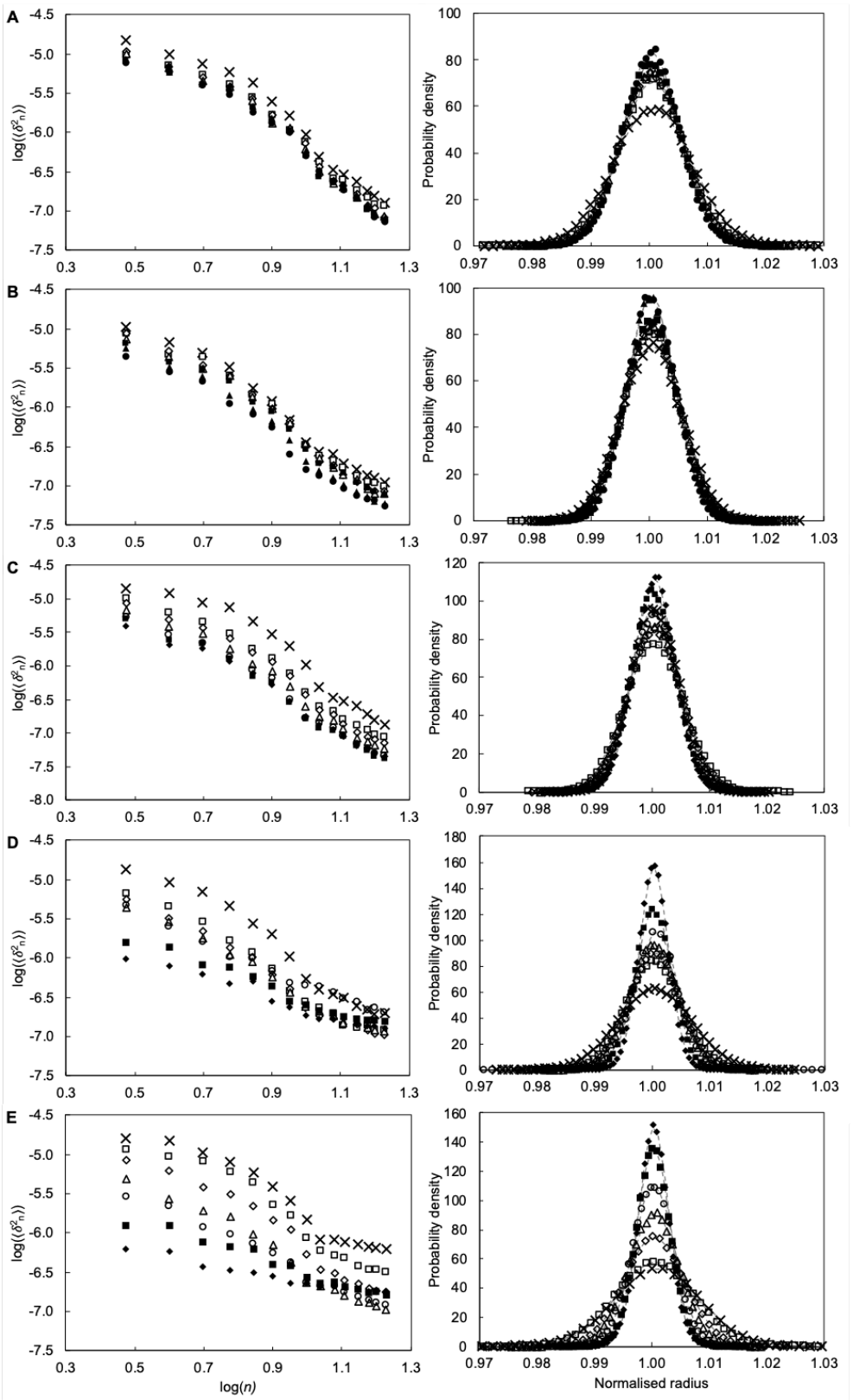

Figure 4.4: ***Fluctuation spectra and radial displacement histograms for RBCs treated with cumOOH.*** *Spectra (left) and radial displacement histograms (right) are presented for cells treated with 10, 30, 50, 70, and 100 μM cumOOH (***A** *to* **E***). Measurements were made pre-treatment (×) and at the following minutes post-treatment: 10 (□), 20 (◊), 30 (△), 40 (◯), 50 (■), 60 (♦), 70 (▲) and 90 (●).*

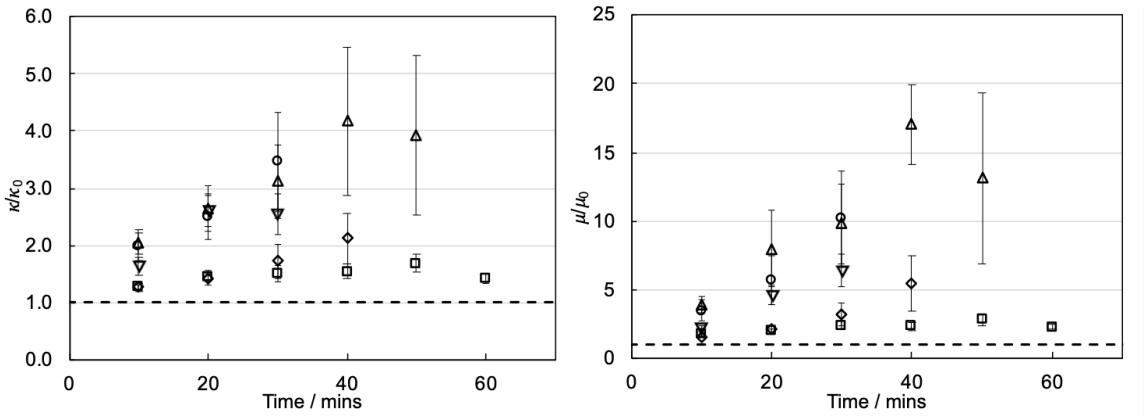

Figure 4.5: ***Effect of cumOOH on the elastic moduli of the RBC.*** *Change in bending (left) and shear (right) moduli of the RBC, relative to the untreated cell, for cells treated with 10 μM (□), 30 μM (◊), 50 μM (△), 70 μM (◯), and 100 μM (▽) cumOOH. The dashed line is at a value of 1, indicating no change in parameter from the cell's untreated state. Standard error is given as the experimental uncertainty.*

to extract the moduli from the experimental data for measurement intervals greater than 30 minutes. For both moduli two distinct trends appeared, dependant on the severity of the cumOOH concentration. For the lower concentrations, 10 and 30 μM, the bending modulus gradually increased up to a maximum 2-fold change over the 60 minutes experiment. Treatment with any higher concentration resulted in a quicker increase in the bending modulus, up to ∼3-fold after just 30 minutes. Similarly, the lower concentrations had a more gradual effect on the shear modulus, whereas the larger concentrations reached a 10-fold increase by the 30 minutes interval.

Observing the radial fluctuation histograms, it was evident that cumOOH treatment had a marked effect on the overall fluctuations of the cell, increasing in severity with increasing cumOOH concentration (Figure 4.4, right). The trend in the normalised standard deviations of these histograms, presented in Figure 4.6, further supports this notion. Not only does an increased concentration of cumOOH have a greater dampening effect, it also occurs at a quicker rate.

4.3.3 Oxidative modification using diamide

The typical evolution of the fluctuation spectra for cells treated with diamide are displayed in Figure 4.7. Diamide treatment caused a dampening in the fluctuation amplitudes across all modes of the spectra, although it remains unclear if the degree of dampening was concentration dependent. After the initial effect of the treatment,

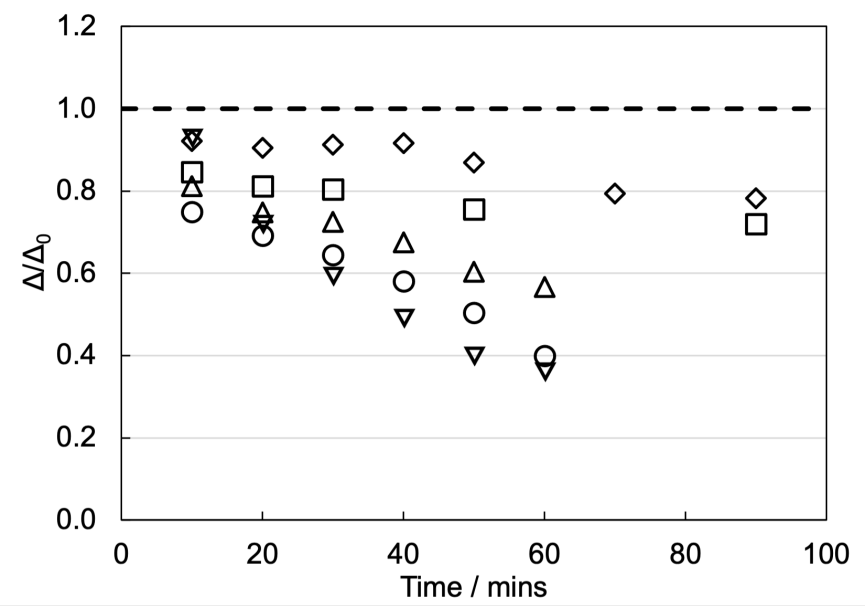

Figure 4.6: ***Kinetics of the cell response to cumOOH treatment.*** *Normalised cell radial displacement standard deviation as a function of time for cells treated with 10 μM (□), 30 μM (◊), 50 μM (△), 70 μM (◯), and 100 μM (▽) cumOOH. The dashed line represents $\Delta/\Delta_0 = 1$, indicating no change in parameter from the cell's untreated state. Experimental uncertainty lies within the point size.*

the incubation time appeared to be a mostly independent factor due to no apparent large deviations between the later spectra.

Moduli were obtained from fitting the spectra (Figure 4.7, left) with Equation 2.17. The normalised sample-average changes in both moduli are presented in Figure 4.8 as a function of diamide concentration. Error bars denote the standard error in the mean of 6 (1 mM), 6 (3 mM), 6 (5 mM), 5 (7 mM) and 5 (10 mM) cells respectively.

Figure 4.8 supports the observation that after oxidative modification with diamide, the elastic moduli of the cell were predominantly altered within the first 10 - 20 minutes of the experiment. After this initial change both moduli remained fairly constant throughout the remainder of the experiment. This trend is present in the results of each of the five concentrations of diamide used. The effect on the bending modulus increased with increasing concentration of diamide, however there appeared to be little concentration-dependent effect on the shear modulus, unless the concentration was significantly large (10 mM). At this concentration, it became impossible to extract the moduli during the fitting of the spectra, for time points greater than 30 minutes.

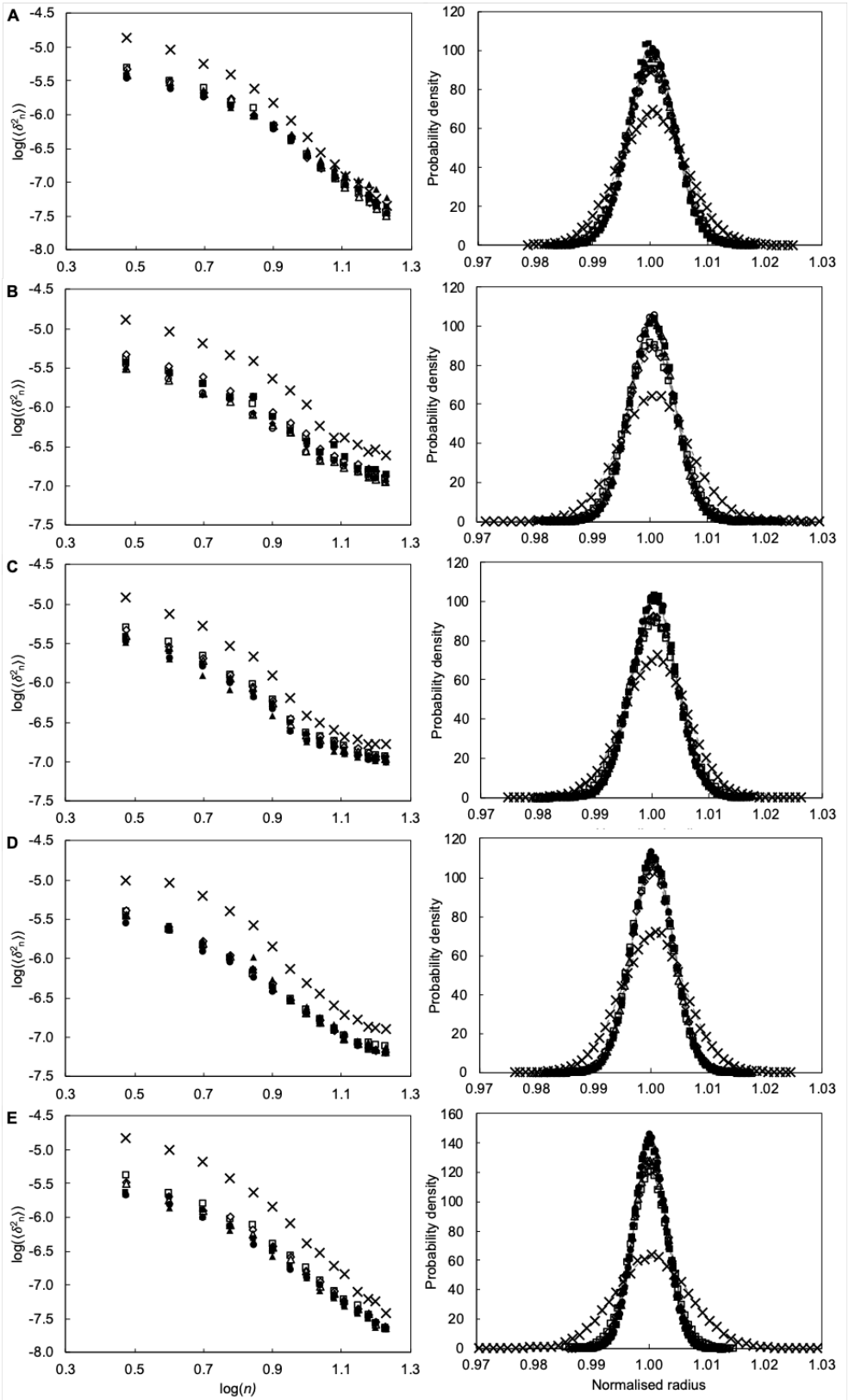

Figure 4.7: ***Fluctuation spectra and radial displacement histograms for RBCs treated with diamide.*** *Spectra (left) and radial displacement histograms (right) are presented for cells treated with 1, 3, 5, 7, and 10 mM diamide (***A** *to* **E***). Measurements were made pre-treatment* (×) *and at the following minutes post-treatment: 10* (□)*, 20* (◊)*, 30* (△)*, 40* (◯)*, 50* (■)*, 60* (♦)*, 70* (▲) *and 90* (●)*.*

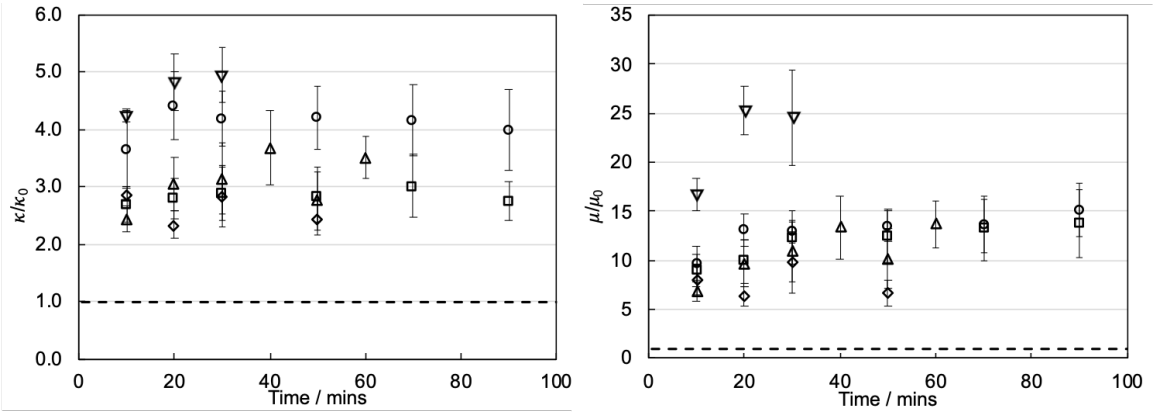

Figure 4.8: ***Effect of diamide on the elastic moduli of the RBC.*** *Change in bending (left) and shear (right) moduli of the RBC, relative to the untreated cell, for cells treated with 1 mM (□), 3 mM (◊), 5 mM (△), 7 mM (◯), and 10 mM (▽) diamide. The dashed line represents a value of 1, indicating no change in parameter from the cell's untreated state. Standard error is given as the experimental uncertainty.*

The radial fluctuation histograms and their normalised standard deviations (Figures 4.7, right, and 4.9 respectively) further demonstrated that the changes inflicted by diamide occurred mostly within the first 10 minutes after treatment, after which the rate of fluctuation dampening was greatly reduced. Comparing the normalised standard deviations between diamide concentrations additionally suggested that the degree of overall fluctuation dampening was largely concentration independent.

4.3.4 Chemical alteration with dimethyl sulphoxide

DMSO appeared to have a relatively small effect on the RBC fluctuation spectra, which varied both by treatment concentration and individual mode response as presented in Figure 4.10 (left). At 1 vol-% the lower modes of the spectra, corresponding to the shear modulus, exhibited a dampening after the DMSO treatment. In contrast, the higher modes were slightly up-shifted, indicating a small decrease in the bending modulus. For the 5 vol-% treatment, the lower modes appeared largely unaffected but the higher modes exhibited a more pronounced up-shift. From the presented spectra, the effect of the 10 vol-% treatment on the lower modes remained unclear, but the higher modes demonstrated an initial up-shift before relaxing towards the pre-treatment value over the course of the experiment.

The effect of DMSO on the mechanical properties of the cell is presented in Figure 4.11, where error bars denote the standard error in the mean of 7 cells (1 vol-%), 5

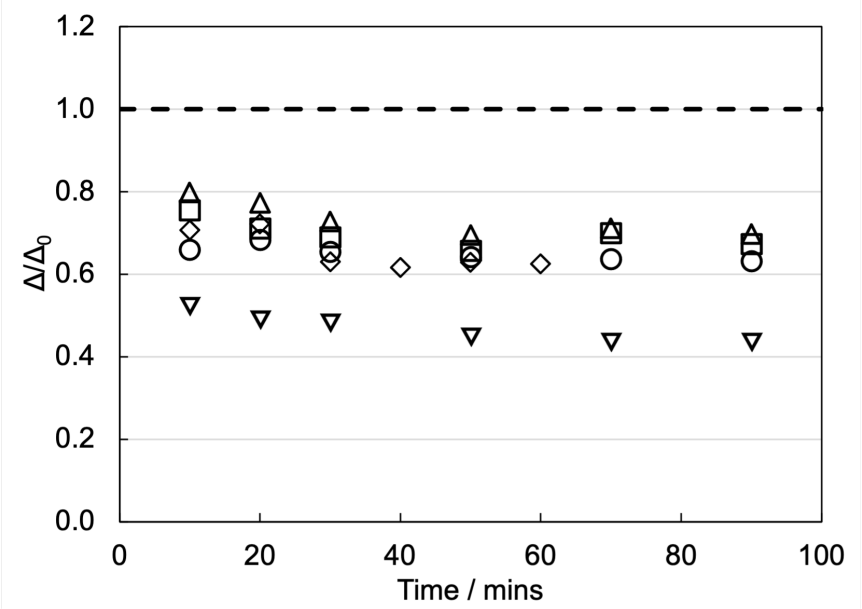

Figure 4.9: ***Kinetics of the cell response to diamide treatment.*** *Normalised cell radial displacement standard deviation as a function of time for cells treated with 1 mM (□), 3 mM (◊), 5 mM (△), 7 mM (◯), and 10 mM (▽) diamide. The dashed line represents $\Delta/\Delta_0 = 1$, indicating no change in parameter from the cell's untreated state. Experimental uncertainty lies within the point size.*

cells (5 vol-%) and 6 cells (10 vol-%). This work has been partially published as part of a collaborative project [96].

The most noticeable change in the bending modulus occurs within the first 10 minutes post-treatment, regardless of DMSO concentration, as indicated by the initial sharp change in κ/κ_0. The 1 vol-% treatment resulted in a ∼40% increase of the bending modulus, whereas the two larger concentrations caused a decrease with a weaker effect seen for cells treated with 10 vol-% (approximately -30% and -20%, respectively). The 1 vol-% treatment then remained constant at $\kappa/\kappa_0 \approx 1.4$ for the duration of the experiment, whilst cells that underwent either the 5 or 10 vol-% treatment displayed restorative behaviours over the course of the experiment. The restoration of the samples treated with 10 vol-% DMSO was quicker than that of the samples treated with 5 vol-%, reaching pre-treatment values within the time frame of the experiment.

Changes in the shear modulus followed much the same trend as the bending modulus. Here, μ was strongly altered within the first 10 minutes post-treatment. Again, the effect on the cells treated with 1 vol-% DMSO remained constant after this time, at almost double the untreated value. However, cells with the 5 or 10 vol-% treatment exhibited an initial decrease, followed by recovery towards the pre-treatment value

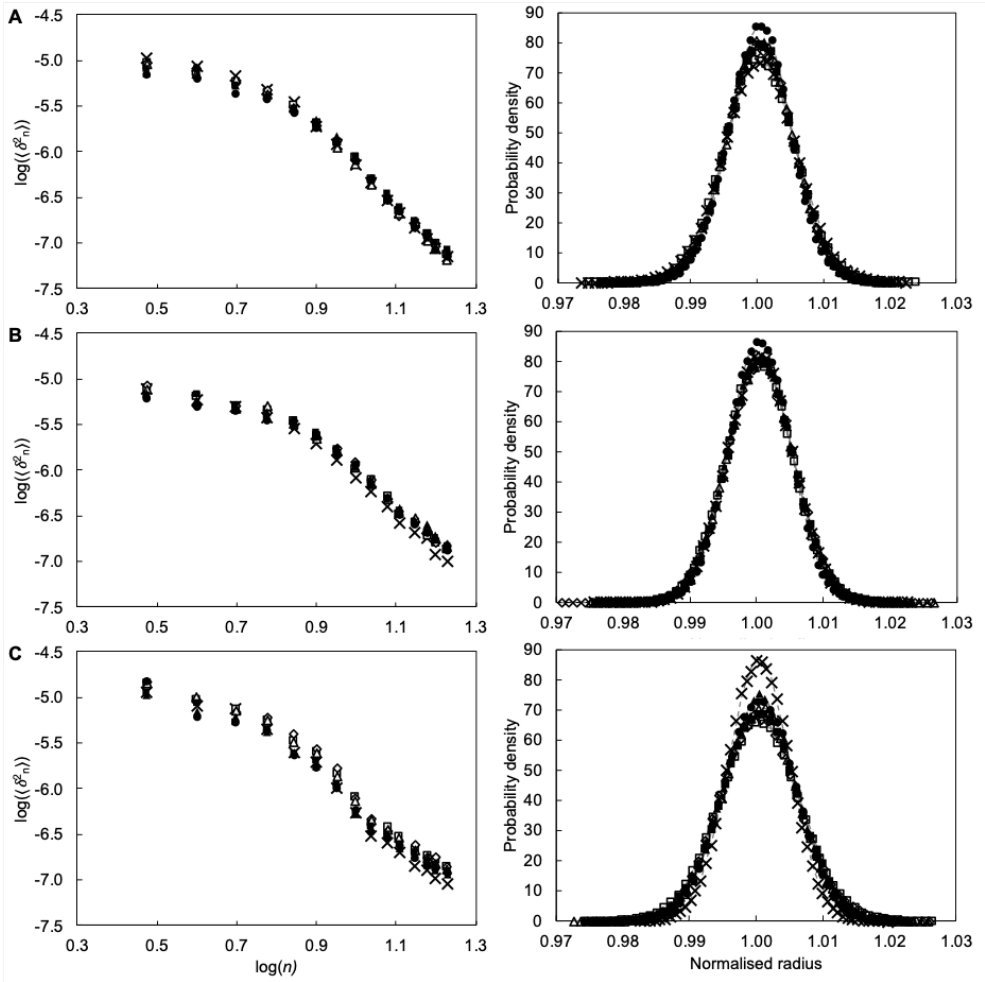

Figure 4.10: ***Fluctuation spectra and radial displacement histograms for RBCs treated with DMSO.*** *Spectra (left) and radial displacement histograms (right) are presented for cells treated with 1, 5, and 10 vol-% DMSO (***A** *to* **C***). Measurements were made pre-treatment* (×) *and at the following minutes post-treatment: 10* (□)*, 20* (◊)*, 30* (△)*, 50* (■)*, 70* (▲) *and 90* (●)*.*

at around 50 minutes. Interestingly, both moduli were affected to a similar degree which was a trend not seen in the results of the oxidative modification study.

Since changes in the spectra of DMSO treated cells were relatively small, the radial fluctuation histograms in Figure 4.10 (right) can provide a more sensitive measurement to show how the overall fluctuations of the cells were affected. The change in the normalised standard deviation (Figure 4.12) of the cell treated with 1 vol-% displayed an initial steady decrease up to 40 minutes, followed by a short plateau, and then a further decrease after 70 minutes. This demonstrates that the fluctuations were first dampened at a steady rate which began to slow after 40 minutes. The converse is true for the trend in both the 5 vol-% and 10 vol-% treatments. Albeit at differing rates, both the cells treated with higher concentrations saw an initial increase in overall fluctuations before a reduction towards the pre-treatment value, as mirrored in the elastic moduli given in Figure 4.11.

4.4 Discussion

Chemical modification of the RBC membrane was achieved using H_2O_2, cumOOH, diamide and DMSO. The effect of each chemical on the mechanical properties of the RBC was investigated using TFS. This method was chosen due to its ability to simultaneously measure the bending and shear moduli of the cell, alongside being a sensitive measure of overall cellular deformability through radial displacement analysis. From previous work in this area it was anticipated that the membrane structural components and, hence, the elastic moduli could be selectively modified upon specific oxidative treatment of the cell. Results are in agreement with this, demonstrating an affinity of each of the treatments with a specific component of the RBC membrane. Additionally, the DMSO treatment of RBCs and subsequent quantification of the effect on the mechanical properties of the cell, aids in furthering the understanding of the molecular action of DMSO on the membrane.

4.4.1 Oxidative modification of the RBC mechanical properties

Hydrogen peroxide

The action of H_2O_2 on the red cell cytoskeleton is well documented in the literature. As a water soluble molecule, H_2O_2 will more readily incorporate itself in the cytoplasm

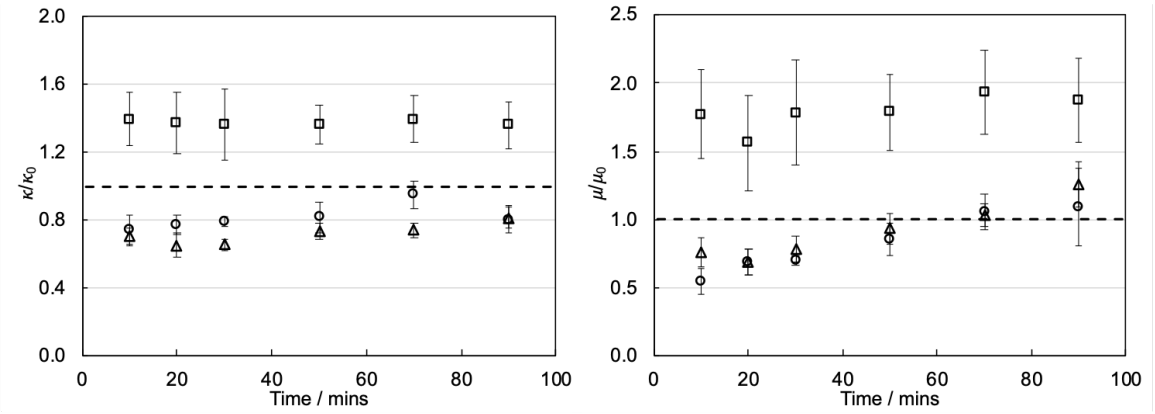

Figure 4.11: ***Effect of DMSO on the elastic moduli of the RBC.*** *Change in bending (left) and shear (right) moduli of the RBC, relative to the untreated cell, for cells treated with 1 vol-% (□), 5 vol-% (△), and 10 vol-% (◯) DMSO. The dashed line represents a value of 1, indicating no change in parameter from the cell's untreated state. Standard error is given as the experimental uncertainty.*

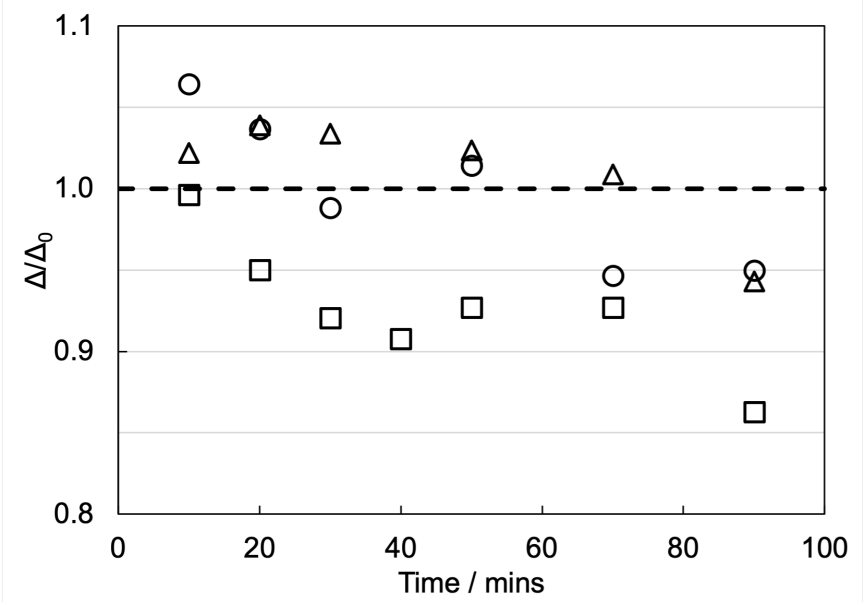

Figure 4.12: ***Kinetics of the cell response to DMSO treatment.*** *Normalised cell radial displacement standard deviation as a function of time for cells treated with 1 vol-% (□), 5 vol-% (△), and 10 vol-% (◯) DMSO. The dashed line represents* $\Delta/\Delta_0 = 1$*, indicating no change in parameter from the cell's untreated state. Experimental uncertainty lies within the point size.*

of the cell, rather than remain in the non-polar acyl chain region of the phospholipid bilayer. The results presented in Figure 4.2 support this as, across all concentrations of H_2O_2 treatment, a larger effect was seen on the shear modulus, indicating that the cytoplasm-facing cytoskeleton was affected more than the lipid bilayer. These results are in good agreement with previous studies using H_2O_2 to chemically stiffen the membrane [59, 114, 115]. Yet most of these studies, with the exception of Hale *et al.* [59], investigated the deformability of the cell as a whole, rather than attempting to distinguish between the contribution of each structural component to overall cellular mechanics.

The bending modulus remained largely unaffected by the H_2O_2 treatment up until the more excessive concentrations of H_2O_2 were used. The bending modulus accounts for the lipid bilayer's contribution to the mechanics of the membrane and therefore, these results agree well with previous studies that have demonstrated lipid peroxidation as not the main consequence of H_2O_2 induced damage. Prior treatment of cells with carbon monoxide (CO) [115, 116] or the antioxidant butylated hydroxytoluene (BHT) [114] were used to demonstrate this. CO treatment negated any formation of the lipid peroxide marker malonyldialdehyde, and the generation of fluorescent amino immunopropene derivatives became obsolete after BHT treatment.

The results of Mendanha *et al.* [98] demonstrated that only H_2O_2 treatments exceeding 300 μM caused significant lipid peroxidation, a trend that these experiments are in agreement with. Using electron paramagnetic resonance spectroscopy to quantify free sulfhydryl (SH) groups at the membrane, Mendanha *et al.* demonstrated that the membrane undergoes a concentration-mediated response to H_2O_2 treatment. Below 300 μM the SH groups at the membrane increased, presumably due to the cross-linking of haemoglobin to the spectrin cytoskeleton (see shear modulus discussion). Above 300 μM, the number of free SH groups began to decrease, coupled with an increase in thiobarbituric acid reactive species production and cell haemolysis. The resulting hypothesis was that haemolysis must be a consequence of lipid peroxidation and therefore, so too must be the reduction in SH groups. This could well explain the concentration-dependent changes observed in the bending modulus, presented in Figure 4.2.

The mostly concomitant effect of H_2O_2 treatment on the cytoskeleton of the cell is well documented in the literature with the primary oxidative target of H_2O_2 being haemoglobin. The results presented in Figures 4.1 and 4.2 are in agreement with this, revealing that H_2O_2 had a significant effect on the shear modulus of the red cell,

where even at the lowest concentration a 50% increase in shear modulus was observed. Upon treatment with H_2O_2, the haemoglobin will rapidly oxidise giving rise to highly volatile ferryl and/or hydroxyl radicals [117]. These radicals react with anything in their near vicinity, making haemoglobin not only a source of radical formation but also a primary target of radical action. Once oxidised, the damaged haemoglobin has been shown to form cross-linked complexes with the spectrin filaments of the cytoskeleton [118]. This decreases RBC deformability [119] and thus increases the shear elastic modulus of the RBC membrane.

Cumene hydroperoxide

CumOOH has previously been reported to cause stiffening of the membrane [59, 113], therefore the results presented in Figure 4.5 are of no surprise.

Most of the literature focuses on the oxidative target of cumOOH as the membrane phospholipids, due to the peroxide's water-immiscible nature and therefore affinity for the enclosed non-polar region created by the acyl chains of the bilayer lipids [99, 117, 120]. The observed increase in bending modulus could result from the oxidation of the polyunsaturated lipid tails, which are cleaved at the double bond [121] with only a single bond remaining. This would reduce the area per molecule required and therefore, could lead to an increase in lipid packing density. This has been verified by loss of membrane area, in terms of radius shrinkage, by both Hale *et al.* [59] and Jewell *et al.* [122].

The presented results also detailed a significant effect on the shear modulus of the membrane and therefore, since the shear modulus is dominated by the cytoskeleton, oxidation is not limited to the bilayer alone. Van den Berg *et al.* described the kinetics of cumOOH treatment as a slow membrane-mediated release of the peroxide into the cytosol [117]; i.e. a small fraction of cumOOH is miscible in the aqueous cytosol [123]. Once in the cytosol, cumOOH can readily oxidise haemoglobin closest to the membrane region, forming met-haemoglobin and inducing spectrin – haemoglobin cross-linking. As a result, the cytoskeleton is damaged in a manner similar to that induced by H_2O_2.

Diamide

With both the bending and shear moduli having increased over the range of diamide concentrations used, these results are in good agreement with previous literature that suggests diamide decreases deformability of the cell [112, 113, 124–127]. Sinha *et al.* [113] demonstrated that diamide treatments above 3 mM could lead to an altered cell morphology, similar to results observed in a small number of experiments here. Any cells displaying such echinocytic behaviour post-treatment were removed from further analysis, preventing the inclusion of inaccurate readings since TFS cannot be used to analyse this morphology.

In a short summary of past literature, Forsyth *et al.* [128] noted discrepancies in the reporting of the effect of diamide on the mechanical properties of the cell, suggesting the result would be method dependent. Methods that resembled more *in vivo* dynamics reported no reduction in deformation with respect to diamide treatment, however, these methods relied heavily on large-scale deformations of the cell, unlike TFS which relies on small deformations of the membrane. It must further be noted that these papers only make up a small fraction of the literature and the widely accepted theory is that diamide is a stiffening agent.

Phospholipid peroxidation induced by diamide has been demonstrated by Power *et al.* [129], in an attempt to assess if GSH protected mammalian cells against peroxidative damage. Power *et al.* treated cells with diamide, thought to oxidise the GSH, but their method proved unsuccessful when they observed direct lipid peroxidation at concentrations marginally above those required to fully oxidise GSH. Further, the reorganisation of skeletal proteins (reduced mesh size of the cytoskeleton has been shown by Sinha *et al.* [113]) could inevitably lead to a disruption of lipid order on the inner leaflet of the bilayer and thus, affect the bending modulus of the membrane. Incidentally, this is also the cause of echinocytes, already known to form upon treatment with the larger diamide concentrations. Since the bilayer is in such close proximity to the spectrin network, particularly that the two structures are coupled together, it is not a surprise that a change in the spectrin network could modify the bending modulus as demonstrated by the results presented in Figure 4.8.

It is well documented that the action of diamide is primarily on the spectrin network of the cell. More specifically, cysteine is an amino acid of the spectrin protein and diamide has been shown to have a specific affinity for oxidising its sulfhydryl group [100]. This creates a disulphide bond between the thiol groups, leading to cross-linking

between spectrin filaments [126]. It has also been shown that average spectrin length and mesh size decrease under diamide treatment [113], further supporting the idea of spectrin cross-linking. With this in mind, it is not surprising that diamide has been shown to alter the morphology of cells. The results presented here suggest that this cross-linking action leads to a marked reduction in RBC cytoskeleton deformability. This effect is in agreement with Engelhardt *et al.* [35], who observed an 8-fold increase in the shear modulus after diamide treatment at a concentration of 1 mM.

4.4.2 Effect of dimethyl sulphoxide on the mechanical properties of the RBC membrane

The chemical properties of DMSO have led to its many uses in pharmacological and biochemical fields. However, the mechanisms of action of DMSO remain poorly understood and in many cases left only to theory. This highlights the importance of obtaining a better understanding of this amphiphilic molecule via experimental approaches.

The data presented in Figure 4.11 agrees well with literature that suggests higher concentrations of DMSO lead to a reduced bending modulus [86, 112]. However, the bending modulus increasing with low concentrations of DMSO has not been previously reported, to our knowledge. The shear modulus is relatively under reported in the literature, most likely because the primary target of DMSO is thought to be the phospholipid bilayer with no contribution to the shear modulus.

The increase in bending modulus of the cells treated with 1 vol-% has not previously been seen. This phenomenon could be a result of DMSO reducing the bilayer thickness and increasing phospholipid packing, as reported in molecular dynamics simulations for bilayer systems treated with low concentrations of DMSO [87]. At greater concentrations, a larger number of DMSO molecules will be incorporated into the bilayer, thought to reside just below the lipid head groups. When positioned here, DMSO would act as a spacer molecule increasing the average area per molecule of each lipid and decreasing the resistance of the bilayer to bending deformations [86]. It is as expected that we observe the bending modulus decrease for 5 and 10 vol-% treatments.

Whilst there is little in the literature to explain how DMSO would modify the cytoskeleton of the cell and hence, the shear modulus, it is not surprising that there are

small alterations in these experiments. DMSO causes structural changes to the phospholipid bilayer which could lead to the dissolution of lipids from, followed by formation of transient pores across, the membrane [87]. With the cytoskeleton coupled to the bilayer it could be speculated that in these instances, the spectrin filament arrangement may also undergo a perturbation or local decoupling from the bilayer and, hence, alter the shear modulus of the system. This idea is supported as the concentration dependent effect of DMSO on the shear modulus of the cell follows that of the bending modulus.

These results provide experimental evidence of the impact of DMSO on the elastic moduli of the cell membrane and hence, help elucidate the effect of DMSO on the structural components of the RBC membrane. It is evident that DMSO only has a weak effect on the membrane and that recovery after treatment is possible. Both of these findings go some way to justify the many uses of DMSO, especially as a cryoprotectant, without causing major or long lasting cellular damage in terms of membrane mechanical properties.

4.5 Conclusions

This chapter presented an investigation into the individual contribution of the structural components of the RBC to overall cell mechanics. Obtained through TFS, the bending and shear moduli were compared between healthy cells and the same cells treated with various chemical modifiers at a range of concentrations.

Through a large modification of the shear modulus after treatment, the results confirm that H_2O_2 has an affinity for oxidising haemoglobin, in turn causing cross-linking with the spectrin cytoskeleton. The bending modulus was only significantly modified upon treatment with the highest concentrations, further supporting that the lipid bilayer is not the primary target of H_2O_2 oxidisation. Under cumOOH treatment both moduli were increased, consistent with observations that cumOOH targets the lipid bilayer but can also leak into the cytosol where it will affect the cytoskeleton. The degradation of the mechanical properties of the cellular membrane under treatment with cumOOH was observed to be quicker than when treated with H_2O_2, even at smaller concentrations. This could have a 3-fold explanation: cumOOH targets more components of the cell, H_2O_2 must first access the cytosol whereas cumOOH is readily incorporated into the bilayer and/or the immiscible nature of cumOOH may have led to higher local concentrations of cumOOH.

Diamide was demonstrated to target both the lipid bilayer and the cytoskeleton in a oxidative manner, adding to similar conclusions found in the available literature focusing on RBC treatment with diamide. A direct comparison between diamide and the other chemical treatments should be cautious, owing to the significantly higher range of diamide concentrations. However, it is worth noting that the maximum concentration of H_2O_2 (500 μM) was twenty times smaller than the maximum concentration of diamide (10 mM), but had a similar effect on the shear modulus. This suggests that the oxidative action of H_2O_2 is much more effective than diamide.

DMSO differs from the previous three chemical treatments as it is not typically considered an oxidative agent. Previously lacking experimental reasoning, these results aid in the explanation and justification of the pharmacological and biochemical uses of DMSO. Of significant importance, it has been demonstrated here that the mechanical properties of the membrane are able to recover from insult with physiologically relevant concentrations of DMSO.

5 Mechanically stimulated ATP release from the RBC

5.1 Introduction

The RBC is in the unique position to be able to monitor and feedback local blood flow and oxygen (O_2) content as a result of navigating the complete circulatory system. In support of this, the ability of the RBC to release adenosine triphosphate (ATP) in response to physiological stimuli and, in turn, the ability of ATP to elicit a vascular response that results in an altered blood flow, has been demonstrated [36–39, 130].

However, the highly efficient adaptation of the RBC to contain large quantities of haemoglobin comes at the cost of the ATP producing organelle, mitochondria. Since ATP is a vital currency in many cellular processes, not just as a signalling molecule, the RBC must be able to synthesise it by other anaerobic means. Glycolysis is the metabolic process by which glucose is anaerobically converted to pyruvate or lactate in RBCs. The Embden-Meyerhof pathway details how a net gain of two moles of ATP are produced for every mole of glucose converted through the glycolysis process [131]. Recent measurements of intracellular ATP suggest RBCs can contain as much as 3.50 ± 0.09 mM ATP [132].

5.1.1 Stimuli and signalling pathways

ATP release from the RBC has been demonstrated as a consequence of several physiological stimuli, including low O_2 [37], acidosis [36], haemolytic index [38], and mechanical stimulation. For the latter, Sprague *et al.* [39] was first to demonstrate the ability of human RBCs to release ATP in response to mechanical stimulation in the form of a deformation, by passing RBCs through filter paper with a similar pore size to that of the RBC diameter.

Whilst there is agreement within the literature that the human RBC is a source of ATP, much debate remains around the mechanism by which ATP is transported

across the cell membrane to the extracellular space. Provided explanations are only supported in the event of one or two stimuli, suggesting that transport could be a stimuli-dependent pathway. Due to the inability of the RBC membrane to vesiculate, proposed methods focus on channel or transporter pathways, as shown in Figure 5.1.

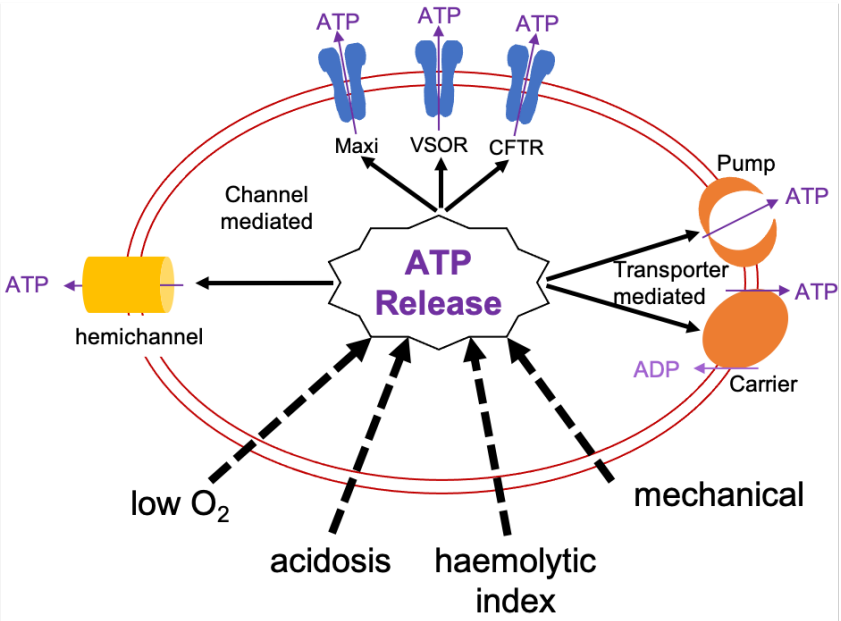

Figure 5.1: ***Proposed pathways for stimulated ATP release from the RBC.*** *Schematic detailing the stimuli and proposed non-lytic and non-vesicular pathways for ATP release from the RBC. Pathways include both transporter and channel mediated suggestions, with the CFTR protein being favourably implicated in mechanically stimulated ATP release. Adapted from [133].*

In the case of mechanically stimulated ATP release, the cystic fibrosis transmembrane conductance regulator (CFTR) protein is thought to be a principal component of the signalling pathway. It has been observed that extracellular ATP above basal level is negated when CFTR activity is inhibited by both sulfonylurea glibenclamide and genetic abnormalities (such as in the RBCs of cystic fibrosis patients) [44]. The work of Braunstein et al. [134] suggested that CFTR was not the primary exit channel for ATP, instead its role is to regulate the release of ATP through another channel. Further, Forsyth *et al.* [61] proposed this channel to be the pannexin 1 hemichannel that has also been implicated in mechanically stimulated ATP release from the RBC.

In support of a secretion pathway involving CFTR, Gov and Safran [135] hypothesised that deformation of the cell disassociates the spectrin network from actin filaments

within the membrane. This would free actin binding sites for attachment to, and hence activation of, the CFTR protein. Experimental support of this theory was delivered by Wan *et al.* [127] who demonstrated two separate time frames, activation and release, in the context of mechanically stimulated ATP release. The activation time-frame, $\sim$ 3 - 6 ms, corresponded to the reorganisation of spectrin and exposure of actin sites for CFTR binding. Whilst the release time frame, $\sim$ 25 - 75 ms, correlated well with the time required for CFTR to diffuse towards and bind with the actin, $\sim$ 30 - 70 ms.

5.1.2 Vasodilatory effect of ATP release

The ability of the RBC to release ATP is important due to the vasodilatory effect of ATP. Vasodilation occurs after ATP concentration in the extracellular space has increased. Extracellular ATP is free to bind with P2Y receptors that line the endothelial cells. These receptors are a subclass of purinergic ion channels, specifically the class of P2 receptors that are activated by ATP and ADP [136]. Upon activation the receptors will regulate ion exchange and transmembrane potentials and in the case of activation by ATP, stimulate the release of nitric oxide (NO) [130].

NO is a potent and well known vasodilator, responsible for the activation of soluble guanylate cyclase (sGC) [137, 138] within smooth muscle cells (SMC). It is this activation that initiates the SMC relaxation response and hence, conducted dilation of the blood vessel. Interestingly, it appears that NO also serves as a regulatory feedback mechanism for extracellular ATP concentration [40].

5.1.3 Regulating local blood flow

Able to release ATP upon stimulation and the subsequent role of ATP in vasodilation, places the RBC as a prime candidate in the discussion of a mechanism to regulate local control of blood flow in the microcirculation. At this level of the circulatory system blood flow is not stable, but much more dynamic, matching supply to constantly changing O_2 need.

Indeed in 1914, Barcroft [139] hypothesised that there must be such a mechanism by which a "*call for oxygen elicits a response*". In early research on this topic, Krogh [140] theorised that the response must include an increase in the diffusion surface which occurs by increasing the capillary density in skeletal muscle. However, his

work was unable to elucidate the mechanism by which such a response would have been mediated and was later proved inaccurate, as resting skeletal muscle was shown not to contain any such reserve of unused capillaries [141].

The RBC was first implicated as a vital component of this proposed control mechanism by Stein and Ellsworth [142]. Their research demonstrated that blood supply was more influenced by O_2 content of the blood - specifically, of the RBC - than the diffusion of O_2 into surrounding tissue (O_2 tension). This result lead to a move away from the notion that the RBC simply be a passive O_2 carrier. The aforementioned stimulated ATP release from RBCs further supports the theory that the RBC can regulate local blood flow.

Disease states

Abnormalities in any regulatory system can be expected to arise in diseased states. In the specific case of the RBC acting as a local blood flow mediator, diseases which are known to impact the circulatory system are of particular interest. An understanding of the changes that occur within the RBC in these diseased states, and the impact the changes have on the ability of the RBC to release ATP, would have major physiological consequences that could lead to improved therapeutic approaches to alleviate symptoms. The following diseases are discussed in detail in Section 1.4.

RBCs from both diabetic (type 2) and cystic fibrosis (CF) patients have been associated with reduced ability to release ATP, although circumstances vary between the two. Many of the secondary complications in diabetic patients are a result of impaired microvascular function as RBCs become glycated and oxidised. Not only does this impact the mechanical properties of the cells (see Chapter 4), but parallel to this diabetic RBCs exhibit a marked decrease in their ability to release ATP after mechanical stimulation [43].

CF patients lack a functional cystic fibrosis transmembrane conductance regulator (CFTR) protein, which usually resides in the RBC plasma membrane. When subjected to mechanical deformation, RBCs from CF patients have been shown to release less ATP than healthy control RBCs [44]. However, in contrast to the RBCs of diabetic patients the deformability of the human CF RBC was unchanged. This lead to the conclusion that the CFTR protein is likely to be involved in the signalling pathway for ATP release via mechanical stimulation.

5.1.4 Membrane structural integrity after dimethyl sulphoxide insult

Measuring extracellular ATP concentration also provides a novel way to investigate the integrity of the membrane upon insult with physiological concentrations of DMSO. Many of the biological and pharmacological uses of DMSO, described in detail in Section 3.1.3, are accepted with little experimental justification. The use of DMSO in enhancing solute penetration, cellular fusion or differentiation, or as a protectant alludes to the exploitation of structural disruption to the cellular membrane. DMSO is used in a wide range of concentrations, from as low as 2 vol-% [80] in the case of cellular differentiation, up to $> 60\%$ when used as a penetration enhancer [79].

So far, the most compelling experimental arguments in support of membrane disruption have come from molecular dynamics simulations. Pore formation as a result of DMSO treatment to DPPC bilayers has been demonstrated by both Notman *et al.* [86] and Gurtovenko and Anwar [87]. The former study suggested that pore formation, mirrored by an increase in membrane flexibility, would facilitate the permeability of the membrane to larger and/or charged molecules. Therefore providing justification for the use of DMSO as a penetration enhancer. The later study suggested DMSO action occurs across three concentration dependent modes (for detail see Section 3.1.3): firstly through decreasing bilayer thickness, secondly by inducing membrane pore formation and finally by destroying the membrane structural integrity completely. Moreover, increased secretion after DMSO treatment has been demonstrated experimentally, as in the case of neurotransmitters released from cells treated with low ($< 1\%$) concentrations of DMSO [143].

In the present work, the use of a luciferin-based assay to determine extracellular ATP concentration helps elucidate the effect of DMSO on cell membranes. In a comparison between non-treated and DMSO-treated blood samples, any increase in extracellular ATP after treatment would allude to cellular leakage and potential disruption of the membrane.

5.1.5 Chapter outline

This chapter details the effect(s) of different oxidising agents on the ability of the RBC to release ATP after mechanical stimulation. Since the membrane elasticity governs how well a cell can respond to external mechanical deformation, it becomes a vital area of investigation. By using the oxidising agents to selectively alter the

membrane structural components and hence, their associated elastic moduli (as outlined in chapter 4), the contribution of each elastic parameter in the mechanically stimulated ATP release can be probed. The discussion elucidates any relationship between specifically altered mechanical properties of the cell and ATP release, but also demonstrates that the essence of this proposed flow control mechanism may be much more complex. Secondly, RBCs were incubated with DMSO to establish if the structural integrity of the cell membrane was compromised by DMSO, a problem not previously addressed in full detail.

5.2 Experimental methods

For the experiments presented in this chapter, the methodology has been outlined in full in Chapter 2. The following section details more specific steps taken in the case of each chemical treatment.

5.2.1 Chemical treatment preparation

Oxidants

Blood samples were aliquoted into 1 mL vials for treatment and measurement purposes. For the oxidising chemicals (hydrogen peroxide (H_2O_2), cumene hydroperoxide (cumOOH), and diamide) stock solutions were first diluted to an intermediate concentration in a PBS/BSA buffer. This ensured that samples were not excessively diluted, so as not to affect the viscosity and therefore the applied shear stress during the shearing process.

An intermediate concentration, $c_i = 19.56$ mM, of H_2O_2 (Fisher Bioreagents, Belgium) was prepared the morning of the experiment, from which the 1 mL blood aliquots could be diluted to the desired concentration (100 - 500 μM) with a volume not exceeding 25.55 μL. Samples were incubated for 30 minutes before measurement.

The intermediate concentration of cumOOH (Sigma-Aldrich, USA) was 2 mM, prepared the day before the experiment. From this, the individual 1 mL blood samples could be diluted to between 10 - 100 μL with a volume not exceeding 50 μL. Samples were incubated for 20 minutes before measurement. The reduced incubation time for cumOOH treatment was a direct result of observation within the fluctuation experiments. The results obtained from TFS indicated cumOOH had a much faster

mechanism of action on the cell. Therefore the incubation time was reduced accordingly to avoid excessively damaged cells introducing anomalies into the data.

Stock diamide (Sigma-Aldrich, USA) was diluted to 0.2 M and prepared the day before the experiment. Blood samples were then diluted with a volume up to 50 μL, creating concentrations in the range 1 - 10 mM, 30 minutes before measurement.

Dimethyl sulphoxide

Since samples treated with dimethyl sulphoxide (DMSO; >98%, Sigma-Aldrich, USA) were only measured pre-shear, the sample viscosity became an obsolete parameter. Therefore, blood was diluted directly with stock DMSO in 1 mL vials. Treatment concentrations ranged from 1 - 10 vol-%, where the maximum addition of DMSO to the sample was still only 100 μL. Samples were incubated with DMSO for 30 minutes before measurement.

5.2.2 Effect of chemicals on assay

Two methods were used to establish if any of the four chemicals impacted the luciferin-based assay, used to determine sample ATP concentration. In the first method (M1), an ATP calibration curve was measured using pure ATP standards and those doped with an intermediate concentration of each chemical. This method, used for H_2O_2 and DMSO, tested both the effect of the chemicals on the assay and their interaction with ATP. The second method (M2) compared buffer background measurements (a small concentration of ATP was present in the buffer) to that of the same buffer diluted with an intermediate concentration of the chemical. In this case, it was assumed that any discrepancy between the results would be due to the chemical affecting the assay. This method was used for cumOOH and diamide.

Results of these tests are shown in Figure 5.2. Comparison using M1 are displayed on the left and comparisons made using M2 are displayed on the right, in both cases error bars denote the standard deviation. All comparisons were further subjected to a T-test with confidence level of $p = 0.05$. All samples returned statistically insignificant differences, except the comparison between the ATP sample at c(ATP) = 10^{-10} M and that treated with both H_2O_2 and DMSO (made using M1).

The significant T-test result for comparisons based on the c(ATP) = 10^{-10} M standard could be influenced by inaccuracies in the dilution series used. The provided ATP

standard of c(ATP) = 10^{-7} M was 4-fold diluted to obtain this concentration, whereas the c(ATP) = 10^{-8} M standard was only diluted once and therefore should be more accurate. At this concentration, the test provided an insignificant T-test result for both chemicals. Further, no experimental values were as low as 10^{-10} M. These results, particularly for diamide, are supported by several publications that report no affect from diamide on the luciferin-based assay [144, 145].

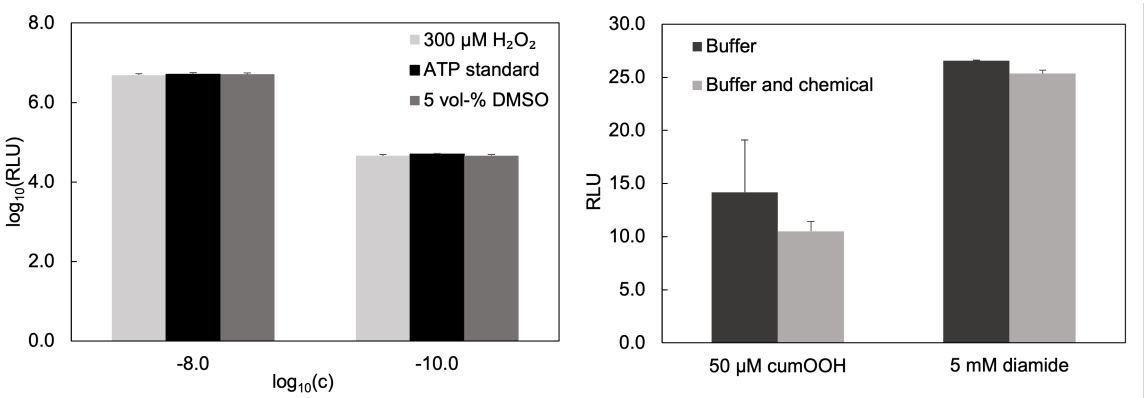

Figure 5.2: ***Effect of chemical treatments on the luciferin-based assay.*** *The effect of each chemical on the chemiluminescent assay used to measure ATP concentration is presented here. Method 1 (M1, left) was used to check H_2O_2 and DMSO treatment, whilst method 2 (M2, right) was used to check cumOOH and diamide treatment. Further T-tests revealed that treatments caused no significant differences of concern.*

5.3 Results

5.3.1 Oxidative modification using hydrogen peroxide

The effect of H_2O_2 on ATP release from RBCs subjected to a physiological shear stress for 30 seconds is presented in Figure 5.3, where error bars denote the standard error. As with many of the results presented in this chapter, the size of the error bars suggests a large variability in the measurements. Although several repeat measurements were taken to account for this, the variability was to be expected as has been reported in several previous studies, both between samples from different individuals and between samples from the same individual taken on different days [144, 145].

The untreated sample, c(H_2O_2) = 0, released 0.55 ± 0.21 nM of ATP. Whilst there could be a slight trend towards increased ATP release after treatment with H_2O_2, overall there were no large differences when compared to the untreated sample.

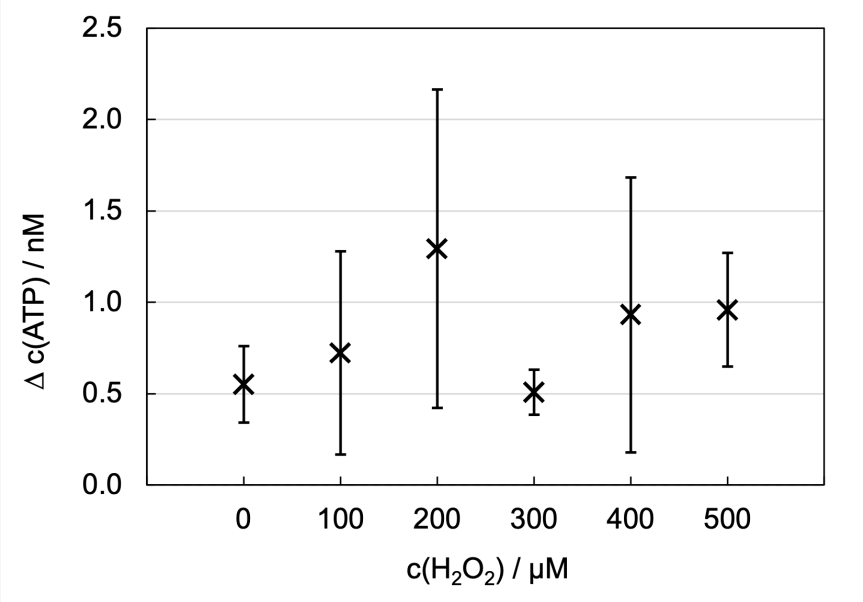

Figure 5.3: ***Effect of H_2O_2 on mechanically stimulated ATP release.*** *Error bars denote the standard error. Due to large uncertainty within the results, H_2O_2 treatment appeared to have little effect on mechanically stimulated ATP release from the RBCs.*

5.3.2 Oxidative modification using cumene hydroperoxide

Figure 5.4 details the change in extracellular ATP concentration, as a result of the increased mechanical stress during shearing, in samples treated with various concentrations of cumOOH. Error bars denote the standard error. The data from Sample 1 produced large uncertainty masking any trends that could potentially be present, this indicated the need for a repeat measurement. Sample 2 data produced much smaller uncertainties. Here, the untreated sample released 1.84 ± 0.62 nM of ATP, with a similar amount also released when the concentration of cumOOH was initially increased to 10 µM. Whilst blood treated with higher concentrations of cumOOH appeared to release less ATP, there was still no significant difference with the untreated sample.

5.3.3 Oxidative modification using diamide

The change in extracellular ATP concentration, as a result of increased mechanical stress during the shearing process, in samples treated with various concentrations of diamide is shown in Figure 5.5. Error bars denote the standard error. The untreated sample released 4.57 ± 0.78 nM of ATP during the shearing process. Increasing

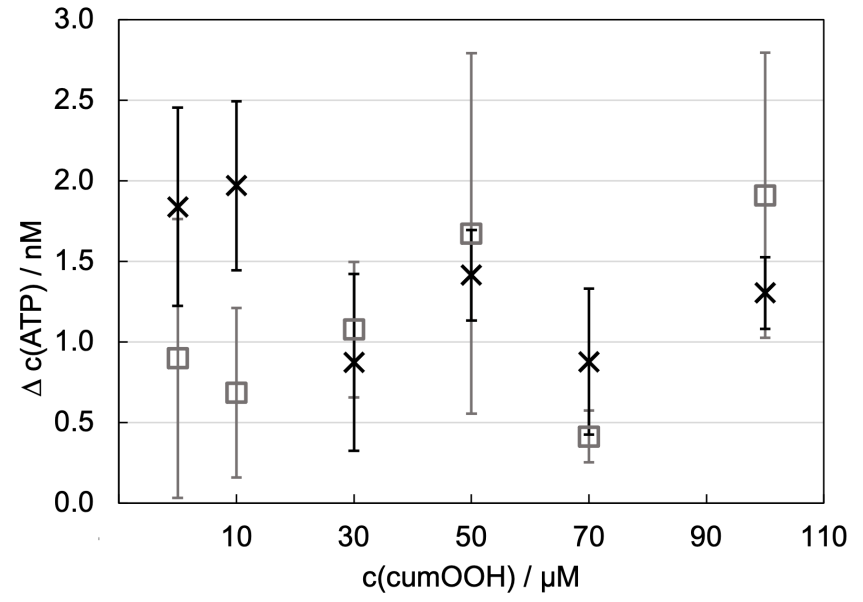

Figure 5.4: ***Effect of cumOOH on mechanically stimulated ATP release.*** *Two samples are presented, sample 1 (□) and sample 2 (×), with the error bars denoting the standard error. Whilst the experimental uncertainty obtained from sample 2 was smaller than that of sample 1, there were still no significant differences in mechanically stimulated ATP release after the blood was treated with cumOOH.*

the concentration of diamide reduced the amount of shear-induced ATP release by a significant amount, to around 0.5 nM.

Of note with these results is the larger ATP release for the c(diamide) = 0 mM sample, when compared to that from the experiments involving the other two oxidising treatments. It could be interpreted that this would provide a "false-positive" as to the effect of diamide on ATP release, however this isn't believed to be the case. The sample clearly contains a larger than average background or reserve of ATP, which could result from a change in the physiological state of the donor, or an unaccounted for event during sample preparation. However, this would have equally affected all samples in the experiment, since all samples were aliquoted from the same blood sample into buffer aliquoted from the same stock solution. In this case the error introduced would be systematic, indicating that the trend - reduced ATP release after diamide treatment - is still significant.

5.3.4 Chemical modification with dimethyl sulphoxide

Figure 5.6 details the ATP released from each sample after incubation with DMSO, where error bars denote one standard deviation. These results indicate that even

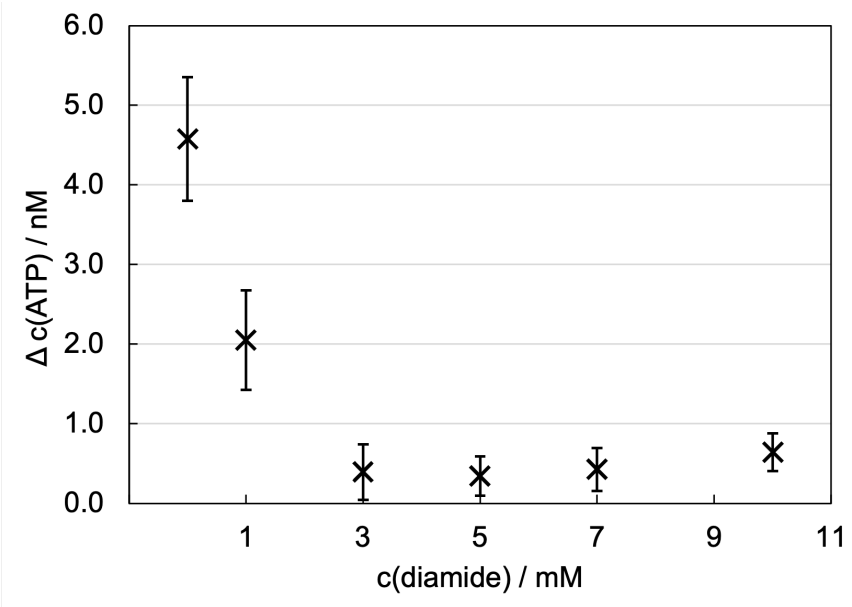

Figure 5.5: ***Effect of diamide on mechanically stimulated ATP release.*** *Error bars denote the standard error. Diamide treatment appeared to significantly impact the ability of the RBC to release ATP upon mechanical stimulation.*

after incubation with the smallest concentration of DMSO, 1 vol-%, the membrane was rendered significantly permeable to ATP, followed by a DMSO dependent increase in ATP leakage. A plateau in extracellular ATP concentration was reached around the 5 vol-% treatment, at c(ATP) $\approx$ 400 nM.

5.4 Discussion

Using a microfluidic approach to measure ATP release from RBCs as a result of mechanical stimulation has proven successful in previous studies investigating the dynamics of shear-induced ATP release from RBCs [127]. The method allows for easy and precise control over the duration and magnitude of increased mechanical stress that the sample was subjected to, as well as ease of measurement using the luciferin based assay. Preliminary experiments with pure blood samples justified the use of 1 %-Htc blood samples and further, the different chemical treatments were shown not to affect the assay. It was anticipated that the selective altering of the RBC membrane structural components with each of the oxidative chemicals would provide a clear link between targeted altered deformability and ATP release. However, the results obtained appear to demonstrate a much more complex cell response involving not just the structural components.

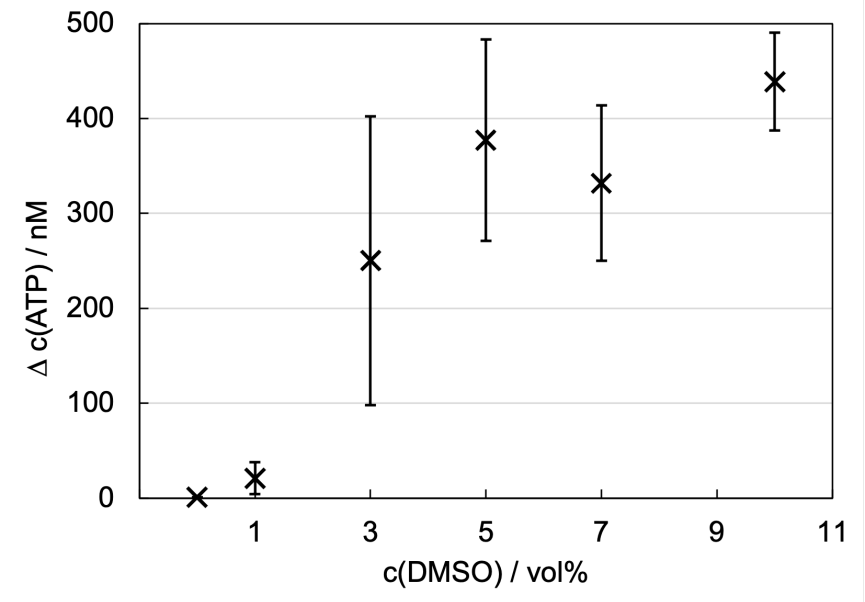

Figure 5.6: ***DMSO-induced ATP leakage from the RBC.*** *Error bars denote one standard deviation. Upon insult with DMSO, even at the lowest of concentrations, the RBC membrane becomes significantly permeable to ATP. A plateau in Δ c(ATP) was reached around the 5 vol-% DMSO treatment.*

5.4.1 Comparison to changes in mechanical properties

Hydrogen peroxide

The TFS measurements demonstrated that H_2O_2 predominantly and significantly increased the shear modulus, with only a slight increase in the bending modulus observable at higher concentrations. Taken alongside the results presented in this chapter, this suggests that artificially stiffening the cytoskeleton with H_2O_2 does not lead to suppression of mechanically stimulated ATP release from the RBC. This result seemingly contradicts the hypothesis that an increased shear modulus leads to reduced ATP release, as can be extrapolated from the individual works on diabetic RBCs to assess their mechanical properties [26] and ability to release ATP [43]. The results of the study presented here suggest that the target of H_2O_2 oxidation, namely the haemoglobin and its oxidised form's subsequent binding to and stiffening of the spectrin cytoskeleton, does not negatively disrupt the signalling pathway between the mechanical stimuli and release of ATP. Instead, the binding of the oxidised haemoglobin to the spectrin must occur in such a way that does not impact the pathway, suggesting another modification within diabetic cells (perhaps oxidation of GSH) to be responsible for the decrease in ATP release.

Cumene hydroperoxide

CumOOH affects both of the elastic moduli in a step-like manner. There is very little effect on the cell's mechanical properties if cumOOH treatment is less concentrated, which provides some explanation for the similar concentration of ATP released for the untreated and 10 μM samples (figure 5.4). For the more concentrated treatments which are known to increase the bending and shear moduli, there appeared a corresponding reduction in ATP release although large experimental uncertainty renders this insignificant. Taken alongside the results from H_2O_2 treatment in which no effect on the ATP release was observed, this finding suggests that when considering the mechanisms of mechanically stimulated ATP release, the importance of a cell having an unperturbed bending modulus may dominate the need for a physiological shear modulus.

Diamide

Treatment with diamide further supports the idea that the bending modulus is the more influential factor in determining deformation induced ATP release from RBCs. Whilst the shear modulus is significantly altered, as in the case of H_2O_2 or cumOOH treatments, diamide induces a comparatively large increase in the bending modulus and is mirrored by a large, concentration dependent decrease in ATP release after mechanical stimulation. It would appear that the cross-linking of transmembrane integral proteins contributes greatly to the increased bending modulus and decreased ATP release after mechanical stimulation.

Summary

To provide a visual overview of ATP release in comparison to the change in RBC mechanical properties, the data from both the TFS and ATP studies have been presented in Figure 5.7 for all three oxidative treatments. For all three parameters, the values presented are relative to the values obtained from measurements of untreated blood samples in both the TFS and ATP release experiments. Where data is red in colour, this indicates that more ATP has been released upon mechanical stimulation; whereas blue data indicates the opposite, that less ATP has been released. The grouping of darker points to the high end of the κ/κ_0 and μ/μ_0 scales indicates that increasing the elastic parameters of the cell has some effect on the amount of ATP

release stimulated by mechanical stress. However, the large spread within the data suggests that this effect could be far more complicated than anticipated.

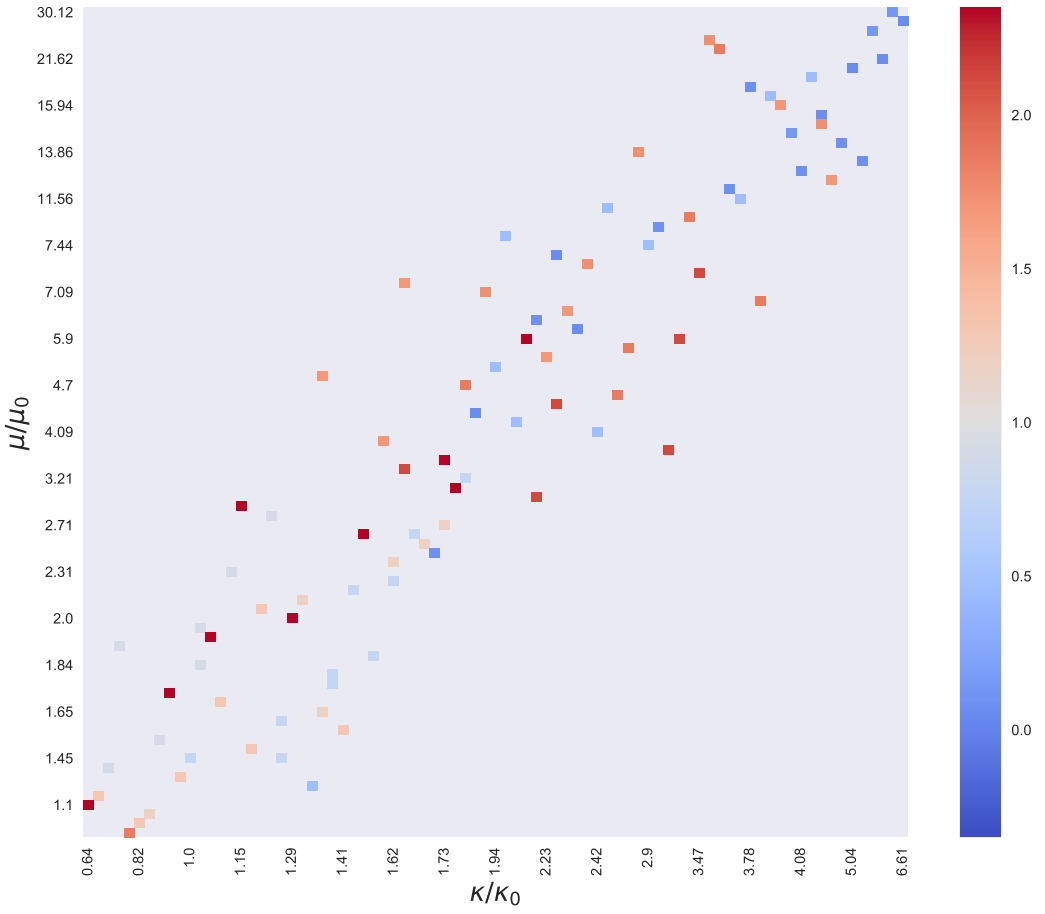

Figure 5.7: ***Comparison of mechanically stimulated ATP release and change in elastic moduli.*** *Change in ATP release is presented as a function of both elastic parameters (bending, κ, and shear, μ) of the RBC membrane. Values presented are the change in parameter relative to the untreated blood sample, i.e. a value of 1 indicates no change.*

5.4.2 Effect of oxidisation

Examining the results in a stand-alone capacity, away from simultaneous changes in mechanical properties, demonstrates a much more complex idea. If instead the targeted sites of oxidisation and the role these play in the proposed signalling pathway (between stimulation and release of ATP) are scrutinised, a much more detailed explanation is obtained.

Hydrogen peroxide

ATP released upon mechanical stimulation appears largely independent from concentration of H_2O_2. The oxidisation of haemoglobin produces irreversible hemichromes (iHCRs) which initiate a more complex attack on membrane proteins, resulting in the destabilisation of the spectrin - protein 4.1 - actin complex [146]. These results (Figure 5.3) suggest that with actin then disassociated from the main spectrin cytoskeleton, it is more readily available to bind with the CFTR protein. As outlined in Section 5.1.1, this would activate the mechanotransductive pathway for ATP release from the RBC and as a result, the ATP released upon mechanical deformation of the cell remained largely unaffected after H_2O_2 treatment in the experiment presented here.

Cumene hydroperoxide

In contrast, CumOOH appears to have a weak effect on the mechanically stimulated release of ATP from RBCs, reducing sample ATP at concentrations of cumOOH above 10 µM. This reduction may not be significant because the effect of oxidation on the lipid bilayer and cytoskeleton are combative in nature, with one cancelling out the other. For example, if the haemoglobin is collaterally damaged during cumOOH oxidation of the cell it will bind to spectrin which, in turn, exposes more actin to the CFTR protein as observed in treatment with H_2O_2. Counter productively, the oxidative effect of cumOOH on the membrane phospholipids would increase the lipid packing, thus reducing membrane fluidity [147] and increasing protein lateral diffusion time [148]. This indicates that the CFTR protein will not be as readily able to diffuse towards and thus bind with exposed actin filaments to stimulate the ATP signalling pathway. This results in the decreased ATP release upon mechanical stimulation. Since cumOOH treatment results in a slight decrease in ATP release overall, this is further suggestive that oxidisation targeting the lipid bilayer has a greater effect than oxidisation of the cytoskeleton on deformation-induced ATP release from RBCs.

Diamide

The effect of diamide treatment on ATP release has been documented in the literature, where diamide is usually the artificial stiffening agent of choice to investigate mechanically stimulated ATP release. It has been used by Price *et al.* [144, 145] and

Wan *et al.* [127], all demonstrating a reduced ability of RBCs to release ATP upon mechanical deformation after treatment with diamide.

Diamide is known to directly affect cytoskeletal spectrin and reduce spectrin - actin binding mediated by protein 4.1 [100]. However, if this were the only effect it would be assumed that the system would respond in a similar manner to when treated with H_2O_2; the ATP release would remain unchanged or trend towards an increase after treatment, as more actin becomes available to bind with CFTR. With a significant reduction in ATP release apparent after diamide treatment, it is likely that other structural components of the membrane have also been targeted. More specifically, diamide has an affinity for the thiol groups of the cysteine amino acid. Therefore it must be considered which other membrane proteins contain potentially susceptible cysteines in their amino acid sequences.

Spangenberg *et al.* [149] demonstrated that upon treatment with diamide, platelet actin undergoes oxidation resulting in the formation of disulphide cross-linking. Further, it is known that the cytoskeletons of sickle cells are markedly less deformable than healthy cytoskeletons, and that disulphide cross-linking of cysteines within the actin filaments is a contributing factor of this [150]. Disulphide cross-linking of actin is supported in several further studies [151, 152]. This suggests that the direct oxidisation of actin by diamide reduces its ability to bind with the CFTR protein and initiate the ATP release signalling pathway.

It is further known that diamide induces oxidisation of glutathione (GSH) [129] initiating formation of a disulphide bond between GSH and a cysteine on CFTR [153], and that these bridges significantly impair the functionality of CFTR. Not only would this inhibit the binding of actin and CFTR, but GSH is a known antioxidant that removes lipid peroxides [110]. The oxidisation of GSH would therefore leave bilayer lipids open to such an attack as described in the case of cumOOH peroxidation. In support of this, the oxidation of GSH has previously been linked to reduced ATP release from diabetic RBCs and healthy RBCs treated with diamide [154]. The fact that the diffusion time of CFTR remains relatively unaffected under diamide treatment [35, 127] suggests that the cross-linking of CFTR has more of an effect on ATP release than the direct oxidation of bilayer lipids. Not only does this provide an explanation as to the majorly reduced ATP release shown in Figure 5.5, but also could also explain why diamide has a much larger effect than cumOOH.

The bond between actin and CFTR could further be inhibited by membrane shape changes induced by diamide treatment. As previously mentioned in Chapter 4, Sinha

et al. [113] demonstrated the echinocytic nature of cells after being treated with high concentrations of diamide. This morphology could increase the lateral diffusion distance between CFTR and the nearest actin molecule. In turn, this would lead to local disassociation between the cytoskeleton and bilayer and remove the ability of CFTR to bind with actin altogether.

5.4.3 Permeability enhancing dimethyl sulphoxide

The permeability enhancing property of DMSO has been expounded through quantifying the extracellular ATP before and after treatment with DMSO at varying concentrations, presented here. The results demonstrate that the RBC membrane becomes significantly permeable to ATP upon insult with DMSO, appearing fully permeable as DMSO concentration is increased above 5 vol-%. Since the cells were not subjected to an external mechanical stimuli, it is fully possible that the mechanism by which ATP was released from the cell here differs greatly from that described in treatments involving the oxidants (see Section 5.4.2).

Of course, DMSO could directly affect one or more of the proteins involved in the signal transduction pathway described in Section 5.1.1, leading to improper functioning and thus, ATP leakage. This is not implausible, since ATP transport across the membrane is increasingly thought to be regulated, but it remains unclear what the specific effect of DMSO would be. In support of this, it has previously been shown that low concentrations of DMSO, similar to those tested here, can change protein secondary structure from α-helical to β-sheet [155]. Affecting one or more of the signalling pathway proteins in this manner could therefore facilitate ATP release.

However, it remains that haemolysis is still the preferred explanation for DMSO induced ATP release from RBCs [156, 157]. The cell undergoing haemolysis suggests that DMSO disrupts the structural integrity of the lipid bilayer. Evidence of this has previously been demonstrated through increased membrane permeability or thinning, and the suggestion of pore formation (see Section 5.1.4). Structural abnormalities or faults such as these would provide a compelling explanation as to the severity of ATP release after DMSO treatment demonstrated here.

Regardless of the mechanism of release these results raise important questions in the justification of the solvent's physiological uses. Assuming increased permeability to ATP can be generalised to other cell types, and considering that a number of cellular processes are ATP dependent, cell functionality could be significantly impaired upon

DMSO treatment. This is particularly important considering that at 10 vol-% DMSO is used in the cryopreservation of cord blood [84] - a vital therapeutic aid in the treatment of several genetic and inherited disorders.

5.5 Conclusions

These results demonstrate that mechanically stimulated ATP release is affected by oxidatively modifying the RBC membrane. The degree of change in ATP release correlates with the target site of oxidisation. H_2O_2 oxidises the haemoglobin which in turn, affects the mechanics of the cytoskeleton but has relatively little impact on the amount of ATP released as a result of mechanical stimulation. CumOOH oxidation primarily targets the lipid bilayer whilst inadvertently also modifying the RBC cytoskeleton. At higher concentrations, cumOOH can reduce ATP release after mechanical deformation. Considered an all-round stiffening agent, diamide oxidisation targets both cytoskeletal and integral membrane proteins, cross-linking available thiol groups of the cysteine amino acid. In turn, diamide treatment has a marked impact on the amount of ATP released after mechanical stimulation, dramatically reducing the RBCs ability to do so.

The chemical alteration of the lipid bilayer has more of an effect on ATP released from the RBC after mechanical stimulation and as such, suggests that the signalling pathway between stimulation and ATP secretion primarily resides within the lipid bilayer domain. The degree to which each oxidative agent affects either the bending or shear moduli suggests that the bending modulus may be the more important factor in controlling ATP release under mechanical deformation. Relating this to the biological process of ATP release, this suggests that the ability of the CFTR protein to migrate within the lipid bilayer and its availability to bind with other proteins, has a greater effect on mechanically stimulated ATP release than the availability of actin sites to bind to CFTR to initiate the signalling pathway. This further indicates that the presence of the CFTR protein is a major determinant in mechanically stimulated ATP release.

DMSO treatment of the RBC results in extensive ATP loss from within the cell, even in the absence of mechanical stimulation. The effect that DMSO has on the cell and hence the cause of this leakage, is largely disputed within the literature. Suggestions range from DMSO altering one or more of the proteins involved in the signalling pathway, to DMSO affecting the structural integrity of the lipid bilayer.

Whatever the mechanism is, it remains an important question within the biological field. That said, these results do provide headway into further understanding the effect that DMSO treatment has on the RBC and justification of its various uses.

6 Conclusions and further work

6.1 Conclusions

This thesis probes the physiological state of the RBC at both the molecular and whole cell level. Perturbations as a result of oxidative damage are quantified in terms of the elasto-mechanical properties of the cell, and these are paralleled with ability of the RBC to release the signalling molecule adenosine triphosphate (ATP) under increased mechanical deformation. Additionally, the effects of dimethyl sulphoxide (DMSO) treatment were investigated throughout the work, seeking to further evidence the solvent's action on the RBC.

Not only is the RBC abundant and easy to obtain, it is also relatively simple in structure making it an attractive entity for investigation. The large volume of oxygen carrying haemoglobin is enclosed by a semipermeable membrane barrier, structurally consisting of the plasma membrane and protein cytoskeleton. This composite structure endows the membrane with both a bending and shear rigidity, allowing the cell to undergo large deformations in the circulation without compromising its structural integrity. These mechanical properties have been investigated through a number of different approaches, but these are often limited by use of whole blood samples or the length scales of the chosen measurement, leading to poor reproducibility and discrepancies in obtained values, as well as method-dependant empirical elastic parameters. Moreover, it is imperative to be able to establish the mechanical properties of the RBC due to their possible implication as stimuli of signalling pathways, such as that which results in the release of the vasodilator, ATP. Work in this area has strong but poorly understood clinical relevance.

Here, synchrotron x-ray studies, thermal fluctuation spectroscopy (TFS) and shear-flow chemiluminescence analysis were utilised to satisfy the aims of the project. Initially, the structure of the phospholipid bilayer was investigated using Langmuir monolayers akin to each leaflet of the RBC membrane bilayer. The monolayers were probed with intense x-ray radiation in both the grazing incidence x-ray diffraction (GIXD) and grazing incidence x-ray off-specular scattering (GIXOS) geometries,

providing both the lateral ordering and transverse structure of the monolayers respectively. Further, the GIXOS technique was compared to x-ray reflectivity (XRR), providing proof of concept of the newly established GIXOS technique.

Whilst the two monolayers both exhibited a hexagonal packing structure, it was evident that variations in population size of each phospholipid species contributed to distinct parameters of the lattice packing between the monolayers. Furthermore, the IL monolayer exhibited a greater range over which the crystalline order was present. Moreover, the difference in electron density profiles of the two monolayers supported the notion of varying packing arrangements. Regrettably, analysis of the XRR measurements returned large experimental uncertainties impeding meaningful comparison to the overall GIXOS results. Nevertheless, this suggests GIXOS as the more reliable technique further increasing the desirability of its use over XRR.

In the second stage of the project, the mechanical properties of the cell were quantified using TFS, a method capable of probing the mechanical state of single cells. This method allowed for continual cell analysis, meaning that as the same cell was measured both before and after chemical modification, a change in elastic moduli relative to the physiological state could be presented. Further, this method measures fluctuations of the cell in both the long and short length scale regimes, therefore allowing simultaneous measurement of the bending and shear moduli of the cell.

As changes in the bending or shear moduli are a result of alterations to either the lipid bilayer or cytoskeleton respectively, the target of each of the oxidants could be established. Whilst hydrogen peroxide (H_2O_2) demonstrated an affinity for the cytoskeleton and cumene hydroperoxide (cumOOH) preferentially partitioned into the lipid bilayer, the action of diamide appeared non-specific. In all cases, results agreed well with previous literature and set the foundation for exploring the association between RBC mechanical properties and the cell's ability to release ATP under increased mechanical deformation.

To that effect, a novel method for examining the increase of mechanical stress as a stimuli for ATP release from the RBC was designed. The simple shear apparatus consisted of a syringe pump attached to a narrow cannula tubing, mimicking the environment within the circulatory system. Magnitude and duration of the increased shear stress could be easily controlled, although an increased buffer viscosity was required due to limitations with the experimental apparatus. Once sheared, sample ATP concentration was measured with the commonly used luciferin based chemiluminescence assay.

The data showed oxidative modification to the RBC membrane impacted mechanically stimulated ATP release and further, that the target site of oxidation was associated with the degree of impact. A reduction in mechanically stimulated ATP release was attributed most strongly to an increase in bending modulus and hence, alteration of the lipid bilayer. However it appears that this is not a direct association, rather the oxidant works to target the structural elements of the membrane and the biological process within simultaneously.

The effect of DMSO on the RBC membrane has also been extensively investigated throughout this work, with results offering promising justification for the multi-uses of DMSO. Synchrotron studies suggested a strong reorientating effect on the phospholipids of a DMSO treated monolayer, with the possibility of monolayer division into DMSO rich/lipid poor and DMSO poor/lipid rich domains. This result offers a mechanism by which the molecular action of DMSO can enhance solute penetration across the membrane through the lipid poor domains effectively acting as pores. The effect of DMSO on the mechanical properties of the cell appears complex at first but despite this, recovery from insult with a physiologically relevant concentration was observed in the TFS study. This finding is of significant importance considering the use of DMSO in the cryopreservation of cells. Finally, the membrane became significantly permeable to ATP after treatment with even the lowest concentration of DMSO and importantly, this occurred without mechanical stimulation. Whilst it remains possible that DMSO could positively affect the ATP signalling pathway, a more compelling argument is that this result provides strong evidence of the pore forming molecular action of DMSO.

To outline, this work consolidates several different areas of investigation in respect to the RBC membrane. Langmuir monolayer studies of RBC phospholipids have progressed through the consideration of more complex mixtures of phospholipid species, akin to the RBC plasma membrane. Further, RBC membrane mechanics have been explored, through selective oxidisation of each of the structural components in correlation with the cell's ability to release ATP and stimulate vasodilation upon mechanical stimulation. The results suggest that changes in the mechanical properties and any mirrored effect on ATP release from the RBC may occur as a result of underlying biological processes that are yet to be fully understood.

6.2 Future work

6.2.1 Investigate oxidative stress using synchrotron techniques

The effect of oxidative stress on the ordering and electron density profiles of RBC plasma membrane phospholipids could be investigated using synchrotron x-ray radiation techniques. As a major target of lipid peroxidation is the cleavage of the double bond in the unsaturated acyl chains, a study such as this would require the use of native lipids that are more unsaturated than the dipalmitoyl chains of the lipids used in the studies presented here. Of course, unsaturated chains would decrease the lipid organisation in the plane of the air-subphase interface, consequently diminishing the intensity of any possible GIXD peaks. However, this would still act as a sensitive measure of peroxidation as any cleavage of the double bond would be thought to increase the lipid ordering and hence, result in a more notable GIXD pattern. The results of this thesis, particularly in Chapter 4, suggest cumOOH as a good candidate for a study of this nature due to its high affinity for oxidising the lipid bilayer. Both H_2O_2 and diamide could also be investigated, but more so above the concentrations where oxidation of the lipids within the plasma membrane was observed.

6.2.2 Use of RBC modelling to obtain mechanical parameters

A major disadvantage in the quantitative measurement of RBC mechanical parameters is the often large discrepancies in values obtained between the various techniques. The reasons for these discrepancies have previously been described, but one major theme that arises is the application of the theoretical approximation to the experimental setting. Particularly in the case of TFS the discoid shape of the cell is not fully accounted for. A solution to this problem could be the amalgamation of coarse-grained particle dynamic simulations with the experimental approach, as suggested by Hale *et al.* [101]. Here, the experimentally obtained mean square fluctuations could be matched to that of a simulated RBC, of which one has full control of the elasticity and shape.

6.2.3 Further investigate the role of the RBC in circulatory signalling

The supporting evidence demonstrating the RBC to be heavily involved in control of the physiological functioning of the circulatory system is an exciting prospect. Indeed,

the ability of the RBC to release ATP and stimulate vasodilation suggests that the RBC could potentially be involved in other circulatory control mechanisms. In view of this, the novel methods described within this thesis could be used to investigate the effect(s) of oxidative stress on the release of other signalling molecules, such as sphingosine-1-phosphate (S1P). This is of interest since it has been demonstrated that S1P, released from rat erythrocytes, maintains normal venial microvessel permeability [158].

6.2.4 Inclusion of complementary techniques

There is a plethora of biophysical techniques available that could provide complementary analysis of the role of the RBC membrane in the physiological functioning of the overall cell. These include but are not limited to fluorescence microscopy, Brewster angle microscopy (BAM), and ratiometric fluorescence imaging.

Fluorescence / Brewster angle microscopy on Langmuir Monolayers

Langmuir monolayers akin to the RBC plasma membrane could be investigated using fluorescence microscopy. This general-lab based technique is particularly useful for the observation of domain structures within the monolayer, and could therefore provide further evidence of the partitioning of the membrane into DMSO rich/lipid poor and DMSO poor/lipid rich domains. It involves spiking the phospholipid sample with rhodamine labelled lipids, such as Rh-DHPE, at a concentration of no more than 0.2 mol-%. However, due to the large size of the rhodamine moiety, these lipids preferentially partition into less ordered phases and therefore have the potential to be excluded towards the edges of the more densely packed DMSO poor/lipid rich phases.

BAM offers a desirable alternative to this, removing the need for the sample to be spiked whilst still allowing for observation of domain formation. In this method, p-polarised light is incident on the air-subphase interface at the Brewster angle, the angle at which no reflection will occur. If the interface is then perturbed by a phospholipid monolayer, reflection will occur from the domains where lipids are present. Whilst domain formation is expected in standard monolayers akin to the RBC plasma membrane, BAM could help elucidate changes to these domains under DMSO treatment.

Ratiometric fluorescence imaging of whole cells

Ratiometric fluorescence imaging is used as a sensitive measure of the membrane dipole potential. In order to obtain RBC images, RBCs are incubated with the fluorescent probes, such as di-8-ANEPPS. The probe is then excited at two wavelengths, 420 and 520 nm, and images of the resulting emission intensities are obtained. The ratiometric intensity, $R = {}^{I_{420}}/_{I_{520}}$, can then be calculated and converted into the approximate membrane dipole potential using a calibration equation. Using this method on RBCs treated with the oxidising agents (as in [122]) and in parallel to the ATP release studies, would extend the knowledge base presented in this thesis. Further, since this technique also provides information about lipid packing in whole cells, it would serve as another method for observing the molecular action of DMSO on the RBC.

6.2.5 Clinical use of established techniques

The clinical relevance of measuring RBC mechanical properties alongside ability to release ATP has been made apparent throughout this thesis. Most notably though, these results suggest that changes away from the physiological state of the RBC in certain diseases most likely result from more complex underlying biological processes. Since as yet, there is no clear link between altered mechanical properties and ability to release ATP in diseased states, the techniques described in this thesis are some way off use as diagnostic tools. However, as a more clinical extension to this work, these techniques could be used in a longitudinal study to monitor the progression of certain diseases and their impact on the RBC.

A Fluctuation spectra analysis code

```
#                       Curve plotting and Non-Linear Regression Analysis

# This script will first produce a PDF file plot of data from sq.txt
# Next it will fit the theoretical curve to the experimental data and output
# the values of the parameters of the fit, as well as a plot of the fit.

#       Load libraries
import numpy as np
from scipy.optimize import curve_fit
import matplotlib.pyplot as plt
import csv
from itertools import zip_longest
import os


#       Load data direct from sq.txt file
data = np.loadtxt('sq.txt')      #read in file
data2 = data.transpose()         #convert rows to columns and vise versa

# asign names to each row that is needed for analysis
old_n = data2[0]
old_logn = data2[10]
old_y2 = data2[12]
old_y1 = data2[13]

# Here is a list of rows that will be deleted (ie modes 1, 2 and > 20),
# note that the index starts at zero, so mode 1 is index 0 and so on
index = [0, 1, 17, 18, 19, 20, 21, 22, 23, 24, 25, 26, 27, 28, 29, 30, 31,
                        32, 33, 34, 35, 36, 37, 38, 39, 40, 41, 42, 43,
                        44, 45, 46, 47, 48, 49]
```

```
# Deleteing the above rows in the x and y data
n = np.delete(old_n, index)
logn = np.delete(old_logn, index)
y2 = np.delete(old_y2, index)
y1 = np.delete(old_y1, index)

# ------------------------------------------------------------------------
#                   Plot logarithmic fluctuation spectrum

# Here data is added to the plot as (x, y, 'black x') using the column titles set
# above
plt.plot(logn, y1, 'kx')

# Here the axis range and labels are added
plt.title('Cell6')    # Can change title
plt.xlabel('logn')
plt.ylabel('$<\delta_n^2>$')
#plt.xscale('log')

# Display the plot and save it to file
plt.tight_layout()              #prevents the graph being cropped in the pdf
plt.savefig('FlucSpec.pdf')     #Prints the plot to pdf
plt.show()                      #Prints the plot to screen
plt.close()                     #Closes pdf file

# ------------------------------------------------------------------------
#                   Fit Two-Parameter Equation

# Set variables and constants
xdata = n
ydata = y2
pi = 3.1415926535

# Function to fit (two-parameter equation)
def func(x, kappa, sigma):
     return (1.0 / (2.0 * pi * kappa)) * (1.0 / (np.sqrt(sigma + x**2.0))**3.0)
```

```
# Execute fit
# Initial guesses for Kappa and sigma are set in p0 = (kappa, sigma)
popt, pcov = curve_fit (func, xdata, ydata, p0=(150.0, 20.0))

# Printing outputs to the screen
print('-------------------------------------------------------------------------')
print('Output values of fitting the two parameter equation:')
print(' ')
print('[ kappa, sigma ] = ', popt)     #prints popt - contains the output values
                                                    #of kappa and sigma
print(' ')

# Extract associated with Kappa and Sigma
perr_2param = np.sqrt(np.diag(pcov))
print('[err_kappa, err_sigma] = ', perr_2param)
print('-------------------------------------------------------------------------')

#Calculating minimised normalised error squared and data from output parameters
# Set kappa and sigma to output values
kappa = popt[0]
sigma = popt[1]

# Calculate the sum of the normalised error squared
residuals = (func(xdata, kappa, sigma) - ydata) / ydata
err = residuals**2.0
fres = sum(err)

# Calculate estimated data

Est = (1.0 / (2.0 * pi* kappa)) * (1.0 / (np.sqrt(sigma + n**2.0))**3.0)

# ------------------------------------------------------------------------
#                    Fit Three-Parameter Equation

# This section of the file will use the values of kappa and sigma output above,
# as the input quesses for the corresponding parameters in the three-parameter
```

```
# equation for the fluctuation spectra.

# Variables included here, commented out, for reference
#xdata = n
#ydata = y2
#pi = 3.1415926535

# Function to fit
def function(x, kap, sig, m2):
    #m2 = np.sqrt((sig**2 - gam))       # This line is for reference only
    return ( 1.0 / (2.0 * pi) ) * ( 1.0 / (kap * m2) ) * ( ( 1.0 / np.sqrt(sig +
                x**2.0 - m2) ) - ( 1.0 / np.sqrt(sig + x**2.0 + m2) ) )

# Fitting function
# Initial guesses for kap, sig and m2 are set in p0 = (kap, sig, m2)
popt, pcov = curve_fit(function, xdata, ydata, p0=(kappa, sigma, 1.0))

# Set output values
kap = popt[0]
sig = popt[1]
m2 = popt[2]

params = [kap, sig, m2]

gam = sig**2.0 - (m2)**2.0    # Calculate gam from m2

# Set optimal values of kappa, sigma and gamma
Optimal_P = [kap, sig, gam]

# Calculate errors associated with each parameter
perr = np.sqrt(np.diag(pcov))

# Convert to errors associated with optimal values of kappa, sigma and gamma
err_kap = perr[0]
err_sig = perr[1]
err_m2 = perr[2]
err_gam = np.sqrt( ( 2.0 * sig * err_sig )**2.0 + ( -2.0 * m2 * err_m2 )**2.0 )
```

```
err_P = [err_kap, err_sig, err_gam]

# Check for size of m2 and error
x_check = [m2, err_m2]

# Calculate error in overall fit (the sum of the normalised error squared (NES))
res = (function(xdata, kap, sig, m2) - ydata) / ydata
error = res**2.0
NES = sum(error)

# Calculate estimated data
# ETPE -> Estimated Three-Parameter Equation
n_fine = np.arange(3.0, 17.0, 0.01);
ETPE = (1.0 / (2.0 * pi)) * (1.0 / (kap * m2)) * ( ( 1.0 / np.sqrt(sig +
        n_fine**2.0 - m2) ) - ( 1.0 / np.sqrt(sig + n_fine**2.0 + m2) ) )

# ------------------------------------------------------------------------
#                    Calculate the shear modulus, mu

# This section will be used to calculate the dimensionless shear modulus and its
# associated error. The shear modulus is a function of kap, sig and av_R (the
# averge radius) calculated from the pixel length given in geo.dat which will
# need to be read in and converted from pixels to micro-m

# Read in geo.dat and extract the average radius and stdev in pixels
f=open('geo.dat',"r")
lines=f.readlines()
result=[]
for x in lines:
    result.append(x.split(' ')[2])
f.close()

result = [float(i) for i in result]

pix_av_R = np.mean(result)
pix_err_av_R = np.std(result)
```

```
#set variables and constants
const = (32.0 * pi)/9.0
pix_conversion = 51.0E-9
av_R = pix_av_R * pix_conversion
err_av_R = pix_err_av_R * pix_conversion

#calculate  mu for ratio
mu = (kap**2.0 * sig) / av_R**2.0

#calculate error in mu
err_mu = np.sqrt(((2.0 * kap * sig * err_kap)/av_R**2.0)**2.0 + ((kap**2.0
        * err_sig)/av_R**2.0)**2.0 + ((-3.0 * kap**2.0 * sig * err_av_R)
        /av_R**3.0)**2)

# ------------------------------------------------------------------------
#                        Dimensionally correct values
#added 23/01/2020

KT = (1.38E-23 * 295.15)   #assumes room temp of 22C
const_mu = ((32.0 * pi)/9.0)* (1.38E-23 * 295.15)

dimensional_kappa = kap * KT
dimensional_sigma = 2 * dimensional_kappa * sig / (av_R)**2
dimensional_gamma = gam * av_R**4 / kap
dimensional_mu = mu * const_mu

err_dimensional_kappa = KT * err_kap
# add rest of errors
#err_dimensional_sigma =
#err_dimensional_gamma =
err_dimensional_mu = const_mu * err_mu

#Collate values
dimensional_params = [dimensional_kappa, dimensional_mu]
err_dimensional_params = [err_dimensional_kappa, err_dimensional_mu]
```

```
# ------------------------------------------------------------------------

#Collate all parameters and associated errors
parameters = [kap, sig, gam, mu]
err_parameters = [err_kap, err_sig, err_gam, err_mu]


# ------------------------------------------------------------------------
# Plotting of amplitudes and respective histograms

print(' ')
print('**Plotting amplitudes and histograms**')
print(' ')
# create Amplitude_analysis file to save all pdfs to
dir = 'Amplitude_analysis'

if not os.path.exists(dir):
    os.makedirs(dir)

# a2-----------------------------
amp_a2=[]
for x in lines:
    amp_a2.append(x.split(' ')[5])
f.close()

amp_a2 = [float(i) for i in amp_a2]

plt.hist(amp_a2, bins = 20)
plt.xlabel('Amplitude')
plt.ylabel('Frequency')
plt.title('a2')
plt.tight_layout()
plt.savefig('Amplitude_analysis/Hist_a2.pdf')
plt.close()

contour_number = np.arange(1.0, 2001.0, 1);
```

```
plt.plot(contour_number, amp_a2, 'b-')
plt.title('a2')
plt.xlabel('Contour number')
plt.ylabel('Amplitude')

# Display the plot and save it to file
plt.tight_layout()              #prevents the graph being cropped in the pdf
plt.savefig('Amplitude_analysis/Amp_a2.pdf')
#plt.show()                      #Prints the plot to screen
plt.close()

# b2-----------------------------
amp_b2=[]
for x in lines:
    amp_b2.append(x.split(' ')[6])
f.close()

amp_b2 = [float(i) for i in amp_b2]

plt.hist(amp_b2, bins = 20)
plt.xlabel('Amplitude')
plt.ylabel('Frequency')
plt.title('b2')
plt.tight_layout()
plt.savefig('Amplitude_analysis/Hist_b2.pdf')
plt.close()

contour_number = np.arange(1.0, 2001.0, 1);
plt.plot(contour_number, amp_b2, 'b-')
plt.title('b2')
plt.xlabel('Contour number')
plt.ylabel('Amplitude')

# Display the plot and save it to file
plt.tight_layout()              #prevents the graph being cropped in the pdf
plt.savefig('Amplitude_analysis/Amp_b2.pdf')
#plt.show()                      #Prints the plot to screen
```

```
plt.close()

# a3-----------------------------
amp_a3=[]
for x in lines:
    amp_a3.append(x.split(' ')[7])
f.close()

amp_a3 = [float(i) for i in amp_a3]

plt.hist(amp_a3, bins = 20)
plt.xlabel('Amplitude')
plt.ylabel('Frequency')
plt.title('a3')
plt.tight_layout()
plt.savefig('Amplitude_analysis/Hist_a3.pdf')
plt.close()

contour_number = np.arange(1.0, 2001.0, 1);
plt.plot(contour_number, amp_a3, 'b-')
plt.title('a3')
plt.xlabel('Contour number')
plt.ylabel('Amplitude')

# Display the plot and save it to file
plt.tight_layout()              #prevents the graph being cropped in the pdf
plt.savefig('Amplitude_analysis/Amp_a3.pdf')
#plt.show()                      #Prints the plot to screen
plt.close()

# b3-----------------------------
amp_b3=[]
for x in lines:
    amp_b3.append(x.split(' ')[8])
f.close()

amp_b3 = [float(i) for i in amp_b3]
```

```
plt.hist(amp_b3, bins = 20)
plt.xlabel('Amplitude')
plt.ylabel('Frequency')
plt.title('b3')
plt.tight_layout()
plt.savefig('Amplitude_analysis/Hist_b3.pdf')
plt.close()

contour_number = np.arange(1.0, 2001.0, 1);
plt.plot(contour_number, amp_b3, 'b-')
plt.title('b3')
plt.xlabel('Contour number')
plt.ylabel('Amplitude')

# Display the plot and save it to file

plt.tight_layout()              #prevents the graph being cropped in the pdf
plt.savefig('Amplitude_analysis/Amp_b3.pdf')
#plt.show()                      #Prints the plot to screen
plt.close()

# a4-----------------------------
amp_a4=[]
for x in lines:
    amp_a4.append(x.split(' ')[9])
f.close()

amp_a4 = [float(i) for i in amp_a4]

plt.hist(amp_a4, bins = 20)
plt.xlabel('Amplitude')
plt.ylabel('Frequency')
plt.title('a4')
plt.tight_layout()
plt.savefig('Amplitude_analysis/Hist_a4.pdf')
plt.close()
```

```
contour_number = np.arange(1.0, 2001.0, 1);
plt.plot(contour_number, amp_a4, 'b-')
plt.title('a4')
plt.xlabel('Contour number')
plt.ylabel('Amplitude')

# Display the plot and save it to file
plt.tight_layout()              #prevents the graph being cropped in the pdf
plt.savefig('Amplitude_analysis/Amp_a4.pdf')
#plt.show()                      #Prints the plot to screen
plt.close()

# b4-----------------------------
amp_b4=[]
for x in lines:
    amp_b4.append(x.split(' ')[10])
f.close()

amp_b4 = [float(i) for i in amp_b4]

plt.hist(amp_b4, bins = 20)
plt.xlabel('Amplitude')
plt.ylabel('Frequency')
plt.title('b4')
plt.tight_layout()
plt.savefig('Amplitude_analysis/Hist_b4.pdf')
plt.close()

contour_number = np.arange(1.0, 2001.0, 1);
plt.plot(contour_number, amp_b4, 'b-')
plt.title('b4')
plt.xlabel('Contour number')
plt.ylabel('Amplitude')

# Display the plot and save it to file
```

```
plt.tight_layout()              #prevents the graph being cropped in the pdf
plt.savefig('Amplitude_analysis/Amp_b4.pdf')
#plt.show()                      #Prints the plot to screen
plt.close()

# a9-----------------------------
amp_a9=[]
for x in lines:
    amp_a9.append(x.split(' ')[19])
f.close()

amp_a9 = [float(i) for i in amp_a9]

plt.hist(amp_a9, bins = 20)
plt.xlabel('Amplitude')
plt.ylabel('Frequency')
plt.title('a9')
plt.tight_layout()
plt.savefig('Amplitude_analysis/Hist_a9.pdf')
plt.close()

contour_number = np.arange(1.0, 2001.0, 1);
plt.plot(contour_number, amp_a9, 'b-')
plt.title('a9')
plt.xlabel('Contour number')
plt.ylabel('Amplitude')

# Display the plot and save it to file
plt.tight_layout()              #prevents the graph being cropped in the pdf
plt.savefig('Amplitude_analysis/Amp_a9.pdf')
#plt.show()                      #Prints the plot to screen
plt.close()

# b9-----------------------------
amp_b9=[]
for x in lines:
    amp_b9.append(x.split(' ')[20])
```

```
f.close()

amp_b9 = [float(i) for i in amp_b9]

plt.hist(amp_b9, bins = 20)
plt.xlabel('Amplitude')
plt.ylabel('Frequency')
plt.title('b9')
plt.tight_layout()
plt.savefig('Amplitude_analysis/Hist_b9.pdf')
plt.close()

contour_number = np.arange(1.0, 2001.0, 1);
plt.plot(contour_number, amp_b9, 'b-')
plt.title('b9')
plt.xlabel('Contour number')
plt.ylabel('Amplitude')

# Display the plot and save it to file

plt.tight_layout()              #prevents the graph being cropped in the pdf
plt.savefig('Amplitude_analysis/Amp_b9.pdf')
#plt.show()                      #Prints the plot to screen
plt.close()

#-------------------------------------------------------------------------------



# Printing outputs of three param equation to the screen
print('-------------------------------------------------------------------------')
print('Output values of fitting the three parameter equation:')
print(' ')
print('[ kappa, sigma, gamma, mu ] = ', parameters)
print(' ')
print('[ err_k, err_s, err_g, err_m] = ', err_parameters)
print(' ')
```

```
print('sqrt(sigma^2 - gamma) +/- error = ', x_check)
print('------------------------------------------------------------------------')

#                    Save outputs to csv file

# Convert NES to array
# NAN -> not a number, used as a filler
a = [NES, 'NAN']

#Convert radius (av_R) and error in radius (err_av_R) to array
radius = [av_R, err_av_R]

# Save All outputs to one file, including shear modulus
# column 1 -> estimated values of data
# column 2 -> row 1 is the sum of the normalised error squared
# column 3 -> row 1 is average radius and row 2 is error in average radius
# column 4 -> dimensionless kap, sig, gam, mu (optimal/calculated values)
# column 5 -> errors associated with kap, sig, gam and mu
# column 6 -> dimensional Kappa and Mu
# column 7 -> errors in dimensional Kappa and Mu
# column 8 -> row 1 is m2 and row 2 is the associated error (row 2 > row 1)

rows = zip_longest(ETPE, a, radius, parameters, err_parameters, dimensional_params,
                        err_dimensional_params, x_check, fillvalue='')
with open("OutputData.csv", "w") as f:
    csv.writer(f).writerows(rows)


#       Plot graph
# Can change colour and marker types here
plt.plot(n, ydata,'bx', label = "Experimental")     #Plots experimental data
plt.plot(n_fine, ETPE,'r-', label = "Fit")         #Plots fitted data

# Define title, legend and axis
plt.title('Cell6')                  #Gives graph title - can change
plt.legend(loc='upper right')       #Prints the legend
plt.xlabel('n')                     #Sets x axis label
```

```
plt.ylabel('$<\delta_n^2>$')        #Sets y axis label

plt.tight_layout()                  #prevents the graph being cropped in the pdf
plt.savefig('Fit.pdf')              #Prints the plot to pdf - can change file name
plt.show()                          #Prints the plot to screen
plt.close()                         #Closes pdf file

print('**Finished**')
```

Bibliography

[1] A. Van Leeuwenhoek, 'Other microscopical observations made by the same, about the texture of the blood, the sap of some plants, the figures of sugar and salt, and the probable cause of the difference of their tastes.', in *Philosophical Transactions of the Royal Society* **1675**, *10*, 380–385, (cit. on p. 1).

[2] American Society of Hematology, Blood Basics, https://www.hematology.org/education/patients/blood-basics (visited on 29/11/2016) (cit. on p. 1).

[3] J. P. Hale, 'The thermal fluctuations of red blood cells', in **2009**, (cit. on pp. 1, 29).

[4] W. T. Tse, S. E. Lux, 'Red Blood Cell Membrane Disorders', in *British Journal of Haematology* **1999**, *104*, 2–13, DOI 10.1016/B978-0-323-35762-3.00045-7, (cit. on p. 2).

[5] J. E. Rothman, J. Lenard, 'Membrane asymmetry', in *Science* **1977**, *195*, 743–753, DOI 10.1126/science.402030, (cit. on pp. 3, 38).

[6] B. K. Brandley, R. L. Schnaar, 'Cell-surface carbohydrates in cell recognition and response', in *Journal of Leukocyte Biology* **1986**, *40*, 97–111, DOI 10.1002/jlb.40.1.97, (cit. on p. 3).

[7] K. Simons, W. L. Vaz, 'Model systems, lipid rafts, and cell membranes', in *Annual Review of Biophysics and Biomolecular Structure* **2004**, *33*, 269–295, DOI 10.1146/annurev.biophys.32.110601.141803, (cit. on pp. 3, 38).

[8] M. E. Linder, *Chapter 53: Lipid-mediated localization of signaling proteins*, *Vol. 1*, Second Edi, Elsevier Inc., **2010**, pp. 365–371 (cit. on p. 3).

[9] S. C. Liu, L. H. Derick, J. Palek, 'Visualization of the hexagonal lattice in the erythrocyte membrane skeleton', in *Journal of Cell Biology* **1987**, *104*, 527–536, DOI 10.1083/jcb.104.3.527, (cit. on p. 4).

[10] N. Mohandas, E. Evans, 'Mechanical properties of the red cell membrane in relation to molecular structure and genetic defects', in *Annual Review of Biophysics and Biomolecular Structure* **1994**, *23*, 787–818, DOI 10.1146/annurev.bb.23.060194.004035, (cit. on p. 5).

[11] Z. Rui, Z. Chenyu, Z. Qi, &. Li Donghai, 'Spectrin: Structure, function and disease', in *Science China Life Sciences* **2013**, *56*, 1076–1085, DOI 10.1007/s11427-013-4575-0, (cit. on p. 5).

[12] R. Hochmuth, R. Waugh, 'Erythrocyte membrane elasticity and viscosity', in *Annual Reviews Physiology* **1987**, *49*, 209–219, DOI 10.1212/wnl.31.10.1371, (cit. on p. 5).

[13] Y. Kim, K. Kim, Y. Park in *Blood Cell - An Overview of Studies in Hematology*, 1, **2012**, Chapter 10 (cit. on pp. 6, 9, 67).

[14] W. Helfrich, 'Elastic Properties of Lipid Bilayers: Theory and Possible Experiments', in *Zeitschrift fur Naturforschung - Section C Journal of Biosciences* **1973**, *28*, 693–703, DOI 10.1515/znc-1973-11-1209, (cit. on p. 7).

[15] E. A. Evans, 'New Membrane Concept Applied to the Analysis of Fluid Shear- and Micropipette-Deformed Red Blood Cells', in *Biophysical Journal* **1973**, *13*, 941–954, DOI 10.1016/S0006-3495(73)86036-9, (cit. on p. 7).

[16] G. Cuce, M. Aktan, *Blood Cell - An Overview of Studies in Hematology Platelets*, **09/2012** (cit. on p. 7).

[17] W. Groner, N. Mohandas, M. Bessis, 'New optical technique for measuring erythrocyte deformability with the ektacytometer.', in *Clinical chemistry* **1980**, *26*, 1435–42, (cit. on p. 7).

[18] A. Barnes, P. Locke, P. Scudder, T. Dormandy, J. Dormandy, J. Slack, 'Is hyperviscosity a treatable component of diabetic microcirculatory disease?', in *The Lancet* **1977**, *310*, 789–791, (cit. on p. 8).

[19] J. Kim, H. Lee, S. Shin, 'Advances in the measurement of red blood cell deformability: A brief review', in *Journal of Cellular Biotechnology* **2015**, *1*, 63–79, DOI 10.3233/jcb-15007, (cit. on pp. 9, 66).

[20] J. P. Shelby, J. White, K. Ganesan, P. K. Rathod, D. T. Chiu, 'A microfluidic model for single-cell capillary obstruction by Plasmodium falciparum-infected erythrocytes', in *Proceedings of the National Academy of Sciences of the United States of America* **2003**, *100*, 14618–14622, DOI 10.1073/pnas.2433968100, (cit. on p. 9).

[21] R. Wang, H. Ding, M. Mir, K. Tangella, G. Popescu, 'Effective 3D viscoelasticity of red blood cells measured by diffraction phase microscopy', in *Biomedical Optics Express* **2011**, *2*, 485, DOI 10.1364/boe.2.000485, (cit. on p. 9).

[22] C. R. Jacobs, H. Huang, R. Y. Kwon, *Introduction to cell mechanics and mechanobiology*, Garland Science, **2012** (cit. on p. 9).

[23] E. A. Evans, R. Waugh, L. Melnik, 'Elastic area compressibility modulus of red cell membrane', in *Biophysical Journal* **1976**, *16*, 585–595, DOI 10.1016/S0006-3495(76)85713-X, (cit. on p. 9).

[24] E. A. Evans, R. Waugh, 'Osmotic correction to elastic area compressibility measurements on red cell membrane', in *Biophysical Journal* **1977**, *20*, 307–313, DOI 10.1016/S0006-3495(77)85551-3, (cit. on pp. 9, 13).

[25] D. P. Theret, M. J. Levesque, M. Sato, R. M. Nerem, L. T. Wheeler, 'The application of a homogeneous half-space model in the analysis of endothelial cell micropipette measurements', in *Journal of Biomechanical Engineering* **1988**, *110*, 190–199, DOI 10.1115/1.3108430, (cit. on p. 10).

[26] M. Bokori-Brown, P. G. Petrov, M. A. Khafaji, M. K. Mughal, C. E. Naylor, A. C. Shore, K. M. Gooding, F. Casanova, T. J. Mitchell, R. W. Titball, C. P. Winlove, 'Red blood cell susceptibility to pneumolysin: Correlation with membrane biochemical and physical properties', in *Journal of Biological Chemistry* **2016**, *291*, 10210–10227, DOI 10.1074/jbc.M115.691899, (cit. on pp. 10, 15, 102).

[27] R. Waugh, E. A. Evans, 'Thermoelasticity of red blood cell membrane', in *Biophysical Journal* **1979**, *26*, 115–131, (cit. on pp. 10, 13).

[28] E. A. Evans, 'Bending elastic modulus of red blood cell membrane derived from buckling instability in micropipet aspiration tests', in *Biophysical Journal* **1983**, *43*, 27–30, DOI 10.1016/S0006-3495(83)84319-7, (cit. on pp. 10, 13, 67).

[29] J. Guck, R. Ananthakrishnan, H. Mahmood, T. J. Moon, C. C. Cunningham, J. Käs, 'The optical stretcher: A novel laser tool to micromanipulate cells', in *Biophysical Journal* **2001**, *81*, 767–784, DOI 10.1016/S0006-3495(01)75740-2, (cit. on pp. 11, 13).

[30] S. Hénon, G. Lenormand, A. Richert, F. Gallet, 'A new determination of the shear modulus of the human erythrocyte membrane using optical tweezers', in *Biophysical Journal* **1999**, *76*, 1145–1151, DOI 10.1016/S0006-3495(99)77279-6, (cit. on pp. 11, 13).

[31] J. Sleep, D. Wilson, R. Simmons, W. Gratzer, 'Elasticity of the red cell membrane and its relation to hemolytic disorders: An optical tweezers study', in *Biophysical Journal* **1999**, *77*, 3085–3095, DOI 10.1016/S0006-3495(99)77139-0, (cit. on p. 11).

[32] G. Lenormand, S. Hénon, A. Richert, J. Siméon, F. Gallet, 'Direct measurement of the area expansion and shear moduli of the human red blood cell membrane skeleton', in *Biophysical Journal* **2001**, *81*, 43–56, DOI 10.1016/S0006-3495(01)75678-0, (cit. on pp. 12, 13).

[33] F. Brochard, J. F. Lennon, 'Frequency spectrum of the flicker phenomenon in erythrocytes', in *Le Journal De Physique* **1975**, *36*, 1035–1047, (cit. on pp. 12, 67).

[34] A. Silker, H. Engelhardt, E. Sackmann, 'Dynamic Reflection Interference Contrast (Ric-) Microscopy: a New Method To Study Surface Excitations of Cells and To Measure Membrane Bending Elastic Moduli.', in *Journal de physique Paris* **1987**, *48*, 2139–2151, DOI 10.1051/jphys:0198700480120213900, (cit. on pp. 12, 13).

[35] H. Engelhardt, E. Sackmann, 'On the measurement of shear elastic moduli and viscosities of erythrocyte plasma membranes by transient deformation in high frequency electric fields', in *Biophysical Journal* **1988**, *54*, 495–508, DOI 10.1016/S0006-3495(88)82982-5, (cit. on pp. 13, 88, 106).

[36] M. L. Ellsworth, T. Forrester, C. G. Ellis, H. H. Dietrich, 'The erythrocyte as a regulator of vascular tone', in *American Journal of Physiology - Heart and Circulatory Physiology* **1995**, *269*, DOI 10.1152/ajpheart.1995.269.6.h2155, (cit. on pp. 14, 91).

[37] G. R. Bergfeld, T. Forrester, 'Release of ATP from human erythrocytes in response to a bried period of hypoxia and hypercapnia', in *Cardiovascular Research* **1992**, *26*, 40–47, (cit. on pp. 14, 91).

[38] D. B. Light, T. L. Capes, R. T. Gronau, M. R. Adler, 'Extracellular ATP stimulates volume decrease in Necturus red blood cells', in *American Journal of Physiology - Cell Physiology* **1999**, *277*, DOI 10.1152/ajpcell.1999.277.3.c480, (cit. on pp. 14, 91).

[39] R. S. Sprague, M. L. Ellsworth, A. H. Stephenson, A. J. Lonigro, 'ATP: The red blood cell link to NO and local control of the pulmonary circulation', in *American Journal of Physiology - Heart and Circulatory Physiology* **1996**, *271*, H2717–H2722, DOI 10.1152/ajpheart.1996.271.6.h2717, (cit. on pp. 14, 91).

[40] R. S. Sprague, M. L. Ellsworth, 'Erythrocyte-derived ATP and perfusion distribution: Role of intracellular and intercellular communication', in *Microcirculation* **2012**, *19*, 430–439, DOI 10.1111/j.1743-6109.2008.01122.x.Endothelial, (cit. on pp. 14, 93).

[41] F. C. Mokken, M. Kedaria, C. P. Henny, M. R. Hardeman, A. W. Gelb, 'The clinical importance of erythrocyte deformability, a hemorrheological parameter', in *Annals of Hematology* **1992**, *64*, 113–122, DOI 10.1007/BF01697397, (cit. on p. 14).

[42] M. Singh, S. Shin, 'Changes in erythrocyte aggregation and deformability in diabetes mellitus: A brief review', in *Indian Journal of Experimental Biology* **2009**, *47*, 7–15, (cit. on p. 15).

[43] W. Subasinghe, D. M. Spence, 'Simultaneous Determination of Cell Aging and ATP Release from Erythrocytes and its Implications in Type 2 Diabetes', in *Analytica Chimica Acta* **2009**, *618*, 227–233, DOI 10.1016/j.aca.2008.04.061.Simultaneous, (cit. on pp. 15, 94, 102).

[44] R. S. Sprague, M. L. Ellsworth, A. H. Stephenson, M. E. Kleinhenz, A. J. Lonigro, 'Deformation-induced ATP release from red blood cells requires CFTR activity', in *American Journal of Physiology - Heart and Circulatory Physiology* **1998**, *275*, DOI 10.1152/ajpheart.1998.275.5.h1726, (cit. on pp. 15, 92, 94).

[45] R. S. Sprague, A. H. Stephenson, M. L. Ellsworth, C. Keller, A. J. Lonigro, 'Impaired release of ATP from red blood ceils of humans with primary pulmonary hypertension', in *Experimental Biology and Medicine* **2001**, *226*, 434–439, DOI 10.1177/153537020122600507, (cit. on p. 15).

[46] F. Liang, J. Lehr, L. Danielczak, R. Leask, A. M. Kietzig, 'Robust non-wetting PTFE surfaces by femtosecond laser machining', in *International Journal of Molecular Sciences* **2014**, *15*, 13681–13696, DOI 10.3390/ijms150813681, (cit. on p. 17).

[47] J. Xue, C. S. Jung, M. W. Kim, 'Phase transitions of liquid-crystal films on an air-water interface', in *Physical Review Letters* **1992**, *69*, 474–477, DOI 10.1103/PhysRevLett.69.474, (cit. on p. 18).

[48] V. M. Kaganer, H. Möhwald, P. Dutta, 'Structure and phase transitions in Langmuir monolayers', in **1999**, *71*, 779–819, (cit. on pp. 19, 20, 59).

[49] T. R. Jensen, K. Balashev, T. Bjørnholm, K. Kjaer, 'Novel methods for studying lipids and lipases and their mutual interaction at interfaces. Part II. Surface sensitive synchrotron X-ray scattering.', in *Biochimie* **2001**, *83*, 399–408, (cit. on pp. 19, 21).

[50] O. Sakata, M. Nakamura in *Surface Science Techniques*, *Vol. 51*, (Eds.: G. Bracco, B. Holst), Springer, Berlin, Heidelberg, **2013**, Chapter 6 (cit. on p. 19).

[51] C. Kittel, *Introduction to Solid State Physics*, 8th ed., Wiley, **2004** (cit. on p. 20).

[52] B. M. Ocko, X. Z. Wu, E. B. Sirota, E. B. Sinha, O. Gang, M. Deutsch, 'Surface freezing in chain molecules: Normal alkanes', in *Physical Review E* **1997**, *55*, 3164–3182, DOI 10.1080/08940889908260986, (cit. on p. 21).

[53] J. Als-Nielsen, D. Jacquemain, K. Kjaer, F. Leveiller, M. Lahav, L. Leiserowitz, 'Principles and applications of grazing incidence X-ray and neutron scattering from ordered molecular monolayers at the air-water interface', in *Physics Reports* **1994**, *246*, 251–313, DOI 10.1016/0370-1573(94)90046-9, (cit. on pp. 22, 23).

[54] R. G. Oliveira, E. Schneck, B. E. Quinn, O. V. Konovalov, K. Brandenburg, T. Gutsmann, T. Gill, C. B. Hanna, D. A. Pink, M. Tanaka, 'Crucial roles of charged saccharide moieties in survival of gram negative bacteria against protamine revealed by combination of grazing incidence x-ray structural characterizations and Monte Carlo simulations', in *Physical Review E - Statistical Nonlinear and Soft Matter Physics* **2010**, *81*, 1–12, DOI 10.1103/PhysRevE.81.041901, (cit. on p. 24).

[55] R. G. Oliveira, E. Schneck, B. E. Quinn, O. V. Konovalov, K. Brandenburg, U. Seydel, T. Gill, C. B. Hanna, D. A. Pink, M. Tanaka, 'Physical mechanisms of bacterial survival revealed by combined grazing-incidence X-ray scattering and Monte Carlo simulation', in *Comptes Rendus Chimie* **2009**, *12*, 209–217, DOI 10.1016/j.crci.2008.06.020, (cit. on p. 24).

[56] N. Gov, A. G. Zilman, S. Safran, 'Cytoskeleton Confinement and Tension of Red Blood Cell Membranes', in *Physical Review Letters* **2003**, *90*, 4, DOI 10.1103/PhysRevLett.90.228101, (cit. on p. 26).

[57] T. Auth, S. A. Safran, N. S. Gov, 'Fluctuations of coupled fluid and solid membranes with application to red blood cells', in *Physical Review E - Statistical Nonlinear and Soft Matter Physics* **2007**, *76*, DOI 10.1103/PhysRevE.76.051910, (cit. on p. 26).

[58] J. Pécréaux, H. G. Döbereiner, J. Prost, J. F. Joanny, P. Bassereau, 'Refined contour analysis of giant unilamellar vesicles', in *European Physical Journal E* **2004**, *13*, 277–290, DOI 10.1140/epje/i2004-10001-9, (cit. on pp. 27, 67).

[59] J. P. Hale, C. P. Winlove, P. G. Petrov, 'Effect of hydroperoxides on red blood cell membrane mechanical properties', in *Biophysical Journal* **2011**, *101*, 1921–1929, DOI 10.1016/j.bpj.2011.08.053, (cit. on pp. 27, 67, 85, 86).

[60] L. G. Eriksson, 'On the shape of human red blood cells interacting with flat artificial surfaces - the 'glass effect'', in *Biochimica et Biophysica Acta* **1990**, *1036*, 193–201, (cit. on p. 27).

[61] A. M. Forsyth, J. Wan, P. D. Owrutsky, M. Abkarian, H. A. Stone, 'Multiscale approach to link red blood cell dynamics, shear viscosity, and ATP release', in *Proceedings of the National Academy of Sciences* **2011**, *108*, 10986–10991, DOI 10.1073/pnas.1101315108, (cit. on pp. 31, 32, 92).

[62] M. DeLuca, W. D. McElroy, 'Kinetics of the Firefly Luciferase Catalyzed Reactions', in *Biochemistry* **1974**, *13*, 921–925, DOI 10.1021/bi00702a015, (cit. on p. 33).

[63] Promega Corporation, ENLITEN ® ATP Assay System Bioluminescence Detection Kit for ATP Measurement, tech. rep., **2009**, p. 8 (cit. on p. 33).

[64] N. Mohandas, P. G. Gallagher, 'Red cell membrane: Past, present, and future', in *Blood* **2008**, *112*, 3939–3948, DOI 10.1182/blood-2008-07-161166, (cit. on p. 37).

[65] E. M. Bevers, P. Comfurius, R. F. A. Zwaal, 'Regulatory Mechanisms in Maintenance and Modulation of Transmembrane Lipid Asymmetry: Pathophysiological Implications', in *Lupus* **1996**, *5*, 480–487, DOI 10.1177/096120339600500531, (cit. on p. 38).

[66] K. Simons, D. Toomre, 'Lipid rafts and signal transduction', in *Nature Reviews* **2000**, *1*, 31–39, DOI 10.1002/sita.200600113, (cit. on p. 38).

[67] R. Wardhan, P. Mudgal in *Textbook of Membrane Biology*, Springer, **2017**, pp. 29–48 (cit. on p. 38).

[68] J. Li, X. Wang, T. Zhang, C. Wang, Z. Huang, X. Luo, Y. Deng, 'A review on phospholipids and their main applications in drug delivery systems', in *Asian Journal of Pharmaceutical Sciences* **2015**, *10*, 81–98, DOI 10.1016/j.ajps.2014.09.004, (cit. on p. 38).

[69] Avanti Polar Lipids, https://avantilipids.com/ (visited on 12/01/2021) (cit. on p. 39).

[70] J. Majewski, T. L. Kuhl, K. Kjaer, G. S. Smith, 'Packing of ganglioside-phospholipid monolayers: An x-ray diffraction and reflectivity study', in *Biophysical Journal* **2001**, *81*, 2707–2715, DOI 10.1016/S0006-3495(01)75913-9, (cit. on pp. 40, 42, 61).

[71] C. A. Helm, P. Tippmann-Krayer, H. Möhwald, J. Als-Nielsen, K. Kjaer, 'Phases of phosphatidyl ethanolamine monolayers studied by synchrotron x-ray scattering', in *Biophysical Journal* **1991**, *60*, 1457–1476, DOI 10.1016/S0006-3495(91)82182-8, (cit. on pp. 40, 42, 58).

[72] C. E. Miller, J. Majewski, E. B. Watkins, D. J. Mulder, T. Gog, T. L. Kuhl, 'Probing the local order of single phospholipid membranes using grazing incidence X-ray diffraction', in *Physical Review Letters* **2008**, *100*, 4–7, DOI 10.1103/PhysRevLett.100.058103, (cit. on p. 40).

[73] C. E. Miller, D. D. Busath, B. Strongin, J. Majewski, 'Integration of ganglioside GT1b receptor into DPPE and DPPC phospholipid monolayers: An X-ray reflectivity and grazing-incidence diffraction study', in *Biophysical Journal* **2008**, *95*, 3278–3286, DOI 10.1529/biophysj.107.128538, (cit. on pp. 40, 58, 59).

[74] J. Majewski, B. Stec, 'X-ray scattering studies of model lipid membrane interacting with purothionin provide support for a previously proposed mechanism of membrane lysis', in *European Biophysics Journal* **2010**, *39*, 1155–1165, DOI 10.1007/s00249-009-0568-0, (cit. on pp. 40, 41, 58, 59).

[75] M. Broniatowski, M. Flasiński, P. Dynarowicz-ŁAtka, J. Majewski, 'Grazing incidence diffraction and x-ray reflectivity studies of the interactions of inorganic mercury salts with membrane lipids in Langmuir monolayers at the air/water interface', in *Journal of Physical Chemistry B* **2010**, *114*, 9474–9484, DOI 10.1021/jp101668n, (cit. on pp. 40–42, 59, 61).

[76] D. Vaknin, M. S. Kelley, B. M. Ocko, 'Sphingomyelin at the air-water interface', in *Journal of Chemical Physics* **2001**, *115*, 7697–7704, DOI 10.1063/1.1406501, (cit. on pp. 41, 42, 59, 61).

[77] G. Tae, H. Yang, K. Shin, S. K. Satija, N. Torikai, 'X-ray reflectivity study of a transcription-activating factor-derived peptide penetration into the model phospholipid monolayers', in *Journal of peptide science* **2007**, *14*, 461–468, DOI 10.1002/psc, (cit. on pp. 42, 61, 62).

[78] D. H. Rammler, A. Zaffaroni, 'Biological implications of DMSO based on a review of its chemical properties', in *Annals of the New York Academy of Sciences* **1967**, *141*, 13–23, (cit. on p. 43).

[79] A. C. Williams, B. W. Barry, 'Penetration enhancers', in *Advanced Drug Delivery Reviews* **2012**, *64*, 128–137, DOI 10.1016/j.addr.2012.09.032, (cit. on pp. 43, 95).

[80] G. H. Lyman, H. D. Preisler, 'Membrane action of DMSO and other chemical inducers of Friend leukaemic cell diffrentiation', in **1976**, *262*, 360–363, (cit. on pp. 43, 95).

[81] T. H. Norwood, C. J. Zeigler, G. M. Martin, 'Dimethyl sulfoxide enhances polyethylene glycol-mediated somatic cell fusion', in *Somatic Cell Genetics* **1976**, *2*, 263–270, DOI 10.1007/BF01538964, (cit. on p. 43).

[82] Q. Ahkong, D. Fisher, W. Tampion, J. Lucy, 'Mechanisms of cell fusion', in *Nature* **1975**, *253*, 194–195, DOI 10.1038/253195a0, (cit. on p. 43).

[83] A. Bishayee, D. Rao, L. Bouchet, W. Bolch, R. Howell, 'Protection by DMSO against cell death caused by intracellularly loaclized iodine-125, iodine-131 and polonium-210', in *Radiation Research* **2000**, *153*, 416–427, DOI 10.1038/jid.2014.371, (cit. on p. 43).

[84] S. Mantri, S. Kanungo, P. C. Mohapatra, 'Cryoprotective Effect of Disaccharides on Cord Blood Stem Cells with Minimal Use of DMSO', in *Indian Journal of Hematology and Blood Transfusion* **2015**, *31*, 206–212, DOI 10.1007/s12288-014-0352-x, (cit. on pp. 43, 108).

[85] M. A. de Ménorval, L. M. Mir, M. L. Fernández, R. Reigada, 'Effects of dimethyl sulfoxide in cholesterol-containing lipid membranes: A comparative study of experiments in silico and with cells', in *PLoS ONE* **2012**, *7*, 1–12, DOI 10.1371/journal.pone.0041733, (cit. on p. 43).

[86] R. Notman, M. Noro, B. O. Malley, J. Anwar, 'Molecular Basis for Dimethylsulfoxide (DMSO) Action on Lipid Membranes', in **2006**, *128*, 13982–13983, DOI 10.1021/ja063363t, (cit. on pp. 43, 61, 66, 69, 88, 95).

[87] A. A. Gurtovenko, J. Anwar, 'Modulating the structure and properties of cell membranes: The molecular mechanism of action of dimethyl sulfoxide', in *Journal of Physical Chemistry B* **2007**, *111*, 10453–10460, DOI 10.1021/jp073113e, (cit. on pp. 43, 88, 89, 95).

[88] Z. E. Hughes, A. E. Mark, R. L. Mancera, 'Molecular dynamics simulations of the interactions of DMSO with DPPC and DOPC phospholipid membranes', in *Journal of Physical Chemistry B* **2012**, *116*, 11911–11923, DOI 10.1021/jp3035538, (cit. on p. 43).

[89] T. T. Mills, J. Huang, G. W. Feigenson, J. F. Nagle, 'Effects of cholesterol and unsaturated DOPC lipid on chain packing of saturated gel-phase DPPC bilayers', in *General Physiology and Biophysics* **2009**, *28*, 126–139, DOI 10.4149/gpb_2009_02_126, (cit. on p. 45).

[90] C. Wölk, H. Youssef, T. Guttenberg, H. Marbach, G. Vizcay-Barrena, C. Shen, G. Brezesinski, R. D. Harvey, 'Phase Diagram for a Lysyl-Phosphatidylglycerol Analogue in Biomimetic Mixed Monolayers with Phosphatidylglycerol: Insights into the Tunable Properties of Bacterial Membranes', in *ChemPhysChem* **2020**, *21*, 702–706, DOI 10.1002/cphc.202000026, (cit. on p. 45).

[91] O. Albrecht, Gruler. H., E. Sackmann, 'Polymorphism of Phospholipid Monolayers.', in *J Phys (Paris)* **1978**, *39*, 301–313, DOI 10.1051/jphys:01978003903030100, (cit. on p. 59).

[92] L. Chen, X. Xie, Z. W. Yu, P. J. Quinn, 'The kinetics and mechanism of the formation of crystalline phase of dipalmitoylphosphatidylethanolamine dispersed in aqueous dimethyl sulfoxide solutions', in *Chemistry and Physics of Lipids* **2004**, *127*, 153–159, DOI 10.1016/j.chemphyslip.2003.10.011, (cit. on p. 60).

[93] X. Chen, Z. Huang, W. Hua, H. Castada, H. C. Allen, 'Reorganization and caging of DPPC, DPPE, DPPG, and DPPS monolayers caused by dimethylsulfoxide observed using brewster angle microscopy', in *Langmuir* **2010**, *26*, 18902–18908, DOI 10.1021/la102842a, (cit. on p. 60).

[94] V. I. Gordeliy, M. A. Kiselev, P. Lesieur, A. V. Pole, J. Teixeira, 'Lipid membrane structure and interactions in dimethyl sulfoxide/water mixtures', in *Biophysical Journal* **1998**, *75*, 2343–2351, DOI 10.1016/S0006-3495(98)77678-7, (cit. on pp. 61, 63).

[95] U. Dahmen-Levison, G. Brezesinski, H. Möhwald, 'Specific adsorption of PLA2 at monolayers', in *Thin Solid Films* **1998**, *327-329*, 616–620, DOI 10.1016/S0040-6090(98)00725-1, (cit. on p. 61).

[96] B. Gironi, Z. Kahveci, B. McGill, B.-D. Lechner, S. Pagliara, J. Metz, A. Morresi, F. Palombo, P. Sassi, P. Petrov, 'Effect of DMSO on the Mechanical and Structural Properties of Model and Biological Membranes', in *Biophysical Journal* **2020**, *119*, DOI 10.1016/j.bpj.2020.05.037, (cit. on pp. 61, 81).

[97] S. M. Sadrzadeh, E. Graf, S. S. Panter, P. E. Hallaway, J. W. Eaton, 'Hemoglobin. A biologic Fenton reagent', in *Journal of Biological Chemistry* **1984**, *259*, 14354–14356, (cit. on p. 66).

[98] S. A. Mendanha, J. L. Anjos, A. H. Silva, A. Alonso, 'Electron paramagnetic resonance study of lipid and protein membrane components of erythrocytes oxidized with hydrogen peroxide', in *Brazilian Journal of Medical and Biological Research* **2012**, *45*, 473–481, DOI 10.1590/S0100-879X2012007500050, (cit. on pp. 66, 85).

[99] J. F. Koster, R. G. Slee, 'Lipid peroxidation of human erythrocyte ghosts induced by organic hydroperoxides', in *Methods* **1983**, *2*, 233–239, (cit. on pp. 66, 86).

[100] P. S. Becker, C. M. Cohen, S. F. Lux, 'The effect of mild diamide oxidation on the structure and function of human erythrocyte spectrin', in *Journal of Biological Chemistry* **1986**, *261*, 4620–4628, (cit. on pp. 66, 87, 106).

[101] J. P. Hale, G. Marcelli, K. H. Parker, C. P. Winlove, P. G. Petrov, 'Red blood cell thermal fluctuations: comparison between experiment and molecular dynamics simulations', in *Soft Matter* **2009**, *5*, 3603, DOI 10.1039/b910422d, (cit. on pp. 67, 113).

[102] D. Boal, *Mechanics of the Cell*, 2nd ed., Cambridge University Press, **2012** (cit. on p. 67).

[103] A. Zilker, M. Ziegler, E. Sackmann, 'Spectral analysis of erythrocyte flickering in the 0.3-4-μm-1 regime by microinterferometry combined with fast image processing', in *Physical Review A* **1992**, *46*, 7998–8001, DOI 10.1103/PhysRevA.46.7998, (cit. on p. 67).

[104] J. G. Mohanty, E. Nagababu, J. M. Rifkind, 'Red blood cell oxidative stress impairs oxygen delivery and induces red blood cell aging', in *Frontiers in Physiology* **2014**, *5 FEB*, 1–6, DOI 10.3389/fphys.2014.00084, (cit. on p. 68).

[105] P. K. Maurya, P. Kumar, P. Chandra, 'Biomarkers of oxidative stress in erythrocytes as a function of human age', in *World Journal of Methodology* **2015**, *5*, 216, DOI 10.5662/wjm.v5.i4.216, (cit. on p. 68).

[106] G. Pizzino, N. Irrera, M. Cucinotta, G. Pallio, F. Mannino, V. Arcoraci, F. Squadrito, D. Altavilla, A. Bitto, 'Oxidative Stress: Harms and Benefits for Human Health', in *Oxidative Medicine and Cellular Longevity* **2017**, *2017*, DOI 10.1155/2017/8416763, (cit. on p. 68).

[107] P. Gupta, A. Lakes, T. Dziubla, *A Free Radical Primer*, Elsevier Inc., **2016**, pp. 1–33 (cit. on p. 68).

[108] V. Kuhn, L. Diederich, T. C. Keller, C. M. Kramer, W. Lückstädt, C. Panknin, T. Suvorava, B. E. Isakson, M. Kelm, M. M. Cortese-Krott, 'Red Blood Cell Function and Dysfunction: Redox Regulation, Nitric Oxide Metabolism, Anemia', in *Antioxidants and Redox Signaling* **2017**, *26*, 718–742, DOI 10.1089/ars.2016.6954, (cit. on pp. 68, 69).

[109] A. Matte, M. Bertoldi, N. Mohandas, X. An, A. Bugatti, A. M. Brunati, M. Rusnati, E. Tibaldi, A. Siciliano, F. Turrini, S. Perrotta, L. De Franceschi, 'Membrane association of peroxiredoxin-2 in red cells is mediated by the N-terminal cytoplasmic domain of band 3', in *Free Radical Biology and Medicine* **2013**, *55*, 27–35, DOI 10.1016/j.freeradbiomed.2012.10.543, (cit. on p. 68).

[110] R. Van Zwieten, A. J. Verhoeven, D. Roos, 'Inborn defects in the antioxidant systems of human red blood cells', in *Free Radical Biology and Medicine* **2014**, *67*, 377–386, DOI 10.1016/j.freeradbiomed.2013.11.022, (cit. on pp. 68, 106).

[111] M. R. Clemens, H. D. Waller, 'Lipid peroxidation in erythrocytes', in *Chemistry and Physics of Lipids* **1987**, *45*, 251–268, DOI 10.1016/0009-3084(87)90068-5, (cit. on p. 69).

[112] M. Koch, K. E. Wright, O. Otto, M. Herbig, N. D. Salinas, N. H. Tolia, T. J. Satchwell, J. Guck, N. J. Brooks, J. Baum, 'Plasmodium falciparum erythrocyte-binding antigen 175 triggers a biophysical change in the red blood cell that facilitates invasion', in *Proceedings of the National Academy of Sciences of the United States of America* **2017**, *114*, 4225–4230, DOI 10.1073/pnas.1620843114, (cit. on pp. 69, 87, 88).

[113] A. Sinha, T. T. Chu, M. Dao, R. Chandramohanadas, 'Single-cell evaluation of red blood cell bio-mechanical and nano-structural alterations upon chemically induced oxidative stress', in *Scientific Reports* **2015**, *5*, 1–8, DOI 10.1038/srep09768, (cit. on pp. 75, 86–88, 107).

[114] L. M. Snyder, N. L. Fortier, J. Trainor, J. Jacobs, L. Leb, B. Lubin, D. Chiu, S. Shohet, N. Mohandas, 'Effect of hydrogen peroxide exposure on normal human erythrocyte deformability, morphology, surface characteristics, and spectrin-hemoglobin cross-linking', in *Journal of Clinical Investigation* **1985**, *76*, 1971–1977, DOI 10.1172/JCI112196, (cit. on p. 85).

[115] M. A. Srour, Y. Y. Bilto, M. Juma, M. R. Irhimeh, 'Exposure of human erythrocytes to oxygen radicals causes loss of deformability, increased osmotic fragility, lipid peroxidation and protein degradation', in *Clinical Hemorheology and Microcirculation* **2000**, *23*, 13–21, (cit. on p. 85).

[116] R. Morabito, O. Romano, G. La Spada, A. Marino, 'H2O2-induced oxidative stress affects SO4 = Transport in human erythrocytes', in *PLoS ONE* **2016**, *11*, 1–16, DOI 10.1371/journal.pone.0146485, (cit. on p. 85).

[117] J. J. van den Berg, J. A. Op den Kamp, B. H. Lubin, B. Roelofsen, F. A. Kuypers, 'Kinetics and site specificity of hydroperoxide-induced oxidative damage in red blood cells', in *Free Radical Biology and Medicine* **1992**, *12*, 487–498, DOI 10.1016/0891-5849(92)90102-M, (cit. on p. 86).

[118] N. Shaklai, B. Frayman, N. Fortier, M. Snyder, 'Crosslinking of isolated cytoskeletal proteins with hemoglobin: a possible damage inflicted to the red cell membrane', in *Biochimica et Biophysica Acta* **1987**, *915*, 406–414, (cit. on p. 86).

[119] J. McKenney, C. R. Valeri, N. Mohandas, N. Fortier, A. Giorgio, L. M. Snyder, 'Decreased in vivo survival of hydrogen peroxide-damaged baboon red blood cells', in *Blood* **1990**, *76*, 206–211, DOI 10.1182/blood.v76.1.206.bloodjournal761206, (cit. on p. 86).

[120] A. Van Der Laarse, R. H. Julicher, L. Sterrenberg, C. H. Van Treslong, 'Lipid peroxidation in neonatal rat heart cell cultures: Effects of cumene hydroperoxide', in *Cardiovascular Research* **1986**, *20*, 20–25, DOI 10.1093/cvr/20.1.20, (cit. on p. 86).

[121] A. Ayala, M. F. Muñoz, S. Argüelles, 'Lipid peroxidation: Production, metabolism, and signaling mechanisms of malondialdehyde and 4-hydroxy-2-nonenal', in *Oxidative Medicine and Cellular Longevity* **2014**, *2014*, DOI 10.1155/2014/360438, (cit. on p. 86).

[122] S. A. Jewell, P. G. Petrov, C. P. Winlove, 'The effect of oxidative stress on the membrane dipole potential of human red blood cells', in *Biochimica et Biophysica Acta - Biomembranes* **2013**, *1828*, 1250–1258, DOI 10.1016/j.bbamem.2012.12.019, (cit. on pp. 86, 115).

[123] V. R. Akoev, A. V. Matveev, T. V. Belyaeva, Y. A. Kim, 'The effect of oxidative stress on structural transitions of human erythrocyte ghost membranes', in *Biochimica et Biophysica Acta - Biomembranes* **1998**, *1371*, 284–294, DOI 10.1016/S0005-2736(98)00037-6, (cit. on p. 86).

[124] T. M. Fischer, C. W. Haest, M. Stöhr, D. Kamp, B. Deuticke, 'Selective alteration of erythrocyte deformability by SH-reagents. Evidence for an involvement of spectrin in membrane shear elasticity', in *BBA - Biomembranes* **1978**, *510*, 270–282, DOI 10.1016/0005-2736(78)90027-5, (cit. on p. 87).

[125] J. A. Chasis, N. Mohandas, 'Erythrocyte membrane deformability and stability: Two distinct membrane properties that are independently regulated by skeletal protein associations', in *Journal of Cell Biology* **1986**, *103*, 343–350, DOI 10.1083/jcb.103.2.343, (cit. on p. 87).

[126] J. M. Sosa, N. D. Nielsen, S. M. Vignes, T. G. Chen, S. S. Shevkoplyas, 'The relationship between red blood cell deformability metrics and perfusion of an artificial microvascular network', in *Clinical Hemorheology and Microcirculation* **2014**, *57*, 291–305, DOI 10.3233/CH-131719, (cit. on pp. 87, 88).

[127] J. Wan, W. D. Ristenpart, H. A. Stone, 'Dynamics of shear-induced ATP release from red blood cells', in *Pnas* **2008**, *105*, 16432–16437, DOI 10.1073/pnas.0805779105, (cit. on pp. 87, 93, 101, 106).

[128] A. M. Forsyth, J. Wan, W. D. Ristenpart, H. A. Stone, 'The dynamic behavior of chemically "stiffened" red blood cells in microchannel flows', in *Microvascular Research* **2010**, *80*, 37–43, DOI 10.1016/j.mvr.2010.03.008, (cit. on p. 87).

[129] J. A. Power, J. W. Harris, D. F. Bainton, 'Lipid peroxidation and morphological changes in mammalian cells treated with the glutathione oxidant, diamide', in *Experimental Cell Research* **1977**, *105*, 455–460, DOI 10.1016/0014-4827(77)90142-2, (cit. on pp. 87, 106).

[130] D. Janigro, T. S. Nguyen, E. L. Gordon, H. R. Winn, 'Physiological properties of ATP-activated cation channels in rat brain microvascular endothelial cells', in *American Journal of Physiology - Heart and Circulatory Physiology* **1996**, *270*, DOI 10.1152/ajpheart.1996.270.4.h1423, (cit. on pp. 91, 93).

[131] R. Van Wijk, W. W. Van Solinge, 'The energy-less red blood cell is lost : erythrocyte enzyme abnormalities of glycolysis', in *Blood* **2005**, *106*, 4034–4042, DOI 10.1182/blood-2005-04-1622.4034, (cit. on p. 91).

[132] Z. Xu, W. Dou, C. Wang, Y. Sun, 'Stiffness and ATP recovery of stored red blood cells in serum', in *Microsystems & nanoengineering* **2019**, *5*, 1–9, (cit. on p. 91).

[133] J. Wan, A. M. Forsyth, H. A. Stone, 'Red blood cell dynamics: From cell deformation to ATP release', in *Integrative Biology* **2011**, *3*, 972–981, DOI 10.1039/c1ib00044f, (cit. on p. 92).

[134] G. M. Braunstein, R. M. Roman, J. P. Clancy, B. A. Kudlow, A. L. Taylor, V. G. Shylonsky, B. Jovov, K. Peter, T. Jilling, I. I. Ismailov, D. J. Benos, L. M. Schwiebert, J. G. Fitz, E. M. Schwiebert, 'Cystic Fibrosis Transmembrane Conductance Regulator Facilitates ATP Release by Stimulating a Separate ATP Release Channel for Autocrine Control of Cell Volume Regulation', in *Journal of Biological Chemistry* **2001**, *276*, 6621–6630, DOI 10.1074/jbc.M005893200, (cit. on p. 92).

[135] N. S. Gov, S. A. Safran, 'Red blood cell membrane fluctuations and shape controlled by ATP-induced cytoskeletal defects', in *Biophysical Journal* **2005**, *88*, 1859–1874, DOI 10.1529/biophysj.104.045328, (cit. on p. 92).

[136] G. Burnstock, 'Blood cells: an historical account of the roles of purinergic signalling', in *Purinergic Signalling* **2015**, *11*, 411–434, DOI 10.1007/s11302-015-9462-7, (cit. on p. 93).

[137] K. Chen, R. N. Pittman, A. S. Popel, 'Nitric oxide in the vasculature: Where does it come from and where does it go? A quantitative perspective', in *Antioxidants and Redox Signaling* **2008**, *10*, 1185–1198, DOI 10.1089/ars.2007.1959, (cit. on p. 93).

[138] D. J. Fischer, N. J. Torrence, R. J. Sprung, D. M. Spence, 'Determination of erythrocyte deformability and its correlation to cellular ATP release using microbore tubing with diameters that approximate resistance vessels in vivo', in *Analyst* **2003**, *128*, 1163–1168, DOI 10.1039/b308225n, (cit. on p. 93).

[139] J. Barcroft, *The respiratory function of the blood.* Cambridge,Univ. Press, **1914** (cit. on p. 93).

[140] A. Krogh, *The anatomy and physiology of capillaries*, *Vol. 18*, Yale University Press, **1922** (cit. on p. 93).

[141] D. C. Poole, S. W. Copp, D. M. Hirai, T. I. Musch, 'Dynamics of muscle microcirculatory and blood-myocyte O(2) flux during contractions.', in *Acta physiologica (Oxford England)* **2011**, *202*, 293–310, DOI 10.1111/j.1748-1716.2010.02246.x, (cit. on p. 94).

[142] J. C. Stein, M. L. Ellsworth, 'Capillary oxygen transport during severe hypoxia: Role of hemoglobin oxygen affinity', in *Journal of Applied Physiology* **1993**, *75*, 1601–1607, DOI 10.1152/jappl.1993.75.4.1601, (cit. on p. 94).

[143] S. Majdi, N. Najafinobar, J. Dunevall, J. Lovric, A. G. Ewing, 'DMSO Chemically Alters Cell Membranes to Slow Exocytosis and Increase the Fraction of Partial Transmitter Released', in *ChemBioChem* **2017**, *18*, 1898–1902, DOI 10.1002/cbic.201700410, (cit. on p. 95).

[144] A. K. Price, D. J. Fischer, R. S. Martin, D. M. Spence, 'Deformation-induced release of ATP from erythrocytes in a poly(dimethylsiloxane)-based microchip with channels that mimic resistance vessels', in *Analytical Chemistry* **2004**, *76*, 4849–4855, DOI 10.1021/ac0495992, (cit. on pp. 98, 105).

[145] A. K. Price, R. S. Martin, D. M. Spence, 'Monitoring erythrocytes in a microchip channel that narrows uniformly: Towards an improved microfluidic-based mimic of the microcirculation', in *Journal of Chromatography A* **2006**, *1111*, 220–227, DOI 10.1016/j.chroma.2005.07.083, (cit. on pp. 98, 105).

[146] P. Jarolim, M. Lahav, S. C. Liu, J. Palek, 'Effect of hemoglobin oxidation products on the stability of red cell membrane skeletons and the associations of skeletal proteins: Correlation with a release of hemin', in *Blood* **1990**, *76*, 2125–2131, DOI 10.1182/blood.v76.10.2125.bloodjournal76102125, (cit. on p. 105).

[147] J. M. Gutteridge, 'Lipid peroxidation and antioxidants as biomarkers of tissue damage', in *Clinical Chemistry* **1995**, *41*, 1819–1828, DOI 10.1093/clinchem/41.12.1819, (cit. on p. 105).

[148] C. Richter, 'Biophysical consequences of lipid peroxidation in membranes', in *Chemistry and Physics of Lipids* **1987**, *44*, 175–189, DOI 10.1016/0009-3084(87)90049-1, (cit. on p. 105).

[149] P. Spangenberg, U. Till, S. Gschmeissner, N. Crawford, 'Changes in the distribution and organization of platelet actin induced by diamide and its functional consequences', in *British Journal of Haematology* **1987**, *67*, 443–450, DOI 10.1111/j.1365-2141.1987.tb06167.x, (cit. on p. 106).

[150] F. A. Bencsath, A. Shartava, C. A. Monteiro, S. R. Goodman, 'Identification of the disulfide-linked peptide in irreversibly sickled cell β-actin', in *Biochemistry* **1996**, *35*, 4403–4408, DOI 10.1021/bi960063n, (cit. on p. 106).

[151] I. Dalle-Donne, R. Rossi, A. Milzani, P. Di Simplicio, R. Colombo, 'The actin cytoskeleton response to oxidants: From small heat shock protein phosphorylation to changes in the redox state of actin itself', in *Free Radical Biology and Medicine* **2001**, *31*, 1624–1632, DOI 10.1016/S0891-5849(01)00749-3, (cit. on p. 106).

[152] D. B. Hinshaw, J. M. Burger, T. F. Beals, B. C. Armstrong, P. A. Hyslop, 'Actin polymerization in cellular oxidant injury', in *Archives of Biochemistry and Biophysics* **1991**, *288*, 311–316, DOI 10.1016/0003-9861(91)90200-3, (cit. on p. 106).

[153] W. Wang, C. Oliva, G. E. Li, A. Holmgren, C. H. Lillig, K. L. Kirk, 'Reversible silencing of CFTR chloride channels by glutathionylation', in *Journal of General Physiology* **2005**, *125*, 127–141, DOI 10.1085/jgp.200409115, (cit. on p. 106).

[154] J. Carroll, M. Raththagala, W. Subasinghe, S. Baguzis, T. D'amico Oblak, P. Root, D. Spence, 'An altered oxidant defense system in red blood cells affects their ability to release nitric oxide-stimulating ATP.', in *Molecular bioSystems* **2006**, *2*, 305–311, DOI 10.1039/b604362n, (cit. on p. 106).

[155] S. Tunçer, R. Gurbanov, I. Sheraj, E. Solel, O. Esenturk, S. Banerjee, 'Low dose dimethyl sulfoxide driven gross molecular changes have the potential to interfere with various cellular processes', in *Scientific Reports* **2018**, *8*, 1–15, DOI 10.1038/s41598-018-33234-z, (cit. on p. 107).

[156] J. Sikora, S. N. Orlov, K. Furuya, R. Grygorczyk, 'Hemolysis is a primary ATP-release mechanism in human erythrocytes', in *Blood* **2014**, *124*, 2150–2157, DOI 10.1182/blood-2014-05-572024, (cit. on p. 107).

[157] X. Yi, M. Liu, Q. Luo, H. Zhuo, H. Cao, J. Wang, Y. Han, 'Toxic effects of dimethyl sulfoxide on red blood cells, platelets, and vascular endothelial cells in vitro', in *FEBS Open Bio* **2017**, *7*, 485–494, DOI 10.1002/2211-5463.12193, (cit. on p. 107).

[158] F.-R. E. Curry, J. F. Clark, R. H. Adamson, 'Sphingosine-1-phosphate from erythrocytes modulates water and macromolecule permeability in rat microvessels', in *The FASEB Journal* **2012**, *26*, 855.5–855.5, DOI https://doi.org/10.1096/fasebj.26.1_supplement.855.5, (cit. on p. 114).